Varying Capacitance Machines for Marine Energy Systems Connected to HVDC Grids

by

David J. Skrovanek

A dissertation submitted in partial fulfillment
of the requirements for the degree of
Doctor of Philosophy
(Electrical and Computer Engineering)

at the
University of Wisconsin-Madison
2024

Date of Final Oral Exam: 12/10/2024
The dissertation is approved by the following members of the Final Oral Committee:

Daniel C. Ludois, Professor, Electrical and Computer Engineering
Giri Venkataramanan, Professor, Electrical and Computer Engineering
Line A. Roald, Associate Professor, Electrical and Computer Engineering
Lei Zhou, Assistant Professor, Mechanical Engineering

Varying Capacitance Machines for Marine Energy Systems Connected to HVDC Grids

David J. Skrovanek

Abstract

High-voltage direct current (HVDC) transmission is increasingly being used in offshore wind and other marine energy systems to improve the efficiency of submarine cable transmission. A barrier to its adoption, however, is the complex network of transformers and power electronics needed to transform the low-voltage AC output of the electric generators into HVDC. Fundamentally, this complexity arises from the fact that the electric machines typically used in power generation (i.e., any machine that relies on magnetic induction: synchronous machines, induction machines, etc.) are inherently low-voltage devices incapable of producing voltages in the range used for HVDC transmission. By instead utilizing electrostatic machinery that can naturally facilitate high-voltage operation, the power conversion for realizing HVDC transmission can be drastically simplified.

Building off of a concept first proposed by General Electric in 1977, this work presents an architecture based on varying capacitance machines and cascaded bridge converters. Using an averaged model, this work demonstrates analytically that the proposed architecture enables a linear scaling of the system's terminal characteristics. Each "cell" consisting of a machine and rectifier can be connected in series, in parallel, or in a combination of both—demonstrating the system's inherent modularity that is desired in modern HVDC systems. Much like the modular multi-level converter (MMC), the architecture proposed in this work also provides redundancy and fault tolerance in contrast to systems consisting of a single stage operating at the full transmission voltage.

The analytical model is then verified experimentally at the bench scale using single-pole varying capacitance machine prototypes connected in series and in parallel. To demonstrate the opportunities for power density improvement with electrostatic machine design techniques, finite element analysis (FEA) was used to optimize the geometry of the prototype's rotor and stator plates, resulting in an 18-pole machine design. Additional prototypes with this optimized design were constructed and tested, ultimately yielding a 3x improvement in power density. Finally, a detailed FEA simulation was used to create a varying capacitance machine design for utility-scale power generation.

To my grandfather, CLM.

Acknowledgements

I would first like to acknowledge my advisor, Prof. Dan Ludois, for his support and guidance throughout my PhD journey. His creativity, willingness to take risks, and passion for engineering (mixed with a healthy dose of cynicism) serve as an inspiration. I have learned a lot about engineering and how the world works.

I would also like to thank all of the staff, faculty, and members of the Wisconsin Electric Machines and Power Electronics Consortium (WEMPEC) for their support. In particular, I would like to thank Kyle Hanson and Pia Strampp for their input and assistance with my experiments and for keeping everyone safe in the lab. My labmates and friends within WEMPEC also deserve a shout-out for creating a fun and supportive environment, including Blake Rose, Shiying Wang, Jamie Turnbull, Sarah Behringer, Marisa Tisler Liben, Federico Coppo, Gokhan Cakal, Justin Paddock, Connor Akers, and Maitreyee Marathe.

If it had not been for all of the teachers, professors, and mentors I have had over the years, I probably would not be where I am today. From my time as an undergraduate, I would like to thank Prof. William Stanchina and Prof. Zhi-Hong Mao for inspiring me to always be curious, as well as Prof. Sabine Von Dirke and Prof. Anita Lukic for bringing out the inner humanist in me. I would also like to thank Christian Großer for taking me in during my time in Germany and his continued mentorship over the years.

My family deserves a lot of credit for shaping me into the person I am today. From encouraging me to pursue my passions to always being patient listeners, I would like to thank you all: my parents, my sister, my grandparents, and my soon-to-be in-laws. In particular, I would like to acknowledge my grandfather, Charles, for serving as a role model and for teaching me what is truly important in life.

Finally, I would like to express my appreciation to my fiancée, Eleanna. Her love, unyielding support, and outlook on life have been integral to my personal and professional successes. I am so lucky to have you in my life.

Contents

List of Figures

List of Tables

Chapter 1

Introduction

> *And this I believe: that the free, exploring mind of the individual human is the most valuable thing in the world.*
>
> — John Steinbeck, "East of Eden" (1952)

While the benefits of deriving electricity from carbon-free resources are well established, achieving a reality in which all electricity originates from these "net-zero" resources remains unclear. Undeterred, nations worldwide have placed their faith (and investments) behind several technologies, most notably solar photovoltaics (PV) and onshore wind turbines. Although harnessing these land-based resources has been met with much success, there is a consensus that net-zero carbon goals cannot be achieved without tapping into offshore energy resources. However, harvesting the energy from ocean waves, currents, tides, and winds poses a number of unique technical challenges in power conversion and transmission, motivating the exploration of new technologies to address these challenges.

1.1 Overview of marine energy

The oceans are brimming with energy, with an estimated 45-130 petawatt-hours (PWh) available each year [1]. While it is difficult to draw comparisons with other energy resources, it suffices to say that the energy available in the oceans is on the same order of magnitude as the global demand for electricity, which topped 25 PWh in 2022. [2].

Resource	Preferred geography	Available energy, in TWh/yr.	Grid-connected installations, in MW (2020)
Tides	Scattered	1,200	524.6
Thermal gradients	Near equator, 30°N-30°S at depths >1000m	44,000	0
Salinity gradients	River mouths feeding into ocean	1,650	0
Currents	Open ocean	Unknown	0
Waves	Coasts at higher latitudes, 30°-60°	29,500	2.3
Offshore wind	Coasts at higher latitudes, 30°-60°	36,000	64,300

Table 1.1: Summary chart of energy sources from ocean [5]–[7]

Energy can be extracted from the ocean in several different ways: from tides, thermal gradients, salinity gradients, currents, waves, and the wind. Table 1.1 provides an overview of these ocean energy sources. As can be gleaned from Table 1.1, only tidal, wave, and offshore wind energy have been used to generate utility-scale electricity so far, with offshore wind being the most mature technology among these by far. China is responsible for nearly half of all offshore wind capacity (46%), with another 40% belonging to European countries [3], see Fig. 1.1. Based on figures announced by offshore wind developers, nearly 200 GW is expected to be installed by 2029, with China being responsible for a third of the anticipated capacity. Despite being far behind other countries, the US has made it a goal to install 30 GW of offshore wind by 2030 [4]. Presently, most installations in the US are off the coast of New England and the mid-Atlantic states but future development is planned for the West Coast and even Lake Erie.

Although the nature of marine energy resources and the devices to capture their energy differ greatly from one another, the process of generating electricity for the utility grid is uniform, regardless of the technology used (see Fig. 1.2). First, the raw energy (e.g., waves, winds, etc.) must be captured, concentrated, and converted into a suitable mechanical form to drive the electric generator. Oftentimes, a power take-off (PTO) is used to assist

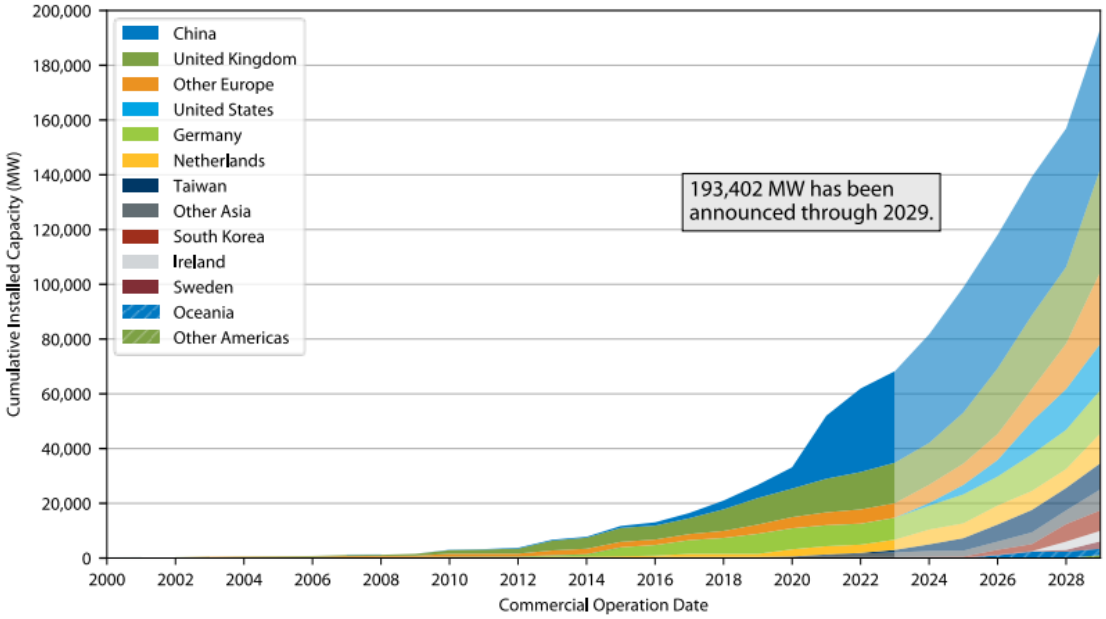

Figure 1.1: Estimated cumulative fixed-bottom and floating offshore wind capacity by country based on developer-announced commercial operation dates, from [3]

with this pre-processing of the mechanical energy, especially in wave energy systems. Designing systems to capture the raw energy is an active area of research but is not covered in this dissertation. The role of the electric generator is to then convert the mechanical energy into electrical energy. Rotating electric machinery is used more often than linear machinery, but linear machinery is increasingly being investigated for niche applications (particularly wave energy). As such, this work focused on rotating electric machinery but linear direct-drive machinery was also explored briefly for wave energy (see Appendix).

Before the electricity can be transmitted to the grid or to its load, it needs to be processed by power electronics and transformers to convert AC to DC or DC to AC, to step up voltages, to regulate some physical quantity (e.g., bus voltage, speed), or some combination thereof. It will be demonstrated in the next few sections that power transmission is not only considerably more challenging for offshore energy sources but is also a function of the type electric machinery used (i.e., magnetic vs. electrostatic).

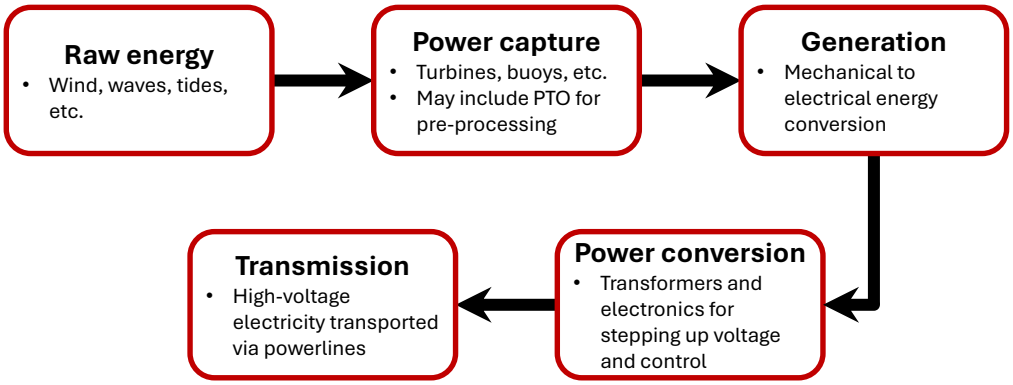

Figure 1.2: Flow of energy in marine energy systems

1.2 Challenges in offshore transmission

Power transmission is oftentimes treated as a matter of secondary importance in the design of marine energy systems but is just as important as other design aspects. Compared with using standard bare overhead transmission lines, power transmission in offshore energy systems is considerably more expensive and complex, owing to the fact that submarine cables must be used. These specially-designed cables consist of multiple layers of mechanical and electrical insulation to withstand the harsh, corrosive sea environment (see Fig. 1.3). At roughly 3 million EUR per km, the cable costs alone are a factor of 3 to 12 times higher than those for bare overhead lines [8]. Trenches in the seafloor must also be dug for the cables, such that they are protected from ships, anchors, and other hazards. With distances between offshore wind farms and onshore substations exceeding hundreds of km, the effort required to connect offshore wind farms with the grid is far greater than the effort needed for onshore wind farms.

In addition to these environmental differences, the choice of transmission technology (AC vs. DC) is more critical with submarine cables than it is for bare overhead lines.

In submarine cables (as well as in underground cables), there is a significant amount of capacitive coupling between the conductor and the outer shield of the cable amounting to roughly 160-600 nF/km, which is roughly 20 times greater than the typical capacitance of bare overhead lines [9], [10]. Because this greater capacitance in cables leads to significant "charging currents", it becomes impractical to use AC transmission in submarine cables beyond a certain length, typically around 100 km [10]. Although reactive compensation is often a solution for underground cable systems on land, offshore submarine cables can only be compensated at each end of the cable, reducing its efficacy. With DC transmission, however, these capacitive effects are not an issue.

Regardless of whether AC or DC transmission is used, offshore energy systems cannot be directly connected to the onshore grid. A variety of offshore substation platforms are needed to collect power and step up voltages. Offshore substations are significantly more expensive than onshore substations, with typical offshore substations costing 100-150 million EUR per unit, which is roughly an order of magnitude more than the 4-20 million EUR per unit needed for onshore substations [8]. For DC transmission, an additional platform is necessary to house the high-voltage AC to DC converter (typically a voltage source converter – VSC). These structures are enormous, both in terms of their physical size as well as their cost. Towering 53 meters above the water, the 800-MW DolWin gamma HVDC platform used in the DolWin1 wind farm in the North Sea cost 1.3-1.5 billion EUR for its construction and installation in 2017 [11]. Other estimates peg HVDC converter station capital costs at roughly 150,000 EUR per MW [8].

1.3 Impact of machine design on transmission systems

Just as the physics of cable technology explained in the previous section shed light onto the differences between AC and DC transmission and some of the challenges this creates, the physics underlying electromechanical energy conversion are responsible for the architectures used in offshore transmission systems. By briefly exploring the fundamental nature of energy conversion in magnetic and electrostatic machines, it will become apparent why

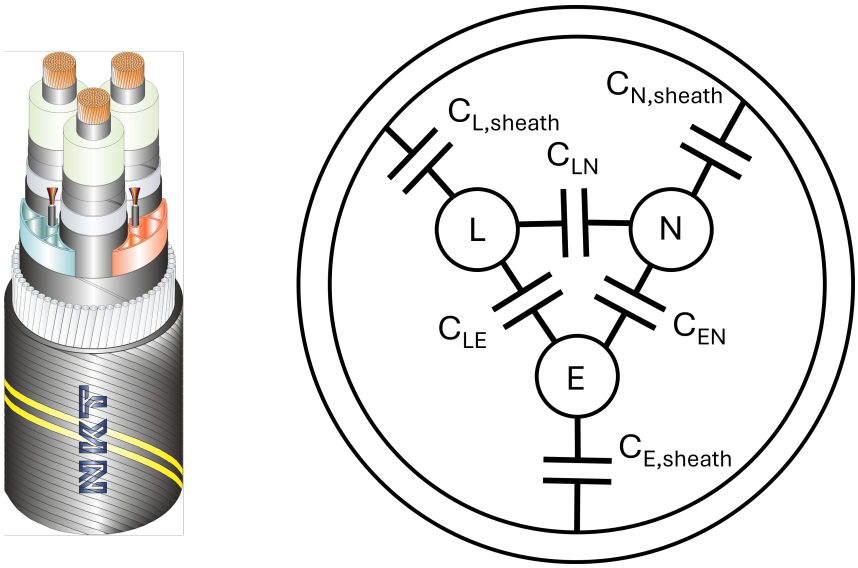

Figure 1.3: Cross section of 420-kV three-phase submarine cable from NKT Cable [12] and diagram of capacitances in cable

electrostatic machinery is well suited to marine energy applications.

All systems that convert mechanical energy into electrical energy and vice versa make use of either magnetic fields **B** or electric fields **E** as the medium through which the energy conversion takes place. The Lorentz Force equation captures the essence of this statement, since energy conversion is fundamentally tied to forces, where the force **F** on a charge q is given by

$$\mathbf{F} = q\left(\mathbf{E} + v \times \mathbf{B}\right) \tag{1.1}$$

with the linear velocity **v** being crossed with **B**. Because the force associated with electric fields does not have any velocity term, it is easy to see why these systems are generally referred to as "electrostatic". Within the field of electric machinery and drives, systems that make use of magnetic fields – which constitute the overwhelming majority of motors and other electromechanical devices – are simply referred to as "magnetic" or "electromagnetic". Note that for rotating electric machinery, forces are replaced by torques and linear velocities are replaced by angular velocities.

The fundamental factors influencing the power of any electromechanical system, be it magnetic or electrostatic, can be derived by taking power as the product of voltage v

and current i, $P = vi$. In magnetic systems, Faraday's Law is used to represent v as $\frac{d\lambda}{dt}$, where the flux linkage λ is defined as the product of inductance L and current, $\lambda = Li$. In electrostatic systems, the definition of current in terms of charge is used, $i = \frac{dq}{dt}$, along with the definition of charge in terms of capacitance, $q = CV$. Differentiating each term with respect to time and applying the product rule yields

$$P = vi = Li\frac{di}{dt} + i^2\frac{dL}{dt} \tag{1.2}$$

for electromagnetic systems, and

$$P = vi = Cv\frac{dv}{dt} + v^2\frac{dC}{dt} \tag{1.3}$$

for electrostatic systems. In both Eq. 1.2 and Eq. 1.3, only the second term corresponds to any electromechanical energy conversion, as the first term corresponds to an exchange of reactive power between the load and energy stored in the magnetic or electric fields. For each system, the second term is made up of two parts, each equal to $\frac{1}{2}i^2\frac{dL}{dt}$ or $\frac{1}{2}v^2\frac{dC}{dt}$. One of these terms corresponds to a change in the field energy due to a change in inductance/capacitance and the other corresponds to the change in mechanical energy needed to change the inductance/capacitance. As such, the quantity of interest from the perspective of power generation is $\frac{1}{2}i^2\frac{dL}{dt}$ or $\frac{1}{2}v^2\frac{dC}{dt}$. These relationships can also be derived from the principle of co-energy and is covered extensively in [13].

Comparing the terms in Eq. 1.2 with Eq. 1.3 provides insight as to why conventional electric machinery requires several step-up transformers for transmission and why electrostatic machinery does not. Because the induced voltage in an electromagnetic system is limited by how quickly mechanical work (e.g., the ocean wave, wind) can vary λ (i.e., $\mathbf{B}$), the output voltage can never approach the voltages needed for transmission (>100 kV). Although increasing $\mathbf{B}$ could theoretically increase the induced voltage, most magnetic materials saturate at 1.5-2 T, imposing a physical limit on the output voltage that can be achieved. In contrast to magnetic machinery, the voltage in electrostatic systems is

limited only by the maximum electric field it can insulate, which can be raised by simply increasing the distance between electrodes or by changing the insulating medium (i.e., using different dielectric materials, raising or lowering pressure of gas-based dielectric, etc.). Thus, by operating at the voltages needed for transmission, step-up transformers can be eliminated by using electrostatic machinery.

To illustrate the effect of magnetic machinery's low-voltage nature on real-life systems, Fig. 1.4a depicts the architecture of a typical offshore wind farm with an HVDC link, such as the 400-MW Merkur Windpark in the North Sea connected to the DolWin1 HVDC link [14]. In the Merkur Windpark, 66 GE Haliade 150-6 wind turbines with permanent magnetic synchronous machines (SM) and a rated power of 6 MW are connected to back-to-back (B2B) converters, where the 900 V output of each SM is raised to several kV. Medium-voltage transformers are then used to step the voltage up to 33 kV before power is collected in four groups of 100 MW (16 or 17 turbines per group). Each group at 33 kV is then stepped up again with a high-voltage transformer to 155 kV and the four groups are condensed into two groups. Finally, each 155-kV group is fed into the DolWin1 VSC to rectify the voltage for DC transmission to shore at ± 320 kV. In addition to introducing significant costs and complexity to the offshore wind farm, all of these transformers and power electronics incur appreciable losses. Even if each stage of power conversion is 99% efficient, over 5% of the power delivered to the shaft of the SM is lost before it is delivered onshore:

$$\frac{P_{onshore}}{P_{shaft}} = \eta_{\text{SM}}\eta_{\text{B2B}}\eta_{\text{MV trafo}}\eta_{\text{HV trafo}}\eta_{\text{VSC}} = (0.99)^5 = 95.1\%. \tag{1.4}$$

1.4 Variable capacitor machinery: The silver bullet?

It is clear from the prior sections that there are significant technical hurdles associated with marine energy systems that must be overcome to allow for a more rapid and economical deployment of these systems. HVDC has emerged as the preferred transmission technology for transporting the generated electricity onshore but remains costly and complicated using conventional means.

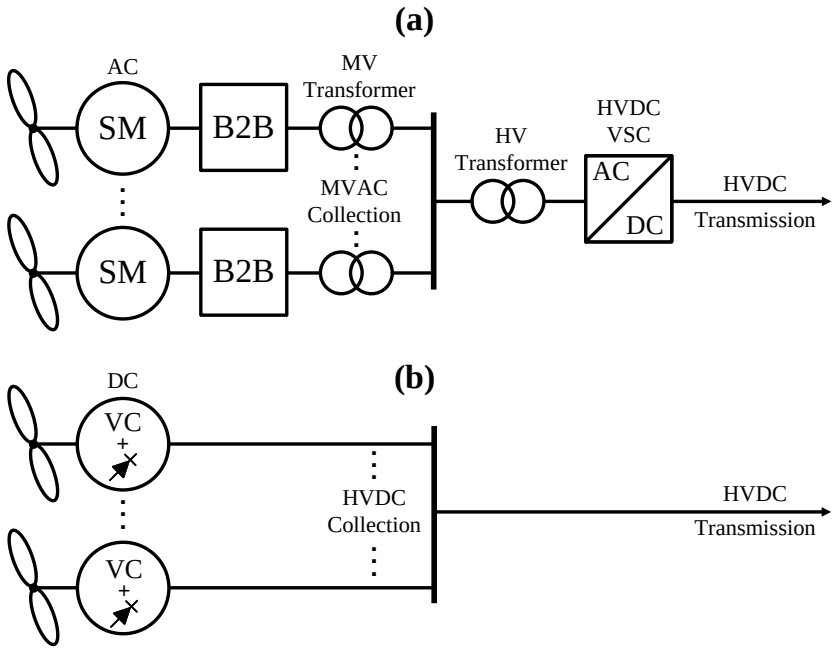

Figure 1.4: (a) Single line diagram of an offshore wind farm using MVAC collection and an HVDC link to onshore (e.g., DolWin1 in Germany [14]) and (b) proposed HVDC system using variable capacitor machines

Electrostatic machinery may be the key technology to enable the proliferation of marine energy systems, as it substantially simplifies the power conversion architecture needed for HVDC transmission (see Fig. 1.4b). Because electrostatic machines can operate at tens or hundreds of kV, step-up transformers are not needed. In addition, these machines can be constructed out of lightweight and abundant materials, such as plastics and aluminum, reducing some of the financial burdens associated with materials and construction.

Although any type of electrostatic machine can be used, this work focuses on varying capacitance machinery (also known as elastance machinery). These machines can be connected to cascaded half-bridge converters, forming "cells". Each cell can be connected either in series or in parallel, depending on the transmission voltage and the operating voltage of each machine. A more detailed description of the proposed system will be provided in subsequent Chapters.

1.5 Organization of Thesis

This dissertation presents a concept based on varying capacitance machinery and cascaded bridge converters to bypass some of the complexities with contemporary HVDC systems. Building off of a concept first proposed by General Electric (GE) in 1977 [15], this work revamps that original design by applying a modern understanding of power electronics and electrostatic machine design. The rest of the dissertation is organized as follows:

- First, background information and a review of electrostatic machinery is presented in Chapter 2 with a focus on its application to HVDC systems. The original HVDC concept proposed by GE is described in detail along with its shortcomings.

- Chapter 3 derives an averaged model to mathematically describe the system. It is demonstrated that using a cascaded bridge converter with multiple machines enables a linear scaling of the system's terminal characteristics.

- In Chapter 4, the analytical model and architecture is verified experimentally at the bench scale using varying capacitance machine prototypes connected in series and in parallel.

- In Chapter 5, finite element analysis (FEA) is used to create improved varying capacitance machine designs and to point out flaws in the GE design. The specifications for a 3300-kW machine at 200 kV are also presented.

- Concluding remarks and this work's contributions are summarized in Chapter 6. Areas for future work are also outlined.

- Chapter 7 explains this work in common, everyday language with the hope that it can be understood and appreciated by a broader audience.

- Efforts to design and prototype linear direct-drive wave energy converters connected to HVDC grids are documented in the Appendix.

Chapter 2

Background and Review

Necessity is the mother of invention.

— Ancient Proverb

The case will be made as to why electrostatic machinery is naturally well-suited to HVDC applications and how it can scale to utility systems in ways that magnetic machinery cannot. Following a brief overview of the different types of common electrostatic machinery, a review of macroscale varying capacitance machinery will be provided. Additional details on a concept paper written by General Electric will be provided, as this paper serves as the basis of this work's HVDC concept.

2.1 Need for electrostatic machinery

A key aspect of the proposed architecture in Fig 1.4b that eliminates the need for step-up transformers is operation of the machinery at transmission-level voltages, necessitating special techniques to enable this high-voltage operation. Paschen's Law [16] dictates that the breakdown voltage of gases can be increased by operating either at high pressures or at ultra-low pressures (i.e., vacuum). While operation of electrostatic machinery at high pressures (50-450 psi) has been previously demonstrated [17], [18], it is not as practical as operating with a vacuum, given the large pressure differential imposed upon the interface between the machine located in the pressure vessel and the external shaft connecting to

the prime mover [19]. In addition, the safety precautions for a vessel at high pressures are far more serious than those for a vacuum chamber but are not insurmountable.

If an electric machine is to operate in a vacuum, it is imperative that this machine produce as little heat as possible since heat generated by the machine cannot be conducted through a vacuum. By examining and comparing electrostatic and magnetic machines from a physical perspective, it becomes clear why electrostatic machines are better suited to vacuum-operation than magnetic machines.

At the most fundamental circuit level, electrostatic and magnetic machines can be represented as variable capacitors and variable inductors, respectively. If the parasitic behavior of each system is considered, they can equivalently be represented as the circuits depicted in Fig. 2.1. For capacitors, these parasitics include a series resistance R_s corresponding to a non-zero resistivity of the electrodes and a parallel resistance R_p corresponding to charge leakage through an imperfect dielectric. Similarly, the windings used in inductors have a non-zero R_s, but the parallel resistance R_{core} arises from magnetic effects, such as Eddy currents and hysteresis.

While it may seem that both systems suffer equally from these unwanted effects, at-scale electrostatic systems can approach their ideal (and near lossless) behavior much more closely than their magnetic counterparts are able to. In electrostatic systems, the physical length of the circuit elements (i.e., capacitor electrodes) are relatively short, leading to $R_s \rightarrow 0$. Combined with its low current nature, at-scale electrostatic machinery has negligible conduction losses, which are $\propto i^2 R_s$. In addition, for systems operating in a vacuum at voltages lower than the partial discharge and field emission limits, $R_p \rightarrow \infty$. For example, [20] reported $R_p = 10^{15}\ \Omega$ for a vacuum-insulated axial flux varying capacitance machine operating at 73 kV.

Unlike the parasitics in the variable capacitor, the parasitics in the variable inductor do not disappear as the system scales up. Even if high quality conductors such as copper are used to create the windings in a magnetic machine, the sheer length of wire needed to create those at-scale magnetic machines ensures that $R_s >> 0$ (since $R_s \propto \ell$). As is

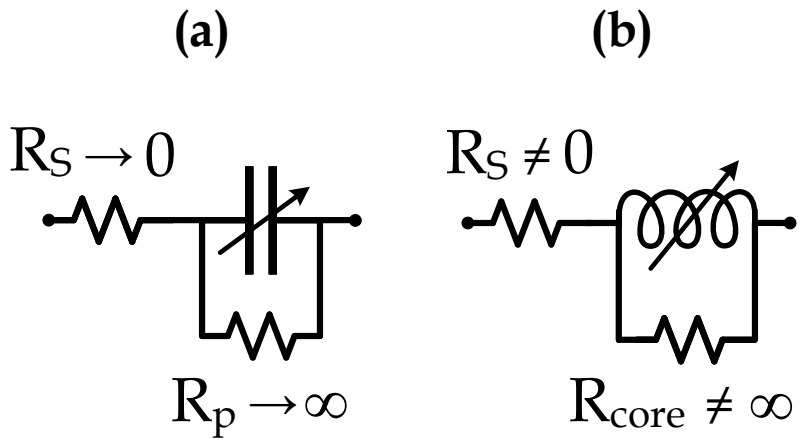

Figure 2.1: Equivalent circuit diagrams of (a) variable capacitor and (b) variable inductor with parasitic effects

the case with transformers, conduction losses scale with the size of the magnetic machine, posing additional challenges related to thermal management. Furthermore, losses from R_{core} are proportional to the frequency of operation and do not shrink as the system scales up. These core losses in magnetic machines also scale with the pole count, since a higher pole count raises the fundamental frequency. In electrostatic systems, however, increasing the pole count does not incur additional losses, allowing for machines with high pole counts to be used.

2.2 Classification of electrostatic machines

Any machine that utilizes electric fields to produce torque falls under the category of electrostatic. While it has been shown that the triboelectric and piezoelectric effects can facilitate electromechanical power conversion, these two electrostatic phenomena are limited to low-power applications and are thus omitted for the sake brevity. More information regarding their application to marine energy can be read in [21]. For macroscale systems, most electrostatic machines have direct analogs to magnetic machines, and these analogs are summarized in Table 2.1. More details can be found in [19], [22].

Varying capacitance machines – which are the focus of this work – derive torque from

capacitive saliency, which is achieved by two plates of a capacitor moving relative to one another, such that the capacitance varies between a minimum and maximum value. Technically, these machines would be most correctly referred to as "elastance" machines, since elastance is the dual of magnetic reluctance, but "varying capacitance" is used more often in the literature. A voltage V_s is applied to the stationary electrode, and torque is proportional to $V_s^2 \frac{dC}{d\theta}$. Physically, this "elastance" torque arises from the system acting to minimize the stored electrostatic energy in the capacitor (i.e., acts to maximize capacitance). Because voltage is only applied to the stator, brushed contacts, slip rings, and other connections to the rotor are not necessary.

In separately excited synchronous machines, voltage is applied to the rotating/moving electrodes, oftentimes with brushes or slip rings. As a motor, AC voltage is also applied to the stator and the generated torque is known as a "field" torque, proportional to $V_s V_r \cos(\gamma)$, where γ is the angle between the stator and rotor.

Asychronous or induction machines make use of charge induction to create a charge distribution in the rotor that moves at a different speed than the stator, much like how slip works in magnetic induction machines. In this case, the torque is referred to as "induction torque" and is proportional to $V_r G_r \frac{1-s}{s}$, where G_r is the conductance of the rotor and s is the slip.

Table 2.1: Overview of common electrostatic machinery, from [19]

Electrostatic machine	**Magnetic machine**
Varying capacitance or elastance	Switched or synchronous reluctance
Separately-excited synchronous	Wound-field synchronous
Asynchronous/induction	Asynchronous/induction

2.3 Review of macroscale varying capacitance machinery

The idea of using varying capacitance machinery for applications in HVDC power systems dates back as far as the 1930s during which J.G. Trump experimentally demon-

strated the operation of a rotating vacuum-insulated 73-kV axial flux variable capacitor machine [20]. There continued to be scattered attempts with both vacuum-insulated and pressurized gas-insulated variable capacitor machines operating at 100s of kV over the next few decades [17], [18], [23], [24] but efforts largely stagnated following the advent of solid-state electronics (see Table 2.2). It was not until 1977 that varying capacitance machines were once again explored as a viable option for HVDC, albeit without any experimental investigation [15]. Published in 1977 in a concept paper by General Electric (GE) [15], a system was proposed that consists of multiple vacuum-insulated varying capacitance machines connected to a ladder rectifier inspired by the Cockcroft-Walton voltage multiplier to act as a charge pump. In addition to producing HVDC directly without any step-up transformers, the GE system depicted in Fig. 2.2 does not require any rare earth materials, electrical steel, or copious amounts of copper. Although the 100-pole, 7 MW paper design was promising, boasting an impressive power density of 4.5 MW/m^3 and output voltage of 200 kV DC, it ultimately was never built, barring a bench-scale demonstration of a single varying capacitance machine in [25]. Through the lens of a modern understanding of power electronics, there are several limitations with the original GE design that prevented it from being built. These limitations stem primarily from the rectifier design itself and the machine design tools available at that time:

- While Cockcroft-Walton multipliers are effective at low power levels, they are not suitable for higher power applications [26]. The required voltage insulation of each Nth diode in the Cockcroft-Walton-style rectifier grows with the number of machines N, which can quickly become problematic if the output of each machine is 10s or 100s of kV.

- The Cockcroft-Walton-style rectifier does not have effective dynamic control, which would be necessary for any sort of grid-connected energy system.

- With a pole count of 100, the fundamental electrical frequency of the proposed machine's output would be in the range of kHz, which could not be efficiently rectified by semiconductor technology back in the 1970s (e.g., silicon diodes).

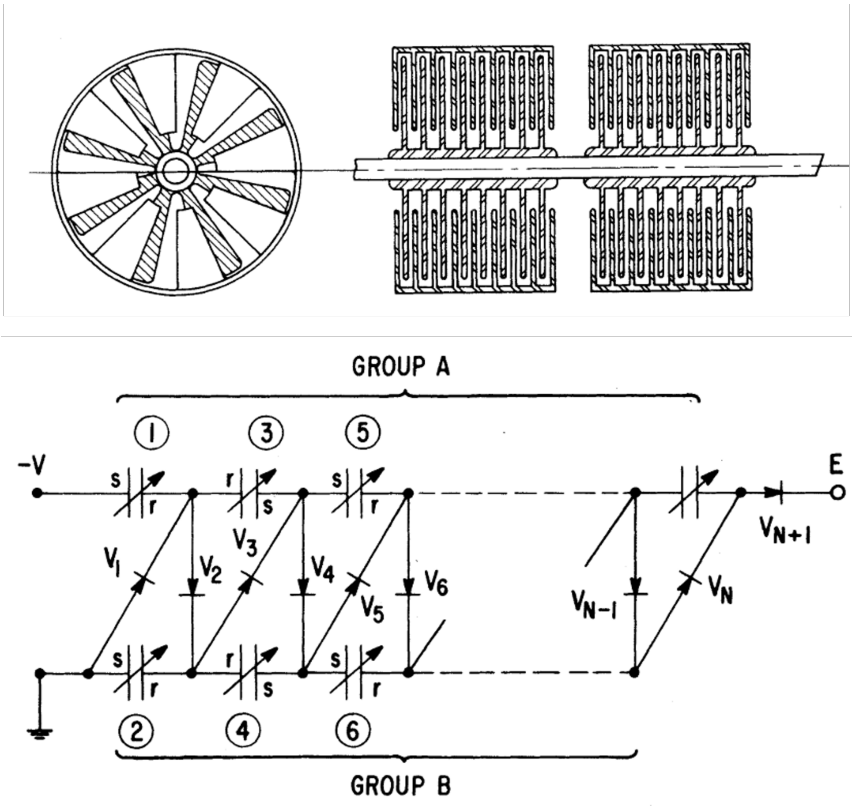

Figure 2.2: Varying capacitance machine (top) and ladder rectifier inspired by the Cockcroft-Walton voltage multipler to generate HVDC directly (bottom), from [15]

- Significant advancements in electrostatic machine design have been made available through computational tools (e.g., Finite Element Analysis - FEA), which were not widely available at the time the paper was published.

Table 2.2: Review of variable capacitor machinery

References	Insulation	Rotor OD	Voltage	Air gap	Speed	Power
[20]	Vacuum at 10^{-5} torr	343 cm	73 kV (excitation)	10 mm	3600 rpm	55 W
[23]	Pressurized air at 4 atm	490 mm	160 kV (output)	5 mm	1200 rpm	32 W
[24]	Pressurized air at 30 atm	39 cm	250 kV (output)	4 mm	750 rpm	500 W
[25], [27]	Air at 1 atm	-	600 V (excitation)	-	60 rpm	nW-µW
This work, 1-pole machine	Air at 1 atm	67 mm	1.4 kV (excitation)	0.5 mm	2500 rpm	0.14 W
This work, 18-pole machine	Air at 1 atm	67 mm	1.9 kV (excitation)	0.5 mm	2500 rpm	0.25 W

Chapter 3

Mathematical Modeling

> *Somehow the wondrous promise of the earth is that there are things beautiful in it, things wondrous and alluring, and by virtue of your trade you want to understand them.*
>
> — Mitchel Feigenbaum

After providing an overview of the system, a single varying capacitance machine and rectifier cell powering an RC load will be analyzed. The analysis will then be extended to the cases of multiple machine cells connected in series and in parallel. While [28]–[34] derive instantaneous quantities for charge pump circuits, the analysis in this paper is concerned with developing an averaged model to gain a more holistic understanding of its operation. The expressions for maximum power transfer will also be derived.

3.1 System Overview

The architecture consists of N cells, where each cell is composed of a varying capacitance machine in series with an excitation voltage source V_E, a half-wave rectifier, and an output capacitor (see Fig. 3.1). These cells can be connected in series, in parallel, or in a combination of both—demonstrating the system's inherent modularity that is desired in modern HVDC systems [35], [36]. Much like the modular multi-level converter (MMC), the architecture proposed in this work also provides redundancy and fault tolerance in

contrast to systems consisting of a single stage operating at the full transmission voltage. Regardless of whether the cells are connected in series or in parallel (see Fig. 3.2), V_E must be isolated and controllable. By controlling V_E, the output voltage can be regulated, much like controlling the field supply excitation in a wound-field synchronous machine (WFSM). Section 3.2 will show that V_E provides no real power, only reactive power.

A simple triangle waveform that varies between C_{min} and C_{max} at an "electrical" period T_e will be assumed for $C(t)$. If the machine has multiple poles $\mathcal{P}$, the period and frequency of the capacitance variation will scale accordingly by $\mathcal{P}$ (this is in contrast to magnetic machines, where the frequency scales by $\frac{\mathcal{P}}{2}$). Thus, the "mechanical" frequency f_m (i.e., the speed at which the shaft rotates) will be distinguished from the electrical frequency f_e (i.e., the speed of the capacitance variation) by

$$f_e = \mathcal{P} f_m. \tag{3.1}$$

To simplify the analysis, it will be assumed that the diodes are ideal (i.e., no forward voltage drop and no reverse current). It will also be assumed that the time constant of the load is much larger than the cycle time of each capacitance variation, $R_L C_L >> T_e$, in order to maintain a constant output voltage over T_e.

By rectifying each machine individually and combining their outputs thereafter, voltage insulation requirements for the diodes are lowered. While simple diode bridge rectifiers have been proposed for use in magnetic machinery, they are generally avoided due to poor power factor and high harmonic content [37]. These issues are not a concern for the nearly lossless electrostatic machinery but active or power factor correction (PFC) rectifier techniques (e.g., a DC-DC conversion stage after the diode bridge) would further enhance each cell's power output.

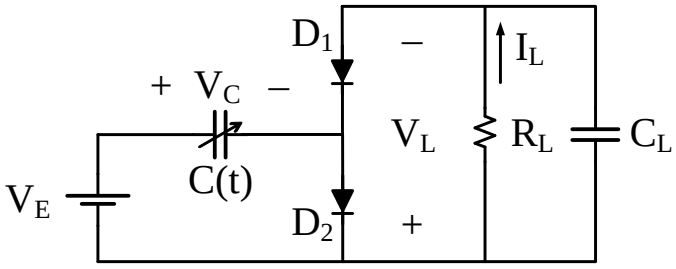

Figure 3.1: Single variable capacitor machine connected to an RC load, forming one cell ($N = 1$). For $N > 1$, R_L and C_L scale by either N or $\frac{1}{N}$, depending on whether the cells are configured in series or in parallel.

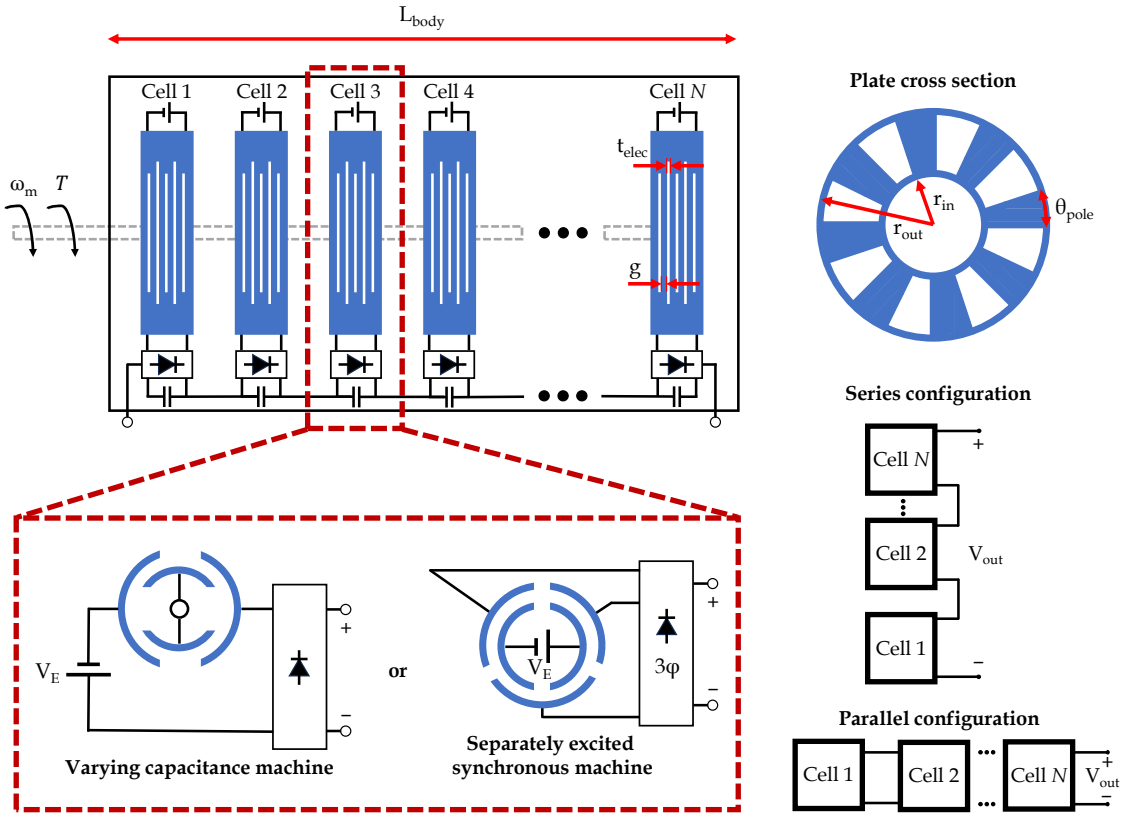

Figure 3.2: Diagram of proposed system to realize transformer-less generation of HVDC. Machine cells can be connected in series or in parallel, and are compatible with multiple electrostatic machine types.

3.2 Analysis on a single cell

Each cell is charge pump, delivering charge to the load during each half cycle of the capacitance variation. Accordingly, the analysis can be broken up into two Modes, where each Mode corresponds to the polarity of $\frac{dC(t)}{dt}$. By determining the charge Q in the machine during each Mode, the net charge delivery to the load can be solved for, which can then be used to derive the remaining quantities in the circuit. Fig. 3.4 and 3.5 depict the waveforms of several parameters of interest to support the ensuing mathematical derivation.

During Mode 1 (white region in Fig. 3.4), the capacitance is increasing and V_E is providing charge to the machine, so the voltage across the machine V_C will remain constant and equal to the magnitude of V_E. Current will flow clockwise through the bottom diode D_2 and the maximum charge on the machine will be

$$Q_1 = C_{max} V_E. \tag{3.2}$$

As soon as the capacitance starts decreasing, V_C will begin increasing since charge is conserved. Once $V_C > V_E$, the top diode D_1 will begin to conduct at time t_d, denoting the start of Mode 2 (gray region in Fig. 3.4). Current will now reverse direction, flowing up through the bottom terminal of R_L and C_L. Because the direction of the load current I_L is counter-clockwise, the polarity of V_L will be negative with respect to V_E. If a positive V_L is desired, V_E must be made negative. The minimum charge in the machine is now influenced by the excitation and load voltages:

$$Q_2 = C_{min} \left(V_E + V_L \right). \tag{3.3}$$

If $\Delta C = C_{max} - C_{min}$, the net charge delivery to the load can be expressed as

$$\Delta Q = V_E \Delta C - V_L C_{min}. \tag{3.4}$$

The short-circuit current I_{SC} and open-circuit voltage V_{OC} can immediately be derived by taking

$$\langle I_{SC} \rangle = \frac{\Delta Q}{\Delta t}\bigg|_{V_L=0} = \frac{V_E \Delta C}{T_e} \tag{3.5}$$

and

$$\Delta Q = 0 \rightarrow \langle V_{OC} \rangle = V_E \frac{\Delta C}{C_{min}}. \tag{3.6}$$

Because I_{SC} is speed-dependent, this implies that the system innately behaves like a current source. In accordance with the duality between electrostatic (capacitive) and magnetic (inductive) systems, the open-circuit voltage of magnetic machinery is speed dependent, allowing those systems to be represented as voltage sources. These results are also supported by Maxwell's equations, since Faraday's Law dictates that a time-varying magnetic field results in a "back emf" voltage, and Ampere's Law states that a time-varying electric field yields a so-called displacement current. More practically, the varying capacitance system can equivalently be represented as a current source I_S, feeding into a load, where $I_S = I_{SC}$. In addition, the machine has an effective Norton equivalent internal resistance R_{int} that can be taken as

$$\langle R_{int} \rangle = \frac{\langle V_{OC} \rangle}{\langle I_{SC} \rangle} = \frac{T_e}{C_{min}}. \tag{3.7}$$

This representation simplifies the analysis when connecting multiple machines (see Fig. 3.3). It is important to note that R_{int} is not a physical resistor but is merely an equivalent representation of the machine's ability to deliver current to the load (if R_{int} is low, little current will reach the load). As such, R_{int} does not dissipate any power or reduce the system efficiency.

The remaining average steady-state circuit quantities can be derived by either solving the equivalent circuit in Fig. 3.3 or by setting

$$\langle I_L \rangle = \frac{\Delta Q}{\Delta t} = \frac{\langle V_L \rangle}{R_L} \tag{3.8}$$

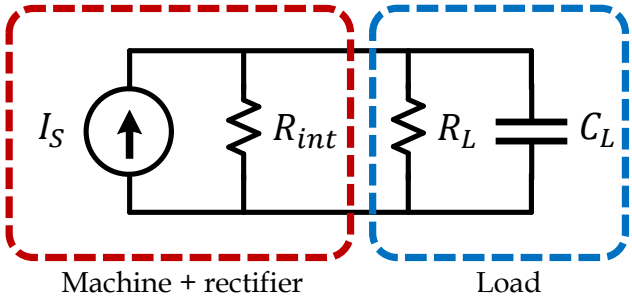

Figure 3.3: Equivalent averaged model circuit of system

and solving for $\langle V_L \rangle$ (see Table 3.1).

3.2.1 Diode switching time

The time at which Mode 1 ends and Mode 2 begins, t_d, can be solved for since the average current through C_L is zero, meaning that charge is balanced. To solve for t_d, the charge in C_L during each Mode must be set equal to each other and solved for t_d:

$$\int_0^{t_d} i_{C_L,1}(t)\,dt = \int_{t_d}^{T} i_{C_L,2}(t)\,dt. \tag{3.9}$$

During Mode 1, C_L is isolated from the machine, so it is only influenced by the load dynamics. In addition, because $R_L C_L >> T_e$, $v_L(t)$ is nearly constant, allowing the expression to be simplified:

$$i_{C_L,1}(t) = C_L \frac{dv_L(t)}{dt} + \frac{v_L(t)}{R_L} \approx \frac{\langle V_L \rangle}{R_L}. \tag{3.10}$$

During Mode 2, C_L is now influenced by the machine dynamics as well as the load but can be simplified due to $v_L(t)$ being nearly constant:

$$i_{C_L,2} = C_L \frac{dv_L(t)}{dt} - \frac{v_L(t)}{R_L} - \left(\frac{dC(t)}{dt} v_C(t) + \frac{dv_C(t)}{dt} C(t) \right) \approx \frac{-\langle V_L \rangle}{R_L} + \frac{2\Delta C}{T_e} \langle V_C \rangle. \tag{3.11}$$

After substituting $i_{C_L,1}(t)$ and $i_{C_L,2}(t)$ into Eq. 3.9, it can be shown that

$$t_d = T_e \left(1 - \frac{1}{2}\frac{\langle V_L \rangle}{\langle V_C \rangle}\frac{T_e}{R_L \Delta C}\right). \tag{3.12}$$

To simplify the expression even further, the expression for $\langle V_L \rangle$ from Table 3.1 can be substituted in, $\langle V_L \rangle = V_E \frac{\Delta C}{\frac{1}{f_e R_L} + C_{min}}$, and from KVL, $\langle V_C \rangle = \langle V_L \rangle + V_E$, so:

$$t_d = T_e \left(1 - \frac{1}{2}\frac{T_e}{R_L C_{max} + T_e}\right). \tag{3.13}$$

3.3 Analysis on multiple cells

The analysis for the N-level system follows the same approach as the analysis for the system with one cell. The key difference is in appropriately scaling Eq. 3.2-3.3 by N, depending on whether the cells are connected in series or in parallel.

When the cells are connected in series, the load voltage is split among the N cells. During Mode 1, the load voltage is being blocked by the top diodes, so it does not affect Eq. 3.2. However, this will influence Eq. 3.3 during Mode 2, such that $Q_{2,series} = C_{min}\left(V_E + \frac{V_L}{N}\right)$. For a parallel connection of the cells, both Eq. 3.2 and Eq. 3.3 will scale by N, since the charge from N current sources connected in parallel will scale linearly. In addition, R_{int} will scale by N, where $R_{int} = \frac{NT_e}{C_{min}}$ and $\frac{T_e}{NC_{min}}$ for the series and parallel connections, respectively. See Table 3.1 for all of the expressions.

3.4 Maximum power transfer

If no restrictions are imposed on the maximum voltage V_{max} that the variable capacitor can insulate, impedance matching the load to the source results in $R_{L,opt} = \frac{N}{f_e C_{min}}$ and $\frac{1}{N f_e C_{min}}$ for the series and parallel connections, respectively. While these values yield the true maximum power that can be delivered to the load (see Fig. 3.6), it would undesirable in most cases to operate at $R_{L,opt}$. Because the load voltages at $R_{L,opt}$ are

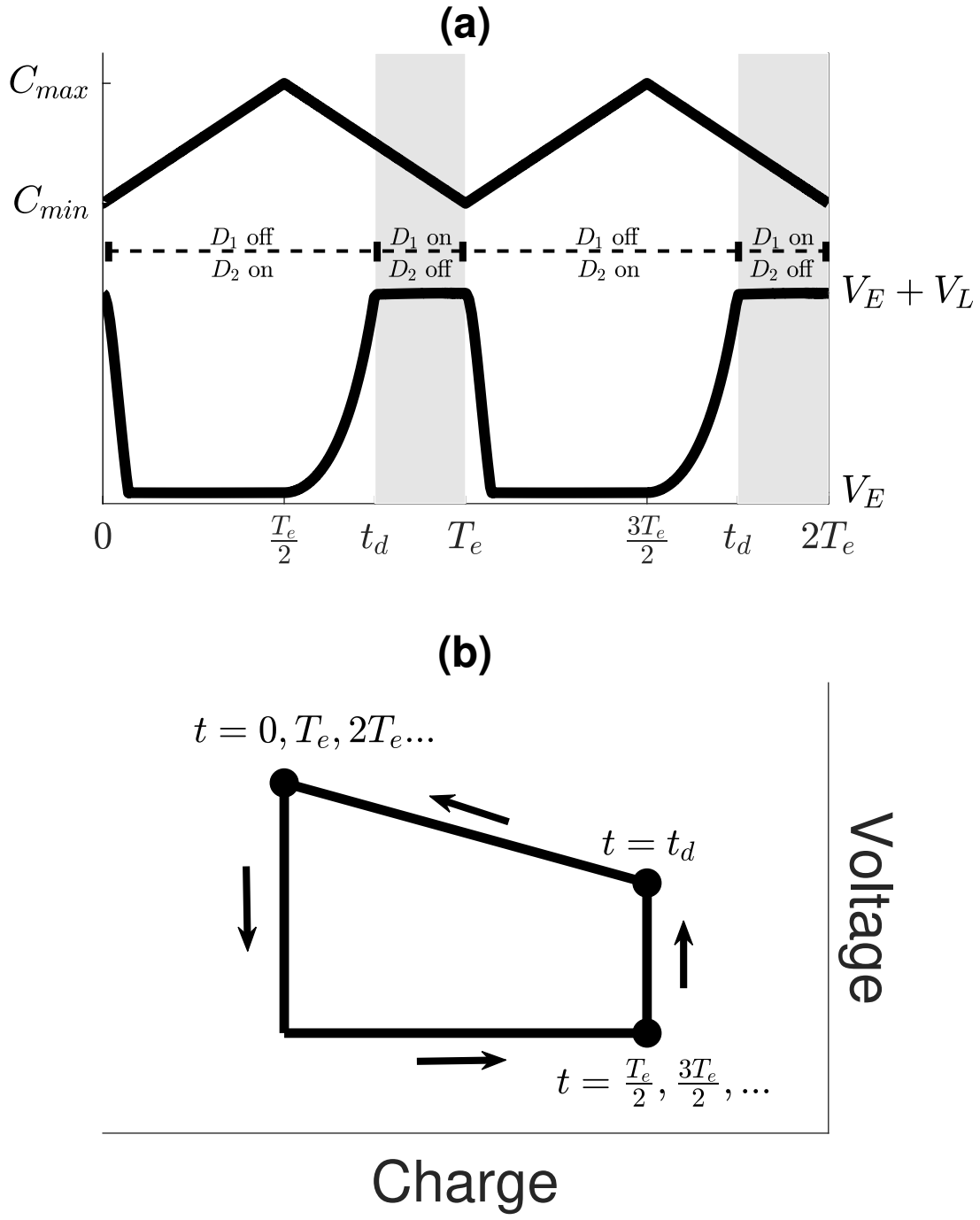

Figure 3.4: (a) Steady-state waveforms of capacitance and machine voltage over two periods, and (b) charge-voltage plane. In reality, the slope of the line from t_d to T_e would be nearly zero since $R_L C_L >> T_e$ but is exaggerated for illustration purposes

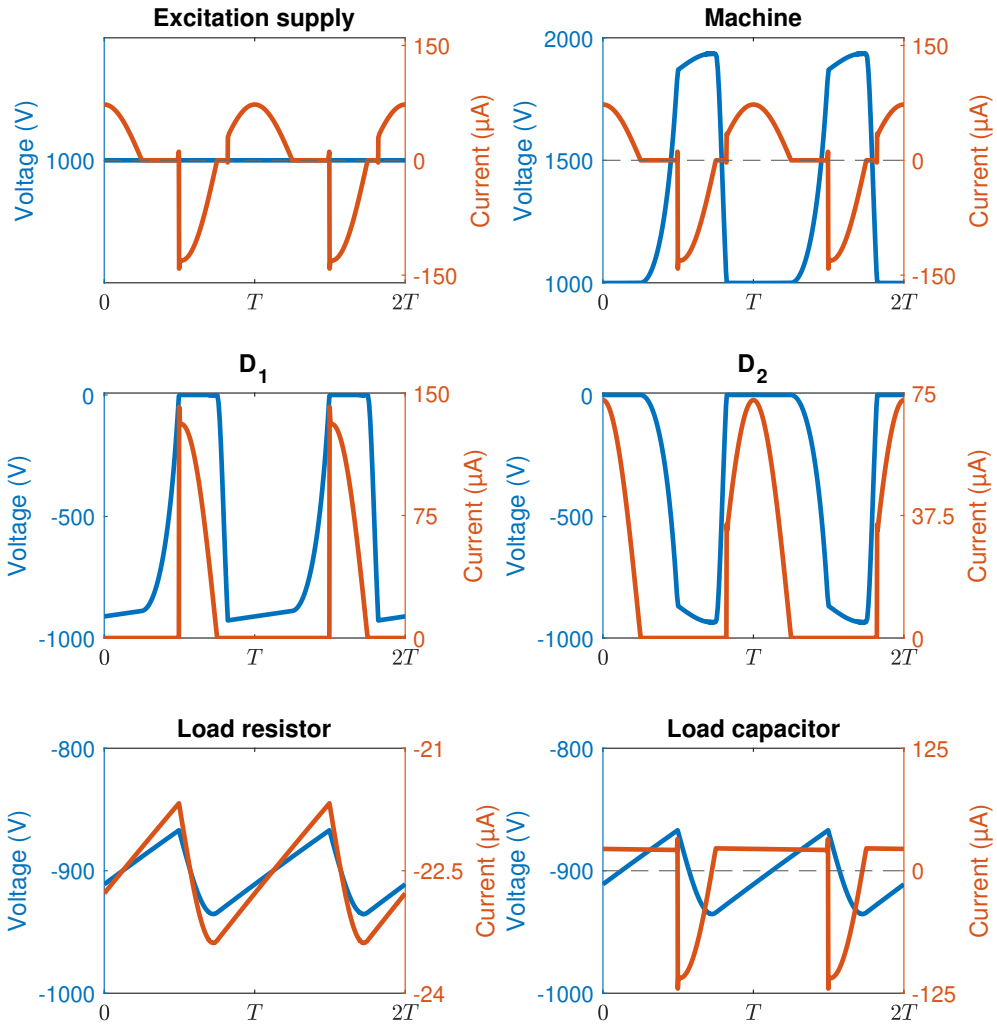

Figure 3.5: Steady-state waveforms of all circuit elements obtained from simulation, with $V_E = 1kV$, $f_e = 50Hz$, $C_{max} = 500pF$, $C_{min} = 25pF$, $R_L = 40M\Omega$, $C_L = 5nF$

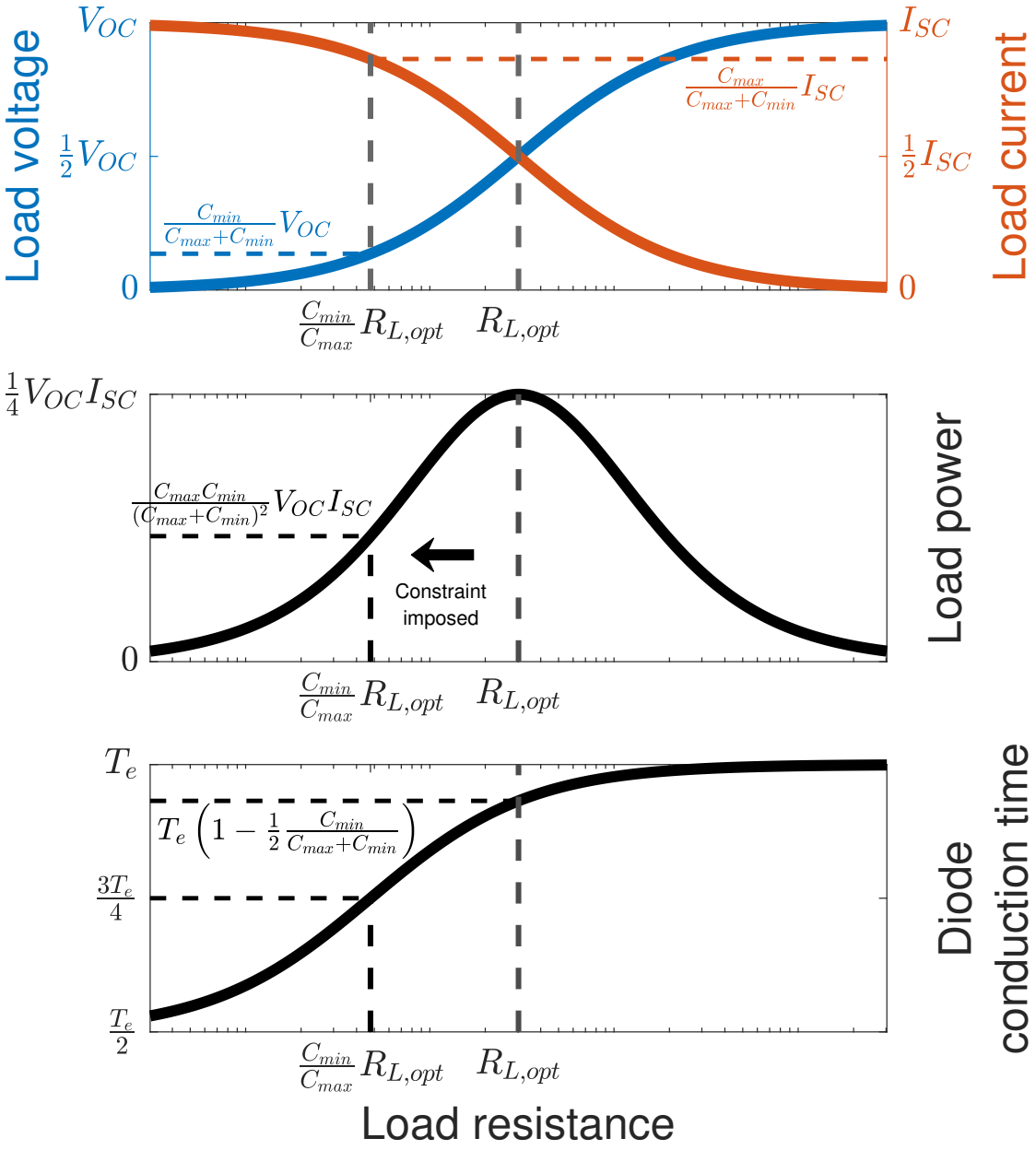

Figure 3.6: Influence of load resistance on terminal properties (voltage, current, and power) and diode conduction time

$\langle V_{L,series} \rangle = \frac{1}{2} V_{OC}$ and $\langle V_{L,parallel} \rangle = V_{OC}$, very large voltages that exceed V_{max} may be produced. This effect is especially acute if $C_{min} << C_{max}$.

More practically, $\langle P_L \rangle$ should be optimized over the two independent variables R_L and V_E subject to the constraint that $V_C < V_{max}$. Under these conditions,

$$V_{E,opt} = \frac{V_{max}}{2} \left(1 + \frac{C_{min}}{C_{max}} \right) \tag{3.14}$$

and

$$R'_{L,opt} \propto \frac{1}{f_e C_{max}}, \tag{3.15}$$

where the $'$ denotes $R_{L,opt}$ when constrained for V_{max}. $R'_{L,opt}$ scales linearly by N for the series connection and inversely by N for the parallel connection. Using these conditions to solve for the remaining parameters, the maximum power that can be obtained from N machines, regardless of whether they are connected in series or in parallel, is

$$\langle P_{L,opt} \rangle = \frac{N}{4} {V_{max}}^2 \Delta C f_e \left(1 - \frac{C_{min}}{C_{max}} \right). \tag{3.16}$$

Several important properties and limitations of using passive electronics with single-phase varying capacitance machinery are revealed upon close examination of Eq. 3.16:

- Referring to Fig. 3.4, the machine only generates every half cycle (during Mode 2 when $\frac{dC}{dt} < 0$). During Mode 1, the machine is motoring since $\frac{dC}{dt} > 0$, corresponding to a significant amount of reactive power circulating within the system.

- Because the diodes in the half-wave rectifier are uncontrolled, power can only be delivered to the load over a portion of the half cycle when $\frac{dC}{dt} < 0$ and is dictated by the machine's capacitance (see Eq. 3.13). In order to take advantage of a greater portion of the available power, active electronics would be necessary.

- Optimizing a varying capacitance machine with passive electronics would yield a different design than one whose output power depends only on ΔC and the load.

Table 3.1: Quantities for N cells connected to an RC load. Note that the approximations are valid when $\Delta C >> C_{min}$.

Parameter	Series	Parallel
Open-circuit voltage	$V_{OC} = NV_E\frac{\Delta C}{C_{min}}$	$V_{OC} = V_E\frac{\Delta C}{C_{min}}$
Short-circuit current	$I_{SC} = V_E\Delta C f_e$	$I_{SC} = NV_E\Delta C f_e$
Load voltage	$\langle V_L\rangle = V_E\frac{\Delta C}{\frac{1}{f_e R_L} + \frac{C_{min}}{N}}$	$\langle V_L\rangle = V_E\frac{\Delta C}{\frac{1}{Nf_e R_L} + C_{min}}$
Load current	$\langle I_L\rangle = V_E\frac{\Delta C}{\frac{1}{f_e} + \frac{R_L C_{min}}{N}}$	$\langle I_L\rangle = V_E\frac{\Delta C}{\frac{1}{Nf_e} + R_L C_{min}}$
Load power	$\langle P_L\rangle = {V_E}^2\frac{\Delta C^2 R_L}{\left(\frac{1}{f_e} + \frac{R_L C_{min}}{N}\right)^2}$	$\langle P_L\rangle = {V_E}^2\frac{\Delta C^2 R_L}{\left(\frac{1}{Nf_e R_L} + C_{min}\right)^2}$
Unconstrained optimal load	$R_{L,opt} = \frac{N}{f_e C_{min}}$	$R_{L,opt} = \frac{1}{Nf_e C_{min}}$
Constrained optimal load	$R'_{L,opt} = \frac{N}{f_e C_{max}}$	$R'_{L,opt} = \frac{1}{Nf_e C_{max}}$
Bias voltage at $R'_{L,opt}$	$V_{E,opt} = \frac{V_{max}}{2}\left(1 + \frac{C_{min}}{C_{max}}\right) \approx \frac{V_{max}}{2}$	
Load voltage at $R'_{L,opt}$	$\langle V_{L,opt}\rangle = N\frac{V_{max}}{2}\left(1 - \frac{C_{min}}{C_{max}}\right) \approx N\frac{V_{max}}{2}$	$\langle V_{L,opt}\rangle = \frac{V_{max}}{2}\left(1 - \frac{C_{min}}{C_{max}}\right) \approx \frac{V_{max}}{2}$
Load current at at $R'_{L,opt}$	$\langle I_{L,opt}\rangle = \frac{V_{max}}{2} f_e \Delta C$	$\langle I_{L,opt}\rangle = N\frac{V_{max}}{2} f_e \Delta C$
Load power at $R'_{L,opt}$	$\langle P_{L,opt}\rangle = \frac{N}{4}{V_{max}}^2\Delta C f_e\left(1 - \frac{C_{min}}{C_{max}}\right) \approx \frac{N}{4}{V_{max}}^2\Delta C f_e$	
Diode conduction time at $R'_{L,opt}$	$t_d = \frac{3}{4}T$	

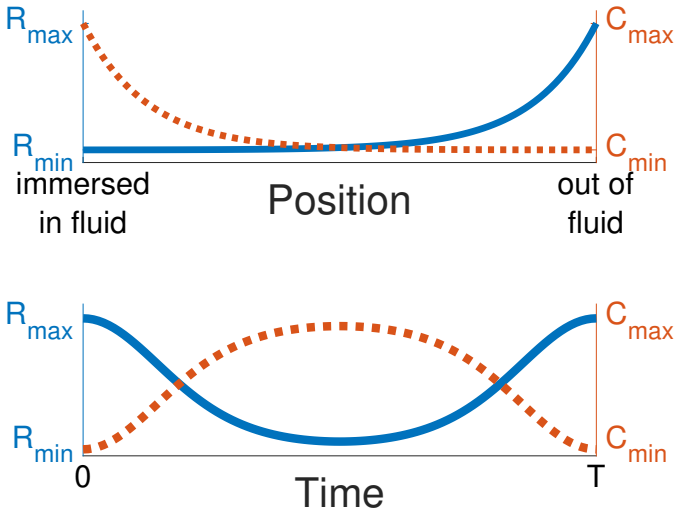

Figure 3.7: Example of leakage resistance and capacitance of dielectric liquid filled capacitor as a function of position (top) and as a function of time (bottom)

3.5 Effect of Charge Leakage

In the previous sections, analysis was conducted on a machine with a perfectly insulating dielectric. However, there could be charge leakage due to the dielectric having finite resistivity or from the ionization of a gaseous dielectric medium (i.e., corona discharge). This charge leakage can be represented as a resistance R_{leak} in parallel with $C(t)$. Although R_{leak} may be position-dependent (e.g., in a dielectric liquid-filled variable capacitor, R_{leak} changes as the dielectric fluid ebbs and flows), making it a time-dependent quantity (see Fig. 3.7), only the average value per cycle will be considered in this analysis for simplicity's sake.

Although a practical varying capacitance system would require a rectifier, the rectifier will be removed in this analysis and the variable capacitor will simply be connected to R_L (see Fig. 3.8). Including the effect of charge leakage requires analysis with instantaneous quantities, which is considerably more challenging with non-linear circuit elements such as diodes. Furthermore, the focus of this analysis is to generalize the effect of charge leakage on efficiency, which can be more easily understood without the rectifier.

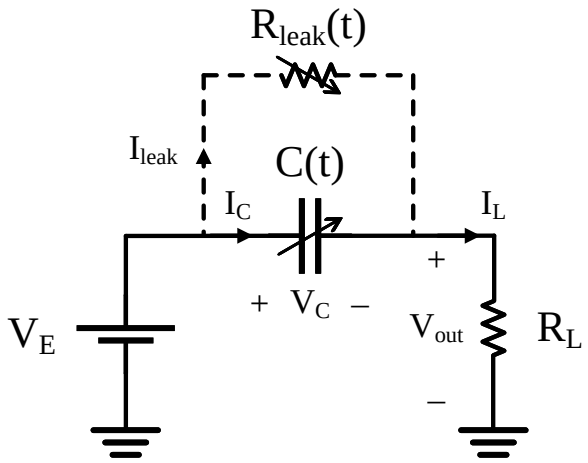

Figure 3.8: Varying capacitance machine with charge leakage R_{leak} connected to a resistive load and no rectifier

Because the capacitance of the capacitor can vary with time, the current through the capacitor consists of an extra term in addition to the familiar term corresponding to the circulation of current between the capacitor and source,

$$I_C(t) = \dot{Q}(t) = \dot{C}(t)V_C(t) + C(t)\dot{V}_C(t). \tag{3.17}$$

The $\dot{C}(t)V_C(t)$ term is akin to the "speed EMF" voltage in magnetic machinery that represents electromechanical energy conversion. Bearing this in mind, the following nonlinear ordinary differential equation (ODE) fully describes the system:

$$\dot{C}(t)V_C(t) + C(t)\dot{V}_C(t) + \frac{V_C(t)}{R_{leak}} = \frac{V_E - V_C(t)}{R_L}. \tag{3.18}$$

In [38], analysis on a lossless system using a sinusoidally-varying $C(t)$ is presented but expresses solutions in terms of Bessel functions, making it difficult to physically interpret. Alternatively, a closed-form solution to Eq. 3.18 in terms of elementary functions can be obtained if the capacitance is modeled as a piecewise triangle waveform of the form $C(t) = C_0 + C_1 tri\left(\frac{t}{T_e}\right)$ where where $C_0 > C_1$ such that $C(t) > 0$, $C_0 = \frac{1}{2}(C_{min} + C_{max})$, and $C_1 = \frac{1}{2}(C_{min} - C_{max})$ (see Fig. 3.9a):

$$C(t) = \begin{cases} C_0 - C_1 + \frac{4C_1}{T_e}\left(t - (n-1)T_e\right), & (n-1)T_e \le t < \frac{2n-1}{2}T_e, \\ C_0 + C_1 - \frac{4C_1}{T_e}\left(t - \frac{2n-1}{2}T_e\right), & \frac{2n-1}{2}T_e \le t < nT_e. \end{cases} \tag{3.19}$$

During the first half period of $C(t)$ with the initial condition $V_C(0) = V_E\left(\frac{R_{leak}}{R_{leak}+R_L}\right)$, $\dot{C} > 0$, so

$$V_C(t) = \frac{V_E}{T_e(1+\frac{R_L}{R_{leak}})+\tau}\left(T_e + \frac{\tau}{1+\frac{R_L}{R_{leak}}}\left(\frac{T_e(C_0-C_1)}{\frac{\tau}{R_L}t + T_e(C_0-C_1)}\right)^{\gamma}\right), \tag{3.20}$$

where

$$\tau = 4R_LC_1 = 2R_L\Delta C, \tag{3.21}$$

representing the time constant of the electromechanical system, and

$$\gamma = \frac{1}{\tau}\left(T_e\left(1+\frac{R_L}{R_{leak}}\right)+\tau\right). \tag{3.22}$$

For the second half period of $C(t)$ when $\dot{C} < 0$, the initial condition is set to the value of Eq. 3.20 at $t = \frac{T_e}{2}$, resulting in

$$\begin{aligned} V_C(t) = \frac{V_E}{T_e(1+\frac{R_L}{R_{leak}})-\tau}\Bigg(T_e - \\ \left(\frac{\frac{\tau}{R_L}(\frac{3}{4}T_e - t) + C_0T_e}{T_e(C_0+C_1)}\right)^{\gamma}\Bigg(T_e - \\ \frac{T_e(1+\frac{R_L}{R_{leak}})-\tau}{T_e(1+\frac{R_L}{R_{leak}})+\tau}\Bigg(T_e + \\ \frac{\tau}{1+\frac{R_L}{R_{leak}}}\left(\frac{C_0-C_1}{C_0+C_1}\right)^{\gamma}\Bigg)\Bigg)\Bigg). \end{aligned} \tag{3.23}$$

The load current I_L can be derived as

$$I_L(t) = \frac{V_E - V_C(t)}{R_L} \tag{3.24}$$

and the power dissipated in the resistor as

$$P_L(t) = \widetilde{i}_L(t)^2 R_L = \frac{\widetilde{v}_L(t)^2}{R_L} \tag{3.25}$$

where $\widetilde{i}_L(t)$ and $\widetilde{v}_L(t)$ represent the AC component of $I_L(t)$ and $V_C(t)$, respectively. Because the DC components of $I_L(t)$ and $V_C(t)$ merely correspond to charging the capacitor, only the AC components are of interest since they represent the electromechanical power conversion in the system.

The losses from charge leakage can simply be taken as

$$P_{loss} = \frac{V_C(t)^2}{R_{leak}}, \tag{3.26}$$

allowing the efficiency to be expressed as

$$\eta = \frac{P_L}{P_{in}} = \frac{P_L}{P_L + P_{loss}}. \tag{3.27}$$

The voltage across the variable capacitor (Eq. 3.20 and 3.23) and the load current (Eq. 3.24) are plotted for two periods of $C(t)$ in Fig. 3.9b-3.9c, respectively. In Fig. 3.9d, the instantaneous power dissipated by the load resistor is depicted (Eq. 3.25). Fig. 3.9e provides an alternative perspective on the dynamics of the circuit with the charge-voltage plane of the variable capacitor. Note that the area under Fig. 3.9e corresponds to the energy in the system [13].

An important criterion regarding acceptable levels of R_{leak} can be gleaned by looking at the expressions for $V_C(t)$. In order for R_{leak} to have a minimal effect on $V_C(t)$, it is clear that

$$T_e << 4R_{leak}C_1 = \tau\frac{R_{leak}}{R_L} \tag{3.28}$$

or, in terms of ΔC,

$$T_e << 2R_{leak}\Delta C. \tag{3.29}$$

In other words, the time that it takes for charges to migrate within the dielectric medium

must be far greater than the mechanical response of the electromechanical system, which is dictated by the period of $C(t)$. These results are consistent with charge relaxation theory, which relates the time τ_c it takes charges to distribute themselves within some insulating medium to the permittivity ϵ and conductivity σ of that insulator as $\tau_c = \frac{\epsilon}{\sigma}$ [39]. Analogously, τ_c should be far greater than T_e such that charges cannot be conducted through the capacitor's dielectric. However, it is useful to employ the criteria as defined by Eq. 3.28-3.29 since they utilize measurable quantities that may deviate from their nominal material properties.

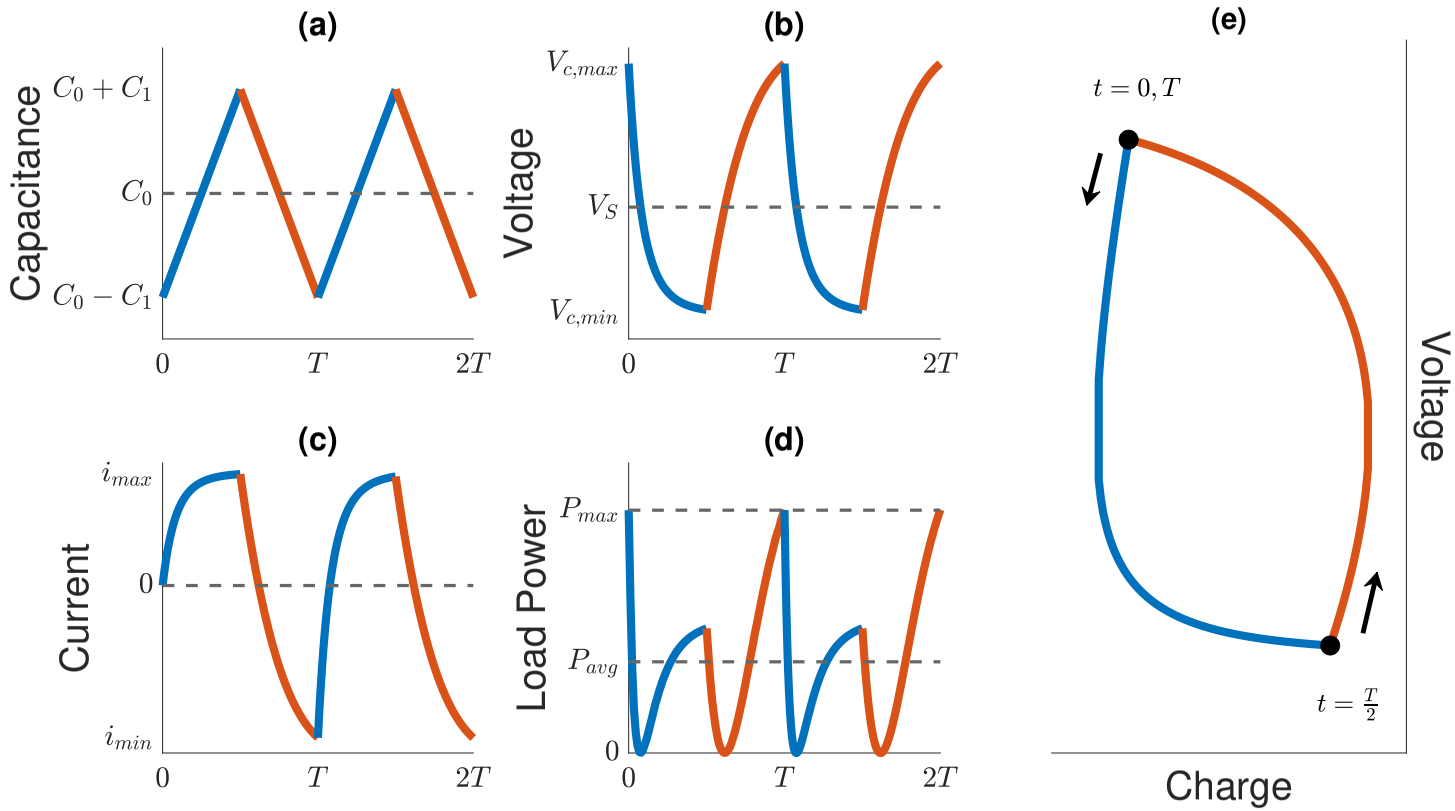

Figure 3.9: (a) $C(t)$ modeled as triangle function (b) Voltage response of variable capacitor to a triangle capacitance function (c) Current response (d) Power dissipated in resistive load (e) Charge-voltage energy plane with the change in state in the counter-clockwise direction. In all plots, the blue line corresponds to the system absorbing electrical energy and delivering mechanical energy ($\frac{dC}{dt} > 0$), and the orange line corresponds to the system absorbing mechanical energy and delivering electrical energy ($\frac{dC}{dt} < 0$).

Chapter 4

Experimental Study of Rotating Varying Capacitance Machinery

If there is no other use discovered of electricity, this however is considerable, that it may make a vain man humble.

— Benjamin Franklin

This section presents results of experiments conducted to verify the analytical model derived in Section 3. Experiments were conducted on two distinct rotating varying capacitance systems, the first consisting of one-pole machines and the second consisting of customized 18-pole machines. The two systems are then compared, demonstrating a 3x improvement in power density with the 18-pole machines.

4.1 Isolated excitation system

Because each machine requires isolated excitation, a custom excitation system had to be designed and built. To have both galvanic isolation and uniformity among the excitation V_E supplied to each machine, a transformer with multiple secondary windings was necessary. The number of secondary windings is dictated by the number of machines that need to be excited. The input to the transformer was provided by a tunable autotransformer

(commonly known as a "variac"), which was connected to the mains electricity. To prevent sparking between the windings of the transformer, an Austin ring transformer design was employed (see Fig. 4.1). A toroidal iron core with 749 turns wrapped around its entire circumference was used as the primary side, and five clusters of 80 turns each were wound around a segment of the core (over the primary windings) to realize five secondary windings with a turns ratio of $9.36 : 1$. A 3D-printed structure was used to separate each of the five secondary windings from the primary and other secondary windings by a large air gap. The entire assembly was then immersed in a liquid varnish to provide further insulation.

After being rectified and filtered by a full-wave bridge rectifier with an RC filter, the output of each secondary was fed into an XP EMCO F50 DC/DC converter capable of producing voltages up to 5 kV with an input of 0.7 to 15 V. Thus, by tuning the variac, a uniform value of V_E for each machine could be specified. Fig. 4.2 shows a schematic of the excitation system, and Fig. 4.3 shows the built system.

As shown in Fig. 4.4, the deviation of the individual DC/DC converter's outputs from the average of the five outputs was small. For $V_E > 1kV$, the maximum deviation of any individual V_E from the average was $\pm$ 2.5%. At lower voltages ($V_E < 100V$), the maximum percent deviation was $\pm$15%.

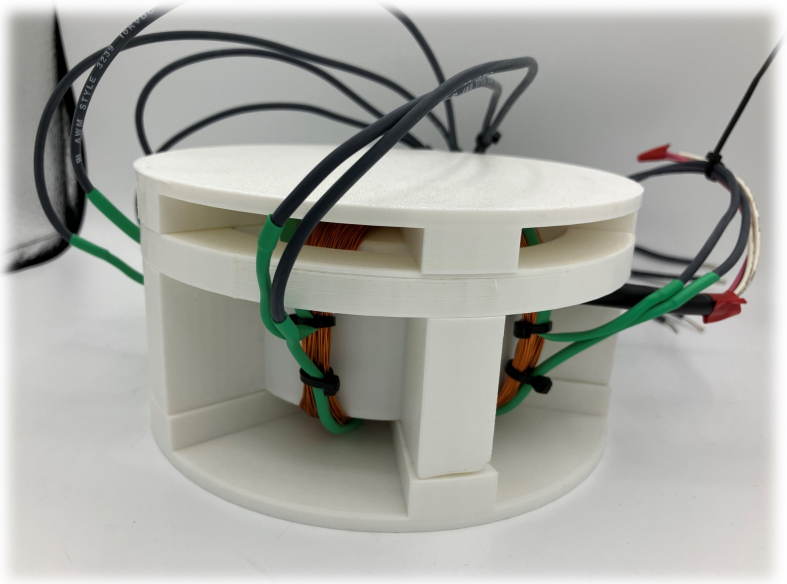

Figure 4.1: Custom-made Austin ring transformer before being submerged in insulating varnish

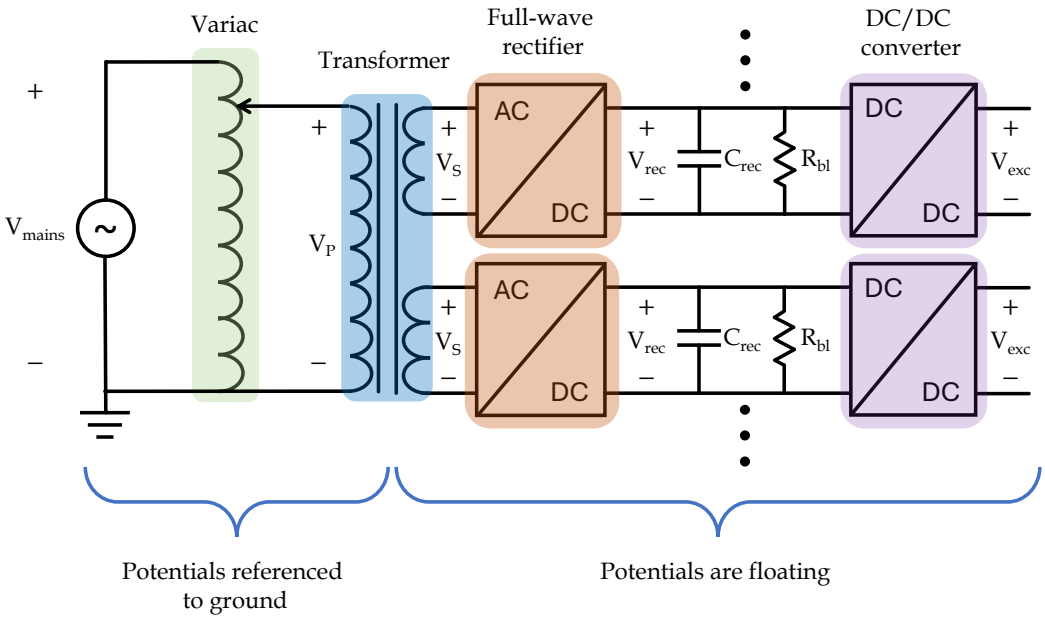

Figure 4.2: Schematic of system used to realize isolated voltage excitation for each machine

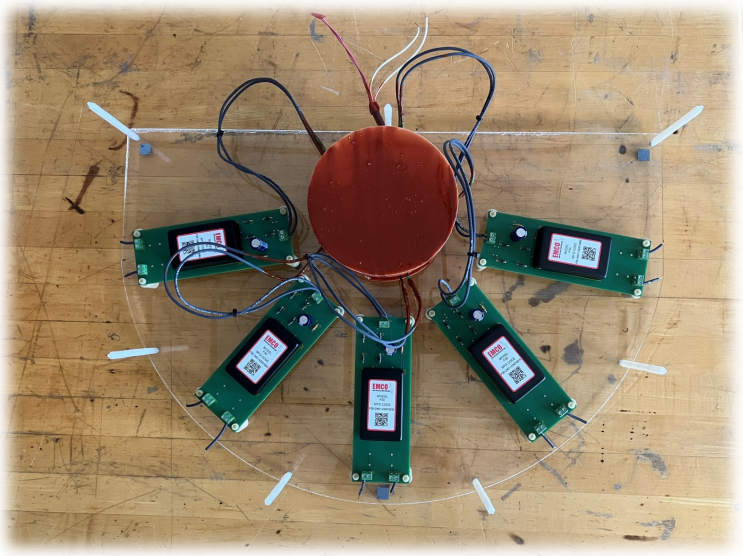

Figure 4.3: Isolated excitation system

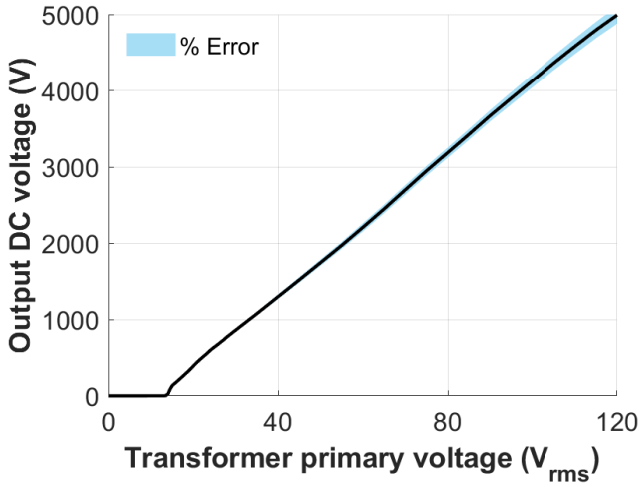

Figure 4.4: Average output voltage V_E as a function of input variac voltage for excitation system.

4.2 One-pole machine

While the overall goal of these experiments was to validate the analytical model, a secondary aim of the experiments with the one-pole machines was to demonstrate the ability of varying capacitance machines to produce high voltages from relatively smaller excitation levels. As was demonstrated in the derivation of the open-circuit voltage (see Eq. 3.6), large output voltages can be generated if $C_{max} >> C_{min}$. For machines with low pole counts, C_{min} will be very small since the physical distance between out-of-phase poles is large enough to mitigate stray capacitances.

4.2.1 Setup

Five single-pole prototype machines were used during the first set of experiments (see Fig. 4.5). These machines were adapted from an existing tunable capacitor design sold by Oren Elliot Products LLC to accommodate high-speed operation. In addition to using ball bearings, counterweights were added to the machines to counteract weight imbalances (counterweights are the brass-colored segments in Fig. 4.5). This weight imbalance arose from one half of the stator plates being connected to the bottom of the machine body, and the other half being connected to the top. The rotor plates were split up and distributed along the shaft in a similar fashion. This configuration allowed for an easy way to apply positive and negative voltages to the machine, since each stator plate of each polarity was separated from the other. However, having the stators and rotors split up in this way imposed an imbalance in the machine's weight distribution, necessitating counterweights to prevent wobbling during high-speed operation.

Shaft couplers were used to mechanically connect the machines and create a common shaft, and a servo motor acted as the prime mover. The shaft of each machine was made of an insulating material, so even though each machine was mechanically connected with each other, they were electrically isolated from one another. The machines were then mounted

on a long, thin sheet of Delrin and inserted in a protective polycarbonate tube (see Fig. 4.6). Precision shims were used to raise each machine to a uniform height, such that all of the shafts were aligned with one another. The rotors of each machine were skewed by $\frac{360^\circ}{N} = 72^\circ$ relative to one another to reduce ripple. This skewing of the rotors is evident in Fig. 4.8-4.9, as there are distinct pulses in the load voltage waveform corresponding to the instances that each machine is delivering power to the load. To properly skew the rotors, the rotor of each machine was turned until the capacitance measured by the impedance analyzer recorded the proper fraction of C_{max}. Once the rotor was in proper position, it was locked in place by tightening its shaft couplers.

The machines made use of a "floating" rotor (i.e., rotor electrodes at floating potential), such that no brush contact was needed to excite the rotor electrodes. As a result, the terminal capacitance of the machine equaled the series combination of the positive stator-to-rotor capacitance C_{s+r} and the negative stator-to-rotor capacitance C_{s-r}. With an air gap of 0.5 mm, the rated maximum voltage (in air) was 3 kV, and $C_{min} = 30 \pm 5pF$ and $C_{max} = 500pF$. The difference among each of the five machines' electrical characteristics was minimal. The electrodes were 0.76-mm thick.

4.2.2 Short-circuit testing

To confirm the equivalent representation of the system as a current source, short circuit testing was conducted on the system in both the series and parallel configurations. Because the current levels in the system were in the range of μA, directly measuring the current was ruled out. Instead, the voltage was measured with an oscilloscope across a small load resistor whose resistance was many orders of magnitude lower than the input impedance of the machine, such that the load would act as a short circuit from the machine's perspective. In both configurations, the measured short circuit current scaled linearly with both rotational speed and excitation (see Fig. 4.10). In all cases, the measured values were within 5% of the expected values.

It is also clear from Fig. 4.10 that the short circuit current scaled linearly by the

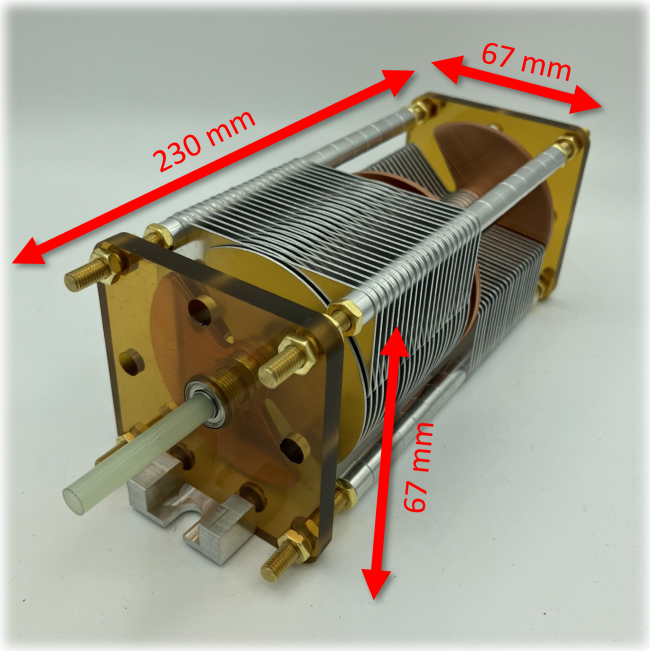

Figure 4.5: Prototype of single-pole machine

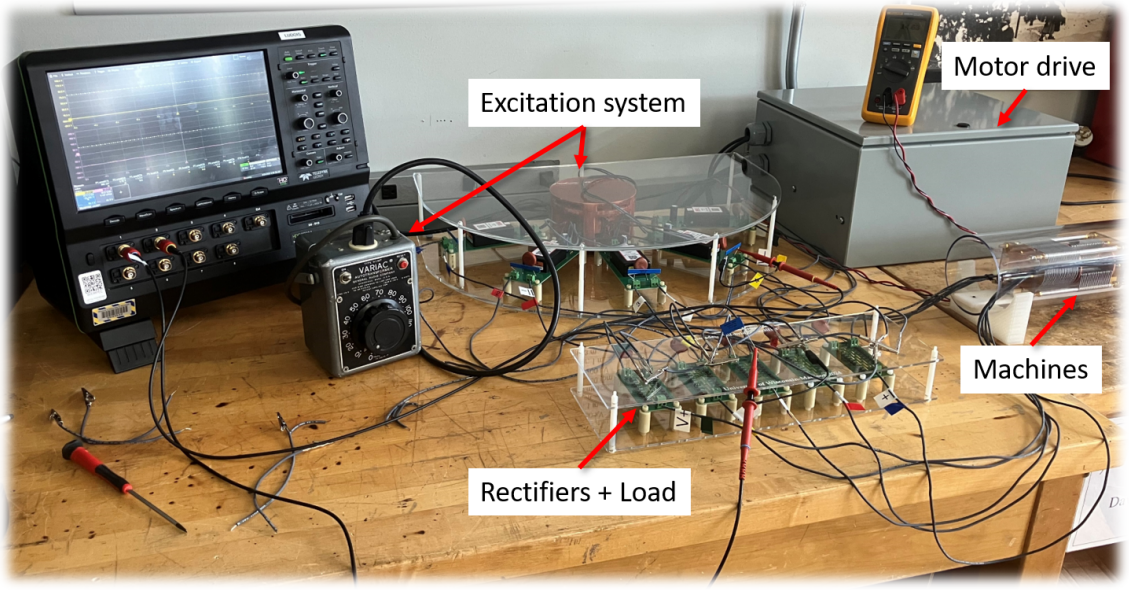

Figure 4.6: Experimental setup on lab bench.

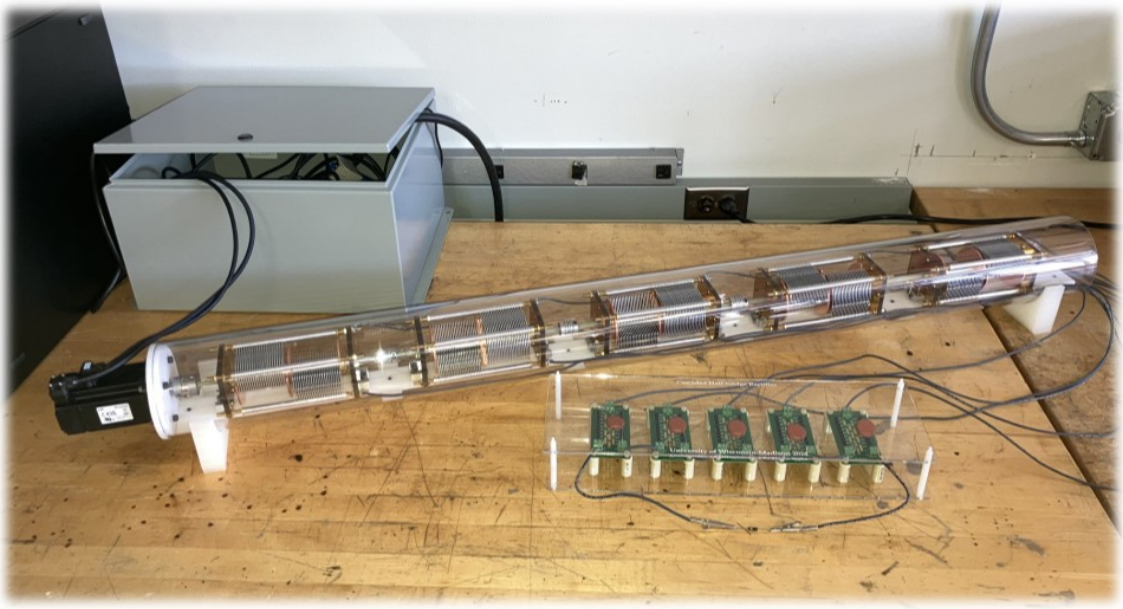

Figure 4.7: Full view of machines used in experiments

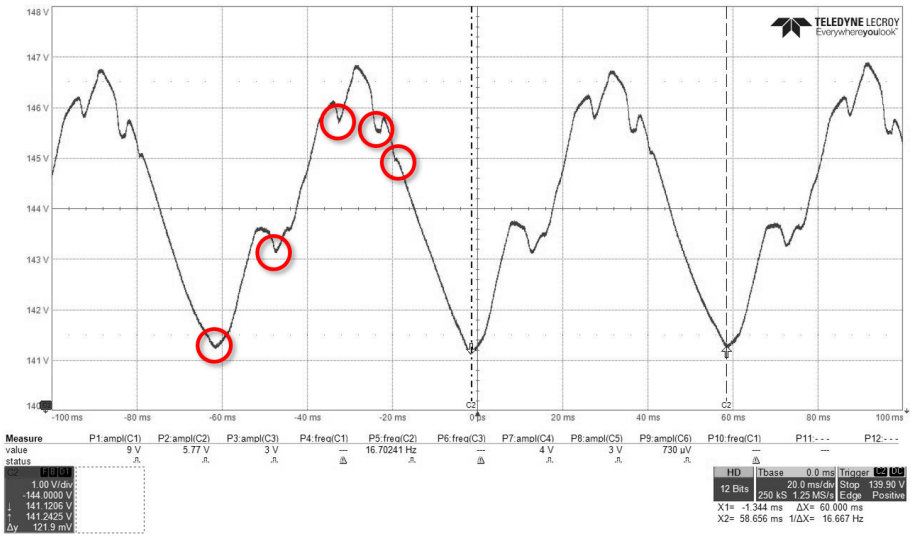

Figure 4.8: Oscilloscope capture of load voltage to show pulses from each machine when five one-pole machines are connected in series and skewed by 72° relative to one another. The input parameters were $\omega_m = 1000rpm$, $V_E = 250V$, and $R_L = 600M\Omega$.

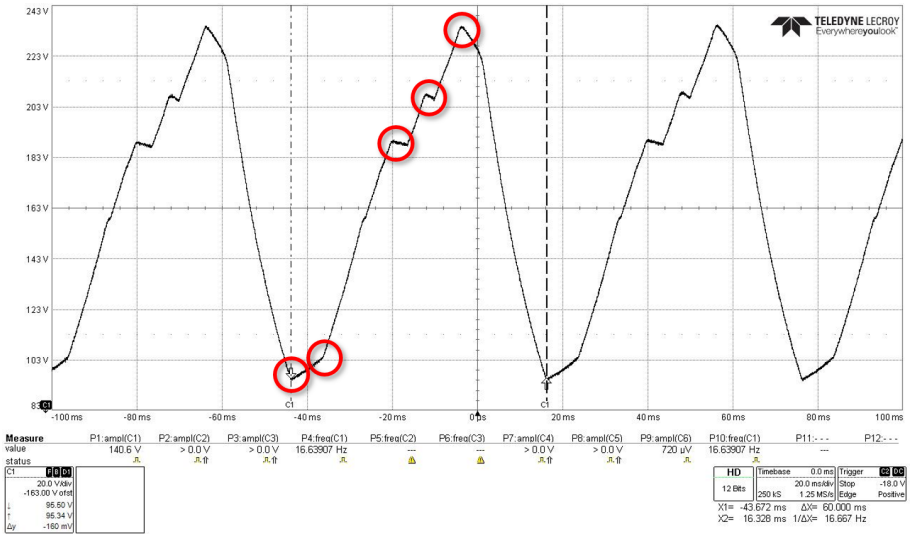

Figure 4.9: Oscilloscope capture of load voltage to show pulses from each machine when five one-pole machines are connected in parallel and skewed by 72° relative to one another. The input parameters were $\omega_m = 1000rpm$, $V_E = 250V$, and $R_L = 24M\Omega$.

number of machines N when the machines were connected in parallel, such that

$$I_{SC,par} = NV_E\Delta C f_e. \tag{4.1}$$

However, the number of machines had no influence on the short circuit current for the series configuration, as was expected.

4.2.3 Output power as a function of load, excitation, and number of machines

The output power was measured as a function of R_L, V_E, and N and compared with the analytical expressions provided in Table 3.1. An RC load was used in all testing and as the values of R_L changed, C_L was also modified to ensure that $R_L C_L >> T_e$.

In the first test, V_L, I_L, and P_L were measured and plotted against a sweep of three decades of R_L for both the series and the parallel configurations at a constant speed of 2000 rpm (see Fig. 4.11). Within each decade, four logarithmically spaced values of R_L were used. In both configurations, a small excitation voltage was used ($V_E < 100V$) to ensure that as R_L approached open-circuit levels, V_L would not exceed the maximum voltage

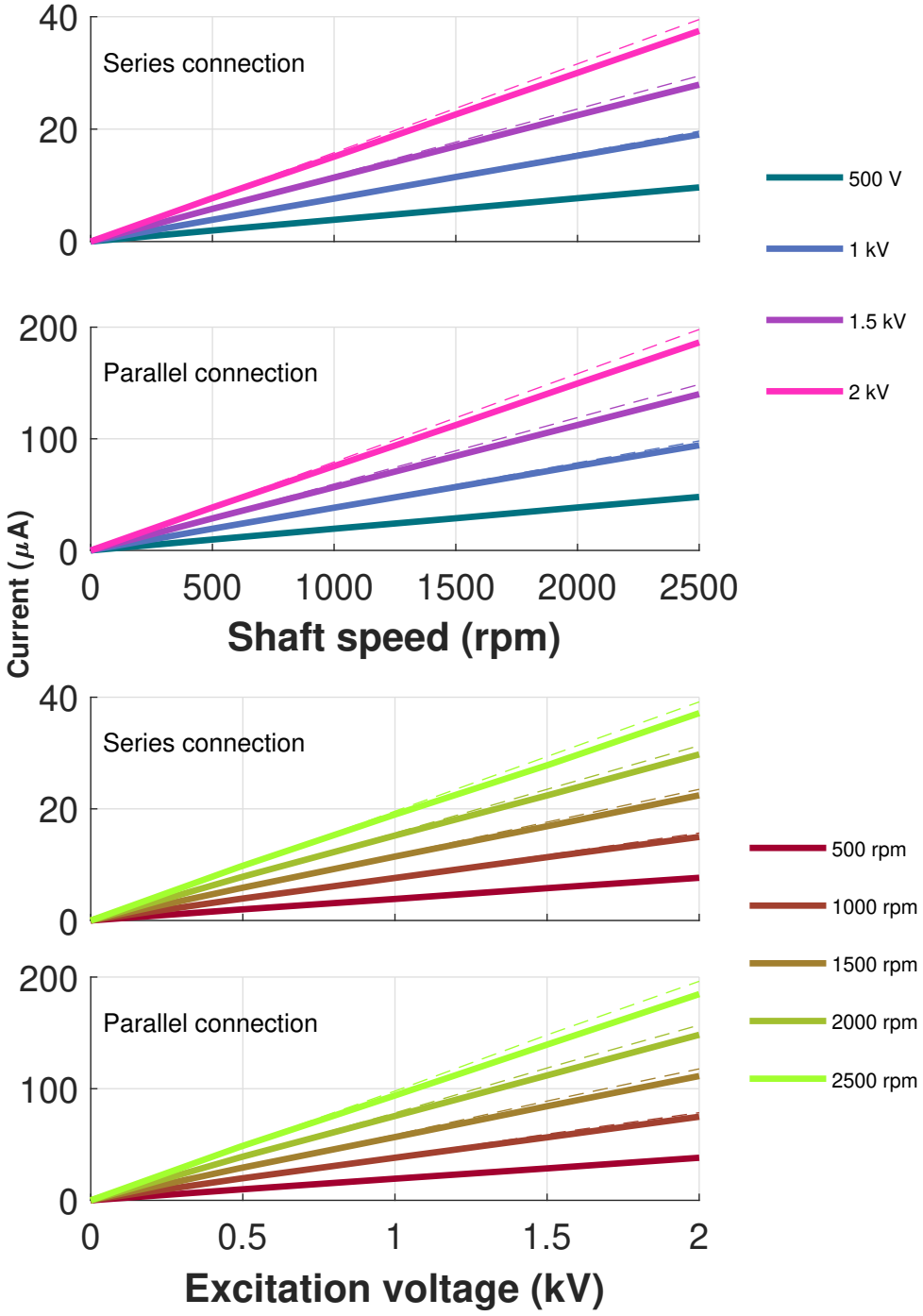

Figure 4.10: Short circuit currents for series and parallel connection of five one-pole machines as a function of shaft speed (top two plots) and excitation voltage (bottom two plots). The solid line represents measured values, and the dashed line represents expected values.

rating of the machines. In contrast to the short-circuit current, the load parameters are very sensitive to C_{min} when $R_L >> 0$, so the expected values are represented in Fig. 4.11 with a tolerance band. This tolerance band also takes into account the uncertainty with V_E, which is much greater at the lower voltages used in this load sweep compared with those used during the short-circuit testing. Based on the diagrams in Fig. 4.11, it is clear that the measured values correspond with the expected behavior over the entire range of R_L.

To determine the maximum power capacity of the system, the power dissipated in a resistor at a constant speed of 2500 rpm was recorded as a function of V_E (see Fig. 4.12). Based on the optimum expressions derived in Table 3.1, it was expected that the maximum V_E that could be used before sparking would occur would be no more than 1.5 kV, since $V_{E,opt} \approx \frac{V_{max}}{2}$. At 2500 rpm, $R_{L,series}$ and $R_{L,parallel}$ were set to 250 $M\Omega$ and 9.6 $M\Omega$, respectively, using the relationships in Table 3.1. At $V_E = 1.4kV$, the maximum power recorded for the system was 0.136 W in the series configuration, corresponding to $V_L = 5890V$. The slight discrepancy between the measured and expected P_L is likely due to losses in the diodes, which were not modeled.

To confirm the modularity of the proposed topology, P_L was recorded as a function of the number of machines connected together, for both the series and parallel configurations. V_E was set to 1 kV, and the motor was spun at 1000 rpm. It is clear from Fig. 4.13 that the output power scales linearly by N, regardless of how the machines are connected.

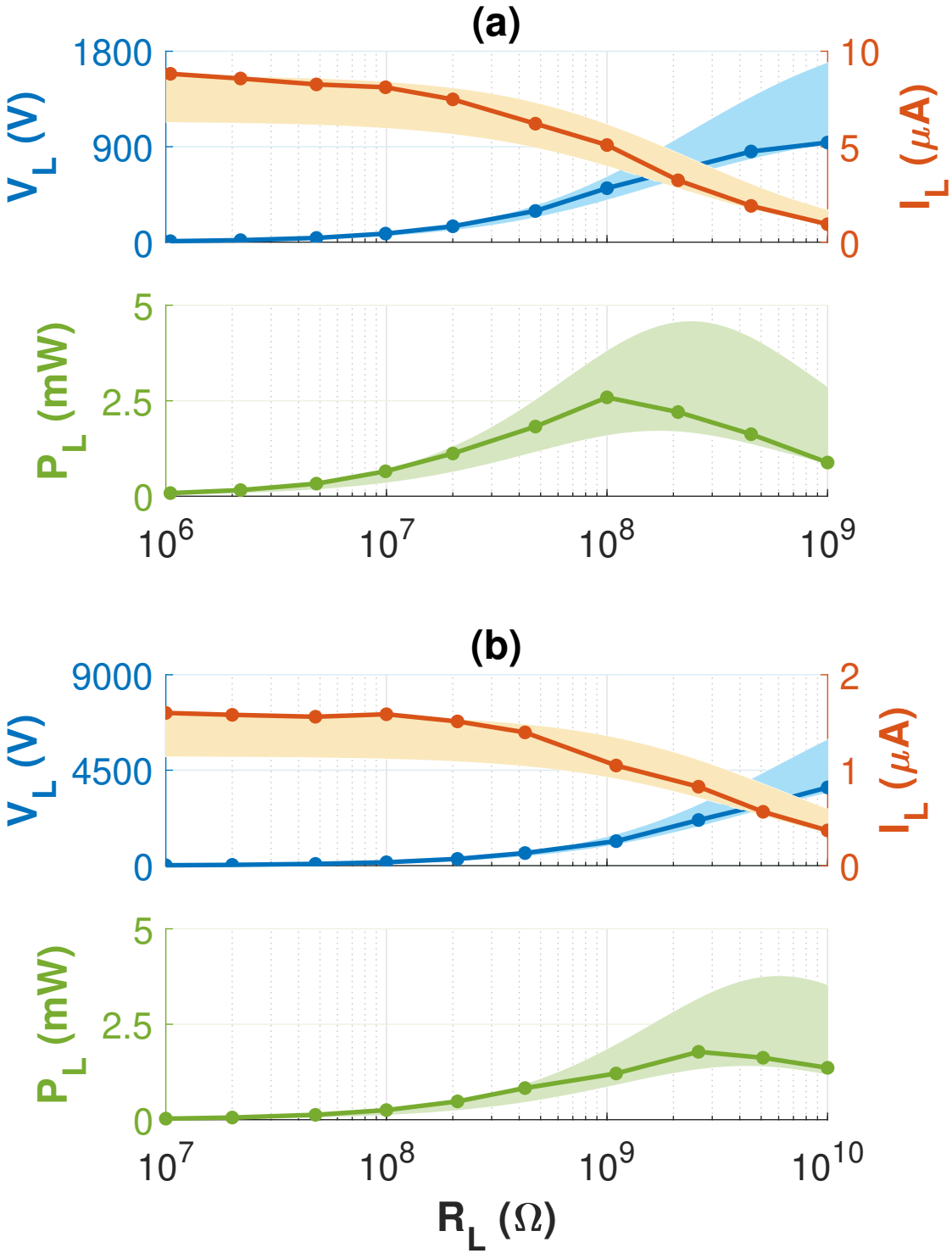

Figure 4.11: Load sweep of single-pole machines at 2000 rpm (a) connected in series with $V_E = 87 \pm 13V$, and (b) connected in parallel with $V_E = 96 \pm 14V$. The tolerance in the expected values (shown in shaded region) takes into account the uncertainty with V_E ($\pm$ 15%) as well as C_{min} ($\pm$ 5 pF).

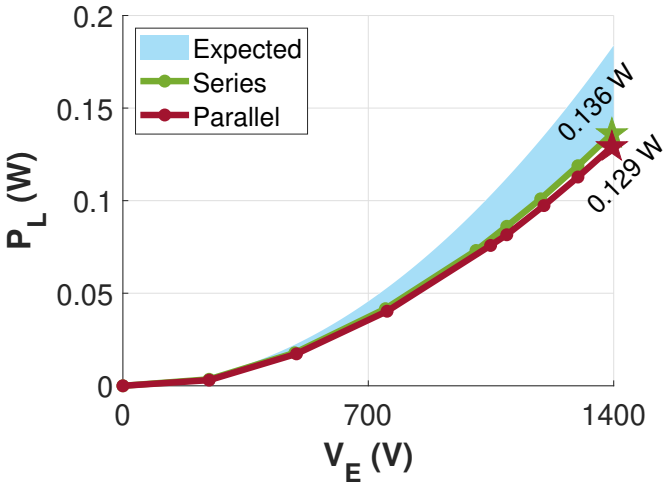

Figure 4.12: Maximum power testing of single-pole machines, with P_L vs. V_E at rotational speed of 2500 rpm. The tolerance in the expected values takes into account the uncertainty with V_E ($\pm$ 2.5%) as well as C_{min} ($\pm$ 5 pF).

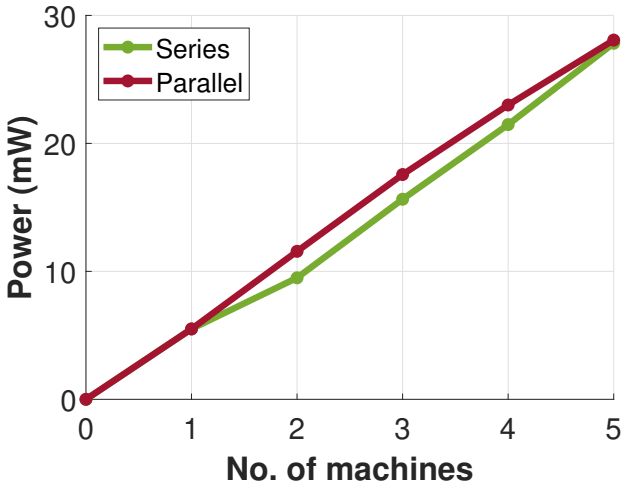

Figure 4.13: Scaling of system power by the number of machines, P_L vs. N, at 1000 rpm and $V_E = 1$ kV.

4.3 18-pole machine

While the single-pole machines yielded promising results, their design was sub-optimal from the perspective of power generation, which is related to $\frac{\Delta C}{\Delta \theta}$. The aim of these next experiments was to demonstrate that the output power of varying capacitance machines could be improved by optimizing the geometry of the electrodes for $\frac{\Delta C}{\Delta \theta}$.

4.3.1 Optimization of 18-pole electrode geometry

To facilitate a fair comparison between the single-pole and the 18-pole designs, the dimensions of the new 18-pole design were kept as close to the original single-pole design as possible. This meant that the air gap, plate thickness, and radius of the plates were kept the same.

To determine the optimal design, Ansys Maxwell FEA was used to calculate the capacitance of candidate designs in the following manner:

- For each pole count, a rotor and stator pair with 0.76-mm thick electrodes separated by a 0.5-mm air gap were drawn natively in Ansys Maxwell. The angular width of the pole (also known as the span) was parametrized, such that a range of values could be assigned to it.

- The pole span was swept from one-tenth of its maximum value to its maximum value, and the capacitance was calculated at each pole span. This sweep was run when the rotor and stator poles were in phase with one another (to determine C_{max}) and when they were out of phase with one another (to determine C_{min}).

- The raw C_{max} and C_{min} data was then processed in MATLAB to determine which pole span yielded the greatest $\frac{\Delta C}{\Delta \theta}$ for that specific pole count.

- This process was repeated for all pole counts considered.

The results of the FEA optimization are shown in Fig. 4.14. It is clear that increasing the pole count increases $\frac{\Delta C}{\Delta \theta}$ up to a certain point since the electrical frequency scales by

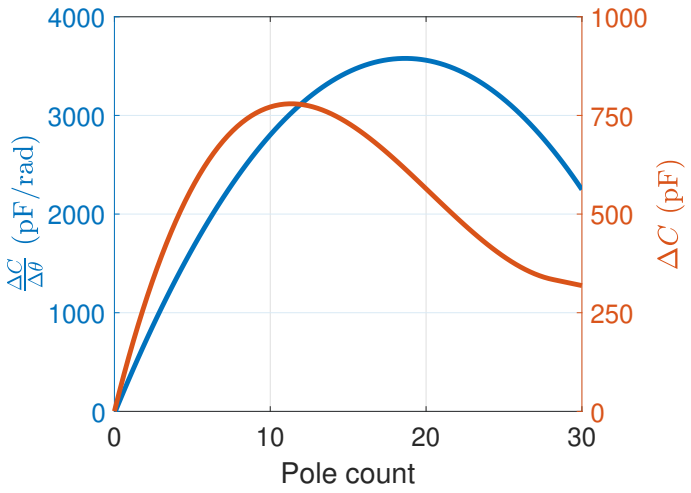

Figure 4.14: Results of FEA optimization on Oren Elliot prototype (for a single rotor-stator pair)

the pole count, since

$$\frac{\Delta C}{\Delta \theta} = \frac{\Delta C}{\pi / \mathcal{P}}. \tag{4.2}$$

However, as the pole count increases, stray capacitance increases C_{min}, which reduces ΔC. For this particular design, the optimal pole count was found to be 18, with a rotor pole span of 9.44°and a stator pole span of 11.25°. Visualizations of these electrode designs are shown in Fig. 4.15-4.16.

4.3.2 Setup

The optimized electrode designs were sent to Oren Elliot Products for manufacturing. In addition to having a new electrode design, the new 18-pole machines were constructed with a conducting rather than insulating shaft, such that the rotor poles and shaft would form one continuous conductor. This design feature was added so that multiple machines could electrically share a common rotor by using conducting shaft couplers. This change was necessary because the stators now occupied the entire machine body's cross section, preventing positive and negative voltages from being applied to a single machine (which was possible with the one-pole machines). Only one voltage could be applied to each machine's stator plates, so two individual machines had to be connected via a common

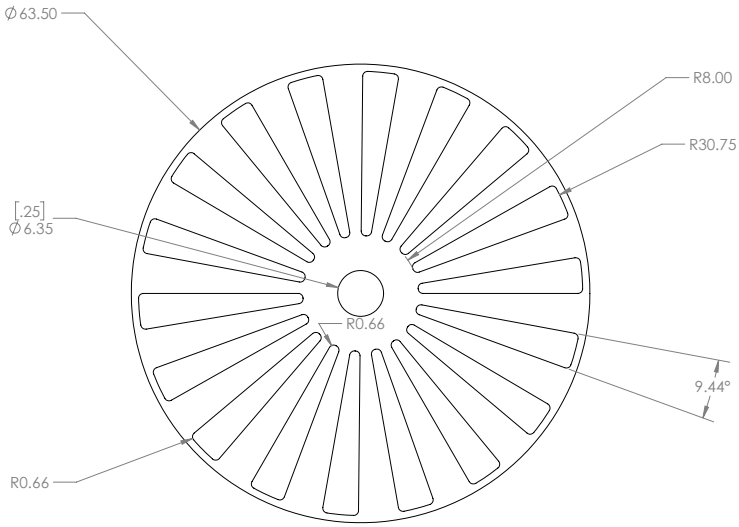

Figure 4.15: CAD drawing of optimized 18-pole rotor electrode

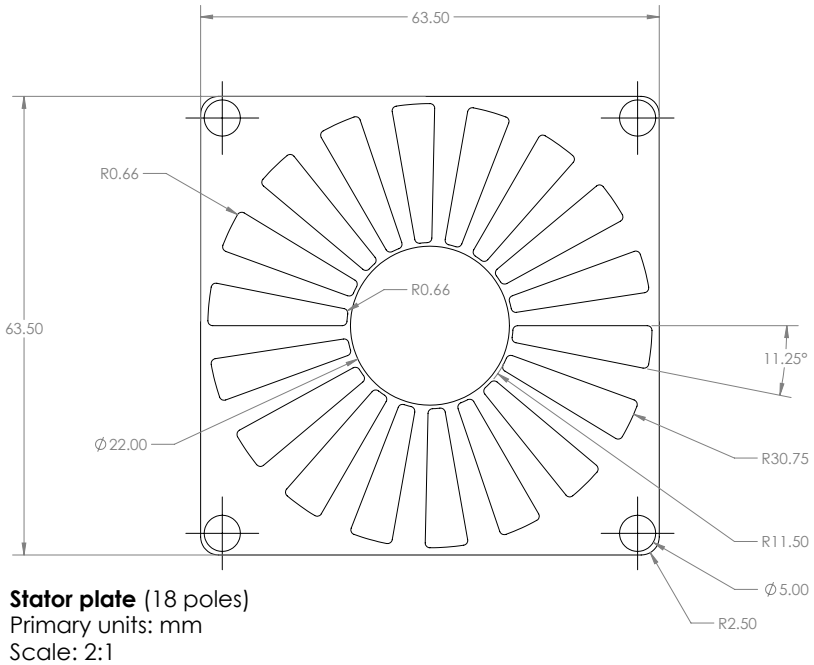

Figure 4.16: CAD drawing of optimized 18-pole stator electrode

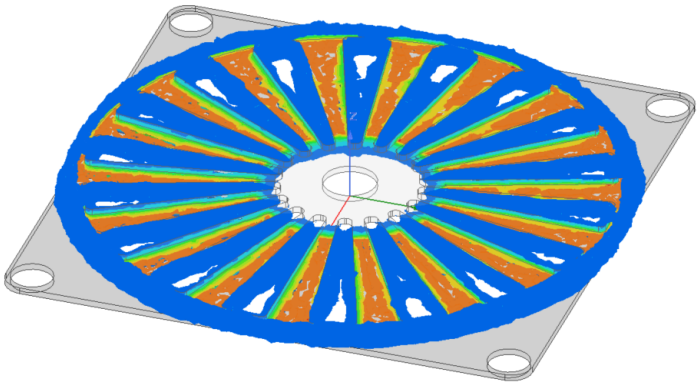

Figure 4.17: Electric field distribution within 18-pole rotor and stator plate pair, taken from FEA simulation

rotor, such that voltage could be applied to two separate stator groups. To mechanically connect each group of machines and electrically isolate them from other machines, Oldham style couplings with an insulating spider were used. By having symmetrical rotor and stator designs, counterweights were no longer needed to counteract any weight imbalances. Fig. 4.19 shows how these machines were configured.

The rotors were skewed to reduce ripple, as was done with the one-pole machines, but was significantly more challenging and less precise since the angular span to skew the rotors was scaled down by $\mathcal{P}$, meaning each rotor would have to be skewed by $\frac{360°/\mathcal{P}}{N} = 6.67°$. Even when the proper position was obtained, the rotors would move slightly as the shaft couplers were tightened. Filing a flat edge on the shaft end during manufacturing to correspond to either C_{max} or C_{min} would have helped with skewing the rotors.

Unlike the one-pole machines, the capacitance of the 18-pole machines varied somewhat from each other. Table 4.1 provides these capacitances, where measured values were obtained with the Keysight impedance analyzer E4990A. The capacitance calculated by FEA somewhat overestimated ΔC, since the measured value of C_{min} was over 50 pF larger than the FEA prediction. C_{max}, however, was within 8 pF of the measured value. The discrepancy in C_{min} can likely be attributed to certain elements not having been included in the FEA model, such as the shaft and bolts, which would have introduced stray capacitance.

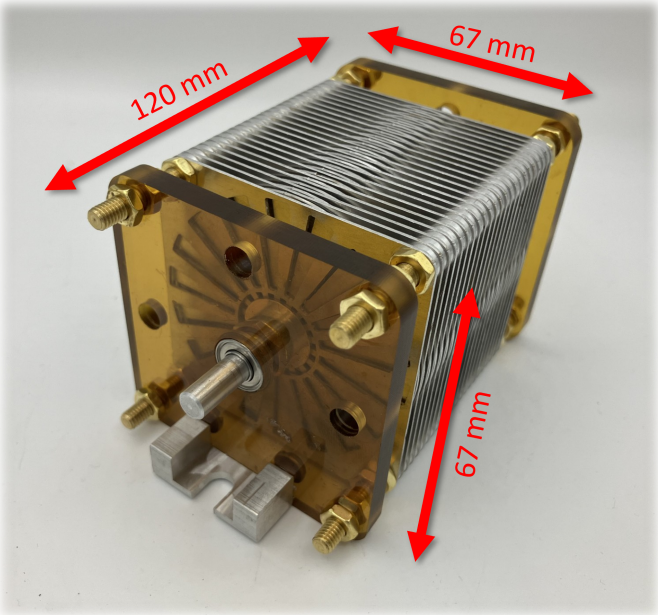

Figure 4.18: Prototype of 18-pole machine

Although the gap distance of the 18-pole machines was the same as the one-pole machines (0.5 mm), the 18-pole machines broke down at 2.2 kV, rather than at 3 kV. Upon close inspection of the electrodes, there were small burrs and other sharp edges that would lead to sparking at lower voltages.

4.3.3 Short-circuit testing

The same short-circuit testing procedure used for the one-pole machines was used for the 18-pole machines. From Fig. 4.20, it is clear that the measured values corresponded well with the expected values in the series configuration. In the parallel configuration, however, there was a large discrepancy between the two. The most likely explanation for this difference is the imprecision in the skewing of the rotors. Although the one-pole machines were also not perfectly skewed, the fundamental frequency of the one-pole machines was small enough to not influence the charging and discharging times of the load capacitors. For the 18-pole machines, however, any slight deviations from the proper skewing of the rotors would be magnified by the higher pole count of the machine, leading to current injections from each machine that were too fast for the load capacitors to absorb.

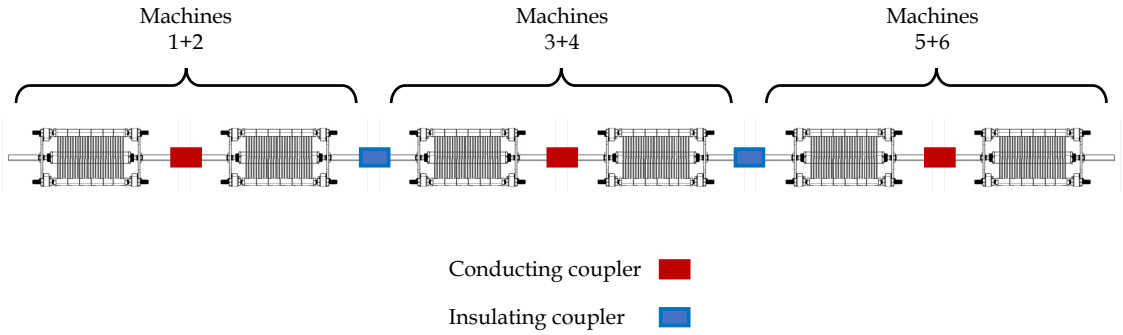

Figure 4.19: Configuration of shaft couplers with 18-pole machines

Machine No.	C_{max} (pF)	C_{min} (pF)	ΔC (pF)
1	1380	808	572
2	1400	809	591
3	1420	813	607
4	1400	813	587
5	1390	815	575
6	1400	816	584
Avg. of individuals	1398	812	586
FEA of individual	1406	758	648
1+2	696	407	289
3+4	702	411	291
5+6	698	411	287
Avg. of pairs	699	410	289

Table 4.1: Capacitance of 18-pole machines

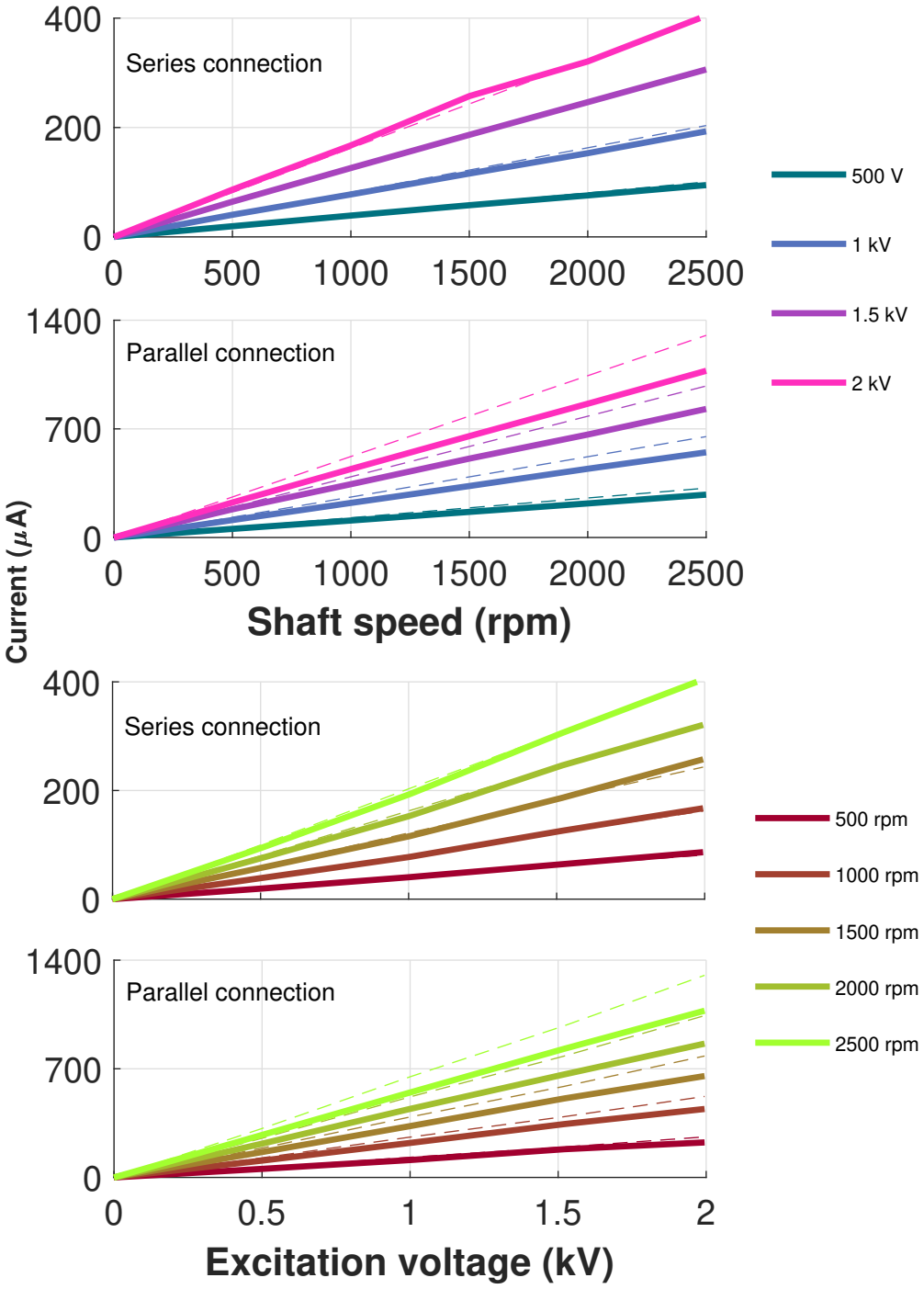

Figure 4.20: Short circuit currents for series and parallel connection of three 18-pole machines as a function of shaft speed (top two plots) and excitation voltage (bottom two plots). The solid line represents measured values, and the dashed line represents expected values.

4.3.4 Output power as a function of load, excitation, and number of cells

As was the case with the testing on the one-pole machines, the output power was measured as a function of R_L, V_E, and N and compared with the analytical expressions.

In the load sweep testing, a larger V_E could be used since C_{min} was small enough such that $\frac{V_{OC}}{V_E} < 1$. As a result, the tolerance around $V_E = 1000V$ was much tighter, at just $\pm 2.5\%$. With this tighter tolerance, the measured values were slightly under the expected values in both the series and the parallel configurations, albeit with the proper profile (see Fig. 4.21).

In the maximum power testing (see Fig. 4.22), the results obtained for the series and parallel configurations were nearly identical, being less than 10 mW apart at all operating points. The maximum power recorded, 0.255 W at $V_E = 1.9kV$ and $\omega_m = 2500$ rpm, is greater than the maximum power obtained with the one-pole machines (both in an absolute sense and as a power density – this will be explained in further detail in Section 4.4).

The output power also scaled linearly with the number of cells N, shown in Fig. 4.23.

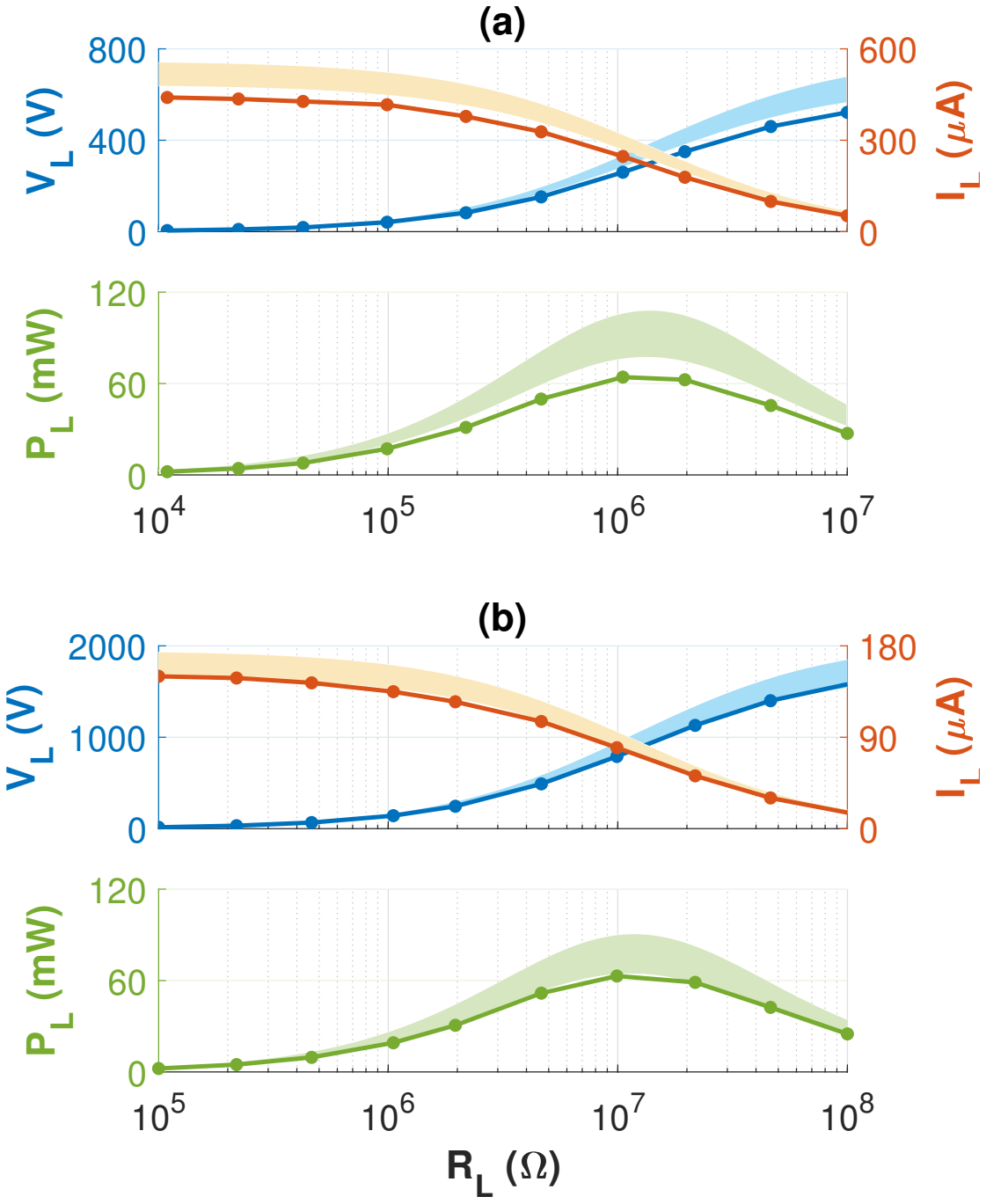

Figure 4.21: Load sweep of 18-pole machines at 2000 rpm (a) connected in series with $V_E = 1000 \pm 25V$, and (b) connected in parallel with $V_E = 1000 \pm 25V$. The tolerance in the expected values (shown in shaded region) takes into account the uncertainty with V_E ($\pm$ 2.5%) as well as C_{min} ($\pm$ 7 pF).

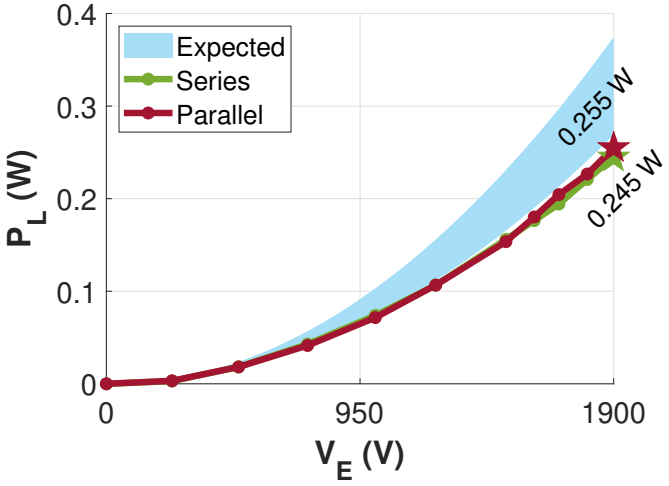

Figure 4.22: Maximum power testing of 18-pole machines, with P_L vs. V_E at 2500 rpm. The tolerance in the expected values takes into account the uncertainty with $V_E(\pm 2.5\%)$ as well as $C_{min}(\pm 7pF)$

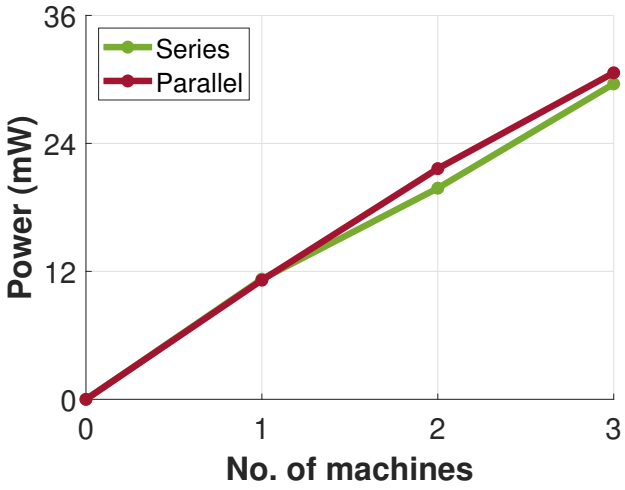

Figure 4.23: Scaling of system power by the number of machines, P_L vs. N, at 1000 rpm and V_E=1 kV

4.4 Comparison between one-pole and 18-pole machines

An important contribution of this work was to confirm that a varying capacitance machine's output power could be improved by optimizing the geometry of the electrodes. In Section 4.3.1, the machine that would yield the greatest $\frac{\Delta C}{\Delta \theta}$ having the same dimensions as the one-pole machines was found to have 18 poles. Using Eq. 3.16, the 18-pole machines would theoretically improve the output power by a factor of 3:

$$\frac{P_{L,18pole}}{P_{L,1pole}} = \frac{\frac{N}{4}{V_{max}}^2 \Delta C f_e \left(1 - \frac{C_{min}}{C_{max}}\right)}{\frac{N}{4}{V_{max}}^2 \Delta C f_e \left(1 - \frac{C_{min}}{C_{max}}\right)} = \frac{(2200V)^2(18)(271pF)\left(1 - \frac{410}{699}\right)}{(2800V)^2(470pF)\left(1 - \frac{30}{500}\right)} = 3.01 \quad (4.3)$$

By taking the maximum power recorded for each system (0.136 W for the five one-pole machines, and 0.255 W for the three 18-pole machines) and calculating the power density for each, the two systems can be assessed fairly. As shown in Table 4.2, the one-pole machines had a maximum power density of 26 W/m^3, and the 18-pole machines had 79 W/m^3, which corresponds to a 3.04x improvement.

It should be noted, however, that a machine may be optimized for other parameters as well. For example, although the 18-pole machine improved the output power, the output voltage was always lower than V_E because $\frac{\Delta C}{C_{min}} < 1$. If these machines are to be used for HVDC generation, it may be worthwhile to co-optimize for some desired output voltage. In addition, it was discussed in Section 3.4 that the optimal varying capacitance machine design also depends on whether active or passive electronics are used. For passive electronics, the machine should be optimized for both $\frac{\Delta C}{\Delta \theta}$ and $\frac{C_{min}}{C_{max}}$, whereas systems using active electronics only need to be optimized for $\frac{\Delta C}{\Delta \theta}$.

Metric	One-pole machines	18-pole machines
C_{max}	500 pF	699 pF
C_{min}	30 pF	410 pF
ΔC	470 pF	289 pF
V_{max}	2.8 kV	2.2 kV
g	0.5 mm	0.5 mm
N	5	3
Volume	5162 cm^3	3232 cm^3
Power density (at V_{max} and ω_m= 2500 rpm)	26 W/m^3	79 W/m^3

Table 4.2: Comparison of one-pole and 18-pole machines

Chapter 5

Considerations for Utility-scale Systems

The little voice inside never grows any older.

— Frank Pierret

This section describes some of the analytical shortcomings in the machine design presented by GE. Improved designs based on FEA are presented and compared with the original GE design. The FEA results highlight the difference in machine designs for those systems using active vs. passive electronics. A comparison of an offshore wind farm using direct-drive permanent magnet synchronous machines vs. varying capacitance machines is also presented.

5.1 Description of GE machine design

In [15], GE presents a paper design for a 7 MW vacuum-insulated varying capacitance machine operating at 200 kV. While the design does a good job of providing the reader with a rough idea of the dimensions and requirements needed to build a utility-scale system, there are several important design attributes omitted in the analysis.

First and foremost, the influence of C_{min} is completely ignored, both in the estimation of the machine's capacitance as well as in the calculation of the power delivered to the load.

For electrostatic machines with high pole counts (>30), leakage capacitance effects are significant when the stator and rotor plates are out of phase with each other, contributing to a non-zero C_{min} that reduces ΔC considerably. In addition, it was shown in Eq. 3.16 that $\frac{C_{min}}{C_{max}}$ has an appreciable influence on the power delivered to the load when passive electronics are used. However, this effect is completely ignored in [15], as it assumes that power can be delivered over the entire half cycle that the machine is generating.

Aside from these analytical shortcomings, the 2.22 mm-thick plates used in the design in [15] are impractical for a machine that is nearly 1 meter in diameter. Thicker plates would be needed to combat wobbling, vibrations, and for gap maintenance.

5.2 Improved machine designs

To demonstrate what a more realistic utility-scale system might look like, analysis was conducted using Ansys Maxwell FEA. All physical aspects of the machine except for the plate thickness were kept the same as the design in [15] in order to facilitate a fair comparison. The procedure was similar to the one used for the bench-scale machines and was conducted in the following manner:

- For each pole count, a rotor and stator pair with 4-mm thick electrodes separated by a 4-mm air gap were drawn in Ansys Maxwell. The angular width of the pole θ_{pole} (also known as span) was parametrized, such that a range of values could be assigned to it.

- θ_{span} was swept from one-tenth of its maximum value to its maximum value, and the capacitance was calculated at each pole span. This sweep was run when the rotor and stator poles were in phase with one another (to determine C_{max}) and when they were out of phase with one another (to determine C_{min}).

- The raw C_{min} and C_{max} data was then processed in MATLAB. For machines using active electronics, the θ_{span} that yielded the greatest $\frac{\Delta C}{\Delta \theta}$ was determined for that specific pole count. For machines using passive electronics, both $\frac{\Delta C}{\Delta \theta}$ and $\frac{C_{min}}{C_{max}}$ had

to be considered in finding the optimal θ_{span} for that pole count.

- This process was repeated for all pole counts considered, which spanned from 2 to 180 poles.

The FEA analysis results are plotted in Fig. 5.1, where the calculation of P_L (on the y-axis) assumes the same input parameters as the ones used in [15]: $\omega_m = 9600\ rpm$ and $V_{max} = 200\ kV$. The optimal machine parameters for each system using passive and active electronics are shown in Table 5.1 alongside the design parameters used in [15]. For a system using passive electronics, a machine with 75 poles is optimal, and for active electronics, 125 poles is optimal (see Fig. 5.2-5.3 for 3D renders of these machines' rotors).

Not only is it clear that the design in [15] vastly overestimated P_L – even if active electronics had been used – but the difference in the passive vs. active electronics-based machine designs is evident. For the machine using passive electronics, it is desirable to have a lower pole count with a smaller ratio of $\frac{C_{max}}{C_{min}}$ compared with the machine using active electronics. This observation is supported by the $\left(1 - \frac{C_{min}}{C_{max}}\right)$ factor in Eq. 3.16, since a greater $\frac{C_{min}}{C_{max}}$ reduces P_L in passive electronics-based systems but does not play a role in active electronics-based systems. The nearly 6x difference in P_L between the two also highlights the inherent trade-off with each system: while using passive electronics is simple and cost-effective, it vastly underutilizes the available power in the machine. On the other hand, designing a high-voltage rectifier based on active electronics adds complexity to the system.

While this paper focused on using varying capacitance machines (also known as elastance machines), the HVDC concept based on cascaded bridge converters could be applied to other synchronous electrostatic machinery, such as separately excited machines. Doing so could utilize an even greater portion of the available machine power, since the voltage on the stator and rotor are controlled, meaning that the machine can generate over its entire cycle.

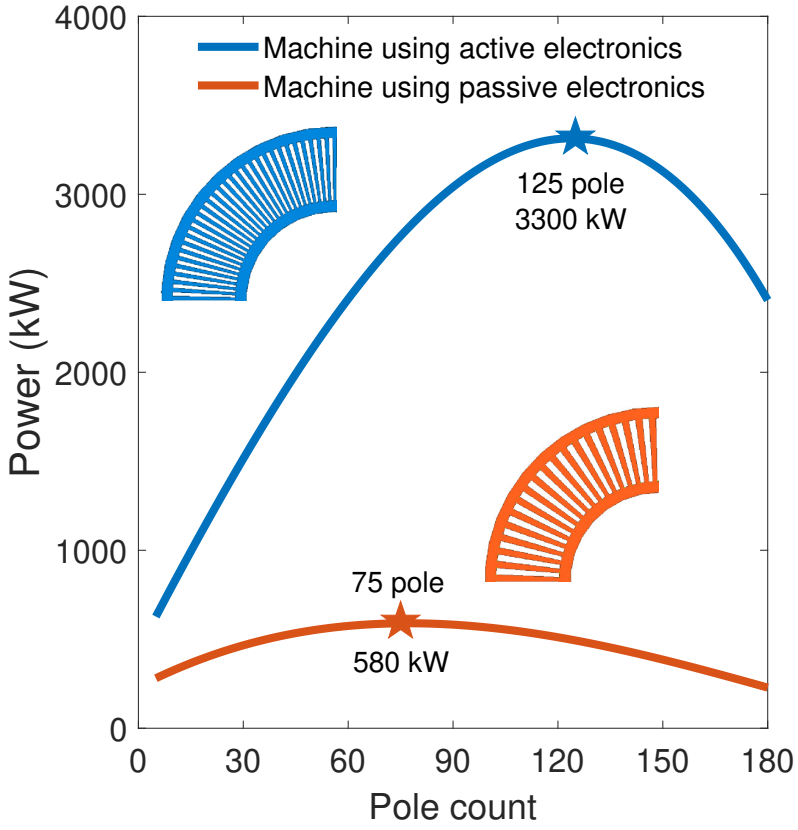

Figure 5.1: Power delivered to load vs. pole count for varying capacitance machines using active and passive electronics at $\omega_m = 9600rpm$ and $V_{max} = 200kV$. The optimal machine at each pole count was determined using FEA, and a section of the optimal machines' rotor plate is shown.

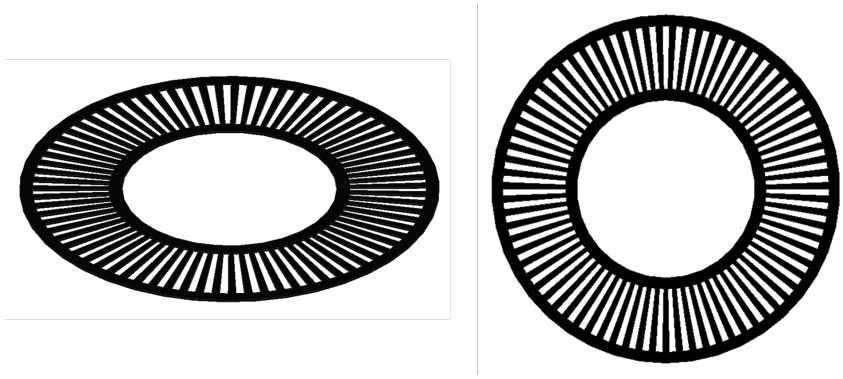

Figure 5.2: 3D rendering of 75-pole machine

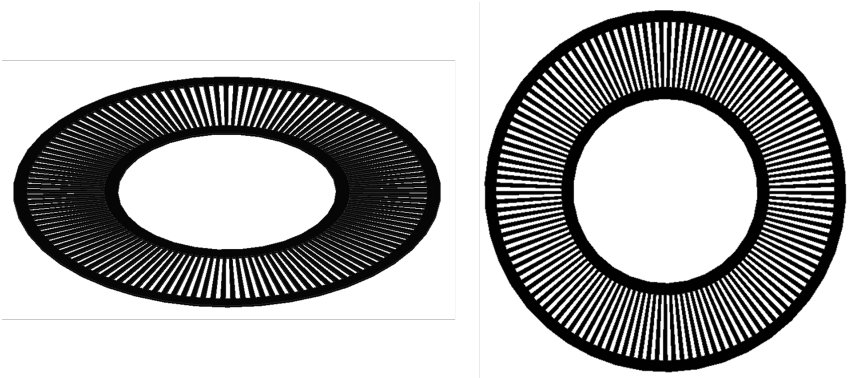

Figure 5.3: 3D rendering of 125-pole machine

Table 5.1: Original machine design presented in [15] and optimized redesigns using FEA. See Fig. 3.2 for labeled machine section.

Parameter	Machine in [15]	Machine with passive electronics	Machine with active electronics
r_{out}	47 cm	47 cm	47 cm
r_{in}	24 cm	24 cm	24 cm
g	4 mm	4 mm	4 mm
L_{body}	2 m	2 m	2 m
t_{elec}	2.22 mm	4 mm	4 mm
No. of plates	320	250	250
Pole count	100	75	125
θ_{pole}	Unspecified	1.44°	0.432°
Pole duty span	Unspecified	60%	30%
C_{max}	568 pF	456 pF	440 pF
C_{min}	0	368 pF	368 pF
ΔC	568 pF	88 pF	72 pF
ω_m	9600 rpm	9600 rpm	9600 rpm
E	25 kV/mm	25 kV/mm	25 kV/mm
V_{max}	200 kV	200 kV	200 kV
P_L	7300 kW	580 kW	3300 kW

5.3 Considerations for offshore wind farms

To help contextualize the benefits of varying capacitance machinery, a comparison was conducted between a wind farm consisting of direct-drive PM synchronous machines and that same farm using the 125-pole machine design described in Section 5.2. Specifically, the 400-MW Merkur Windpark consisting of 66 6-MW GE Haliade 150-6 wind turbines (see Chapter 1) is used as the reference point. Table 5.2 summarizes the findings of this comparison.

Based on information in [40], the volumetric power density and the mass power density of the PM machines used in the Merkur Windpark are approximately 150 W/L and 124 W/kg, respectively. These metrics place each machine at roughly 400 m^3 and 48 tonnes. With these machines being direct drive, there is no need for a gearbox. However, each turbine contains a MV transformer at its base, each weighing roughly 11.3 tonnes and occupying 14.3 m^3 [41]. The Merkur Windpark also consists of an offshore substation (OSS) housing HV transformers and a separate converter station housing the VSC. The OSS weighs approximately 4200 tonnes and occupies 1520 m^3 [42], and the VSC weighs approximately 20,300 tonnes and occupies 2830 m^3 [43]. If just the "active" mass and volume are considered, where active refers to components that are actively facilitating power conversion, then the active mass of the wind farm is 28,400 tonnes and the active volume is 31,700 m^3. Accordingly, the volumetric and mass power densities of the active area of the 400-MW wind farm correspond to 14 W/kg and 12.6 W/L, respectively.

If the FEA model of the 125-pole machine using active electronics in Section 5.2 is operated at 1500 rpm (a typical rotational speed for wind turbines with a gearbox) rather than at 9600 rpm, its average output power becomes 520 kW at a volumetric power density of 360 W/L. To match the 6-MW power rating of the machines used in the Merkur Windpark, 1442 rotor and 1443 stator plates would be needed over a volume of 166 m^3. If steel with a mass density ρ of 7.85 g/cm^3 is used for the stator and rotor plates, the

mass per plate is equal to

$$W_{plate} = \pi(r_{out} - r_{in})^2 t_{elec}\, \theta_{duty}\, \rho_{steel} = 1.57\, kg/plate. \tag{5.1}$$

Similarly, the mass of a steel shaft segment (where segment refers to the width of the airgap and an individual plate) for each plate can be estimated:

$$W_{shaft} = \pi {r_{in}}^2 (g + t_{elec})\, \rho_{steel} = 11.36\, kg/segment. \tag{5.2}$$

Based on commercially-available gearboxes rated up to 7 MW, the gearbox for this machine would weigh roughly 40 tonnes and occupy 10 m^3 [44]. To provide the vacuum insulation, a roughing and scrolling pump would be needed in each turbine but would collectively weigh no more than 1 tonne and occupy no greater than 1 m^3 [45]. Because the varying capacitance machine is able to directly produce HVDC, the OSS and VSC are not necessary, eliminating a significant mass and volume from the system. If the gearbox and vacuum pumps are included in the definition of "active" area, then the active mass of the system is 5200 tonnes, and the active volume is 11,700 m^3. These metrics place the active mass power density and active volumetric power density at 77 W/kg and 34.2 W/L, respectively. Relative to the system with the PM machines, the varying capacitance machine-based system has 5.5x better utilization of active mass and a 2.7x better utilization of active volume.

Table 5.2: Comparison of 400-MW Merkur Windpark using GE Haliade 150-6 direct-drive PM machines vs. 125-pole active electronics-based varying capacitance machines with a gearbox

	Direct-drive PM machines	Varying capacitance machines with gearbox
No. of wind turbines	66	66
Machine rated power	6 MW	6 MW
Machine mass power density	124 W/kg	160 W/kg
Machine volumetric power density	150 W/L	360 W/L
Machine mass	48 t	37.3 t
Machine volume	400 m^3	166 m^3
Gearbox mass	0	40 t
Gearbox volume	0	10 m^3
Vacuum pump mass	0	1 t
Vacuum pump volume	0	1 m^3
MV Transformer mass	11.3 t	0
MV Transformer volume	14.3 m^3	0
OSS mass	4200 t	0
OSS volume	1520 m^3	0
VSC mass	20,300 t	0
VSC volume	2830 m^3	0
Active mass of wind farm	28,400 t	5200 t
Mass power density of active area	14.1 W/kg	77.0 W/kg
Active volume	31,700 m^3	11,700 m^3
Volumetric power density of active area	12.6 W/L	34.2 W/L

Chapter 6

Conclusions

I would rather have questions that can't be answered than answers that can't be questioned.

— Richard Feynman

6.1 Contributions

This work's contributions broadly fall into two categories: one related to the architecture for realizing HVDC grids with rotating varying capacitance machines, and the other related to linear direct-drive machines for wave energy (described in the Appendix).

6.1.1 Architecture for HVDC grids based on rotating varying capacitance machinery

- An architecture for generating and transmitting HVDC without step-up transformers was proposed. Building off of and improving upon a concept outlined by General Electric in 1977, this architecture utilizes a cascaded bridge converter with varying capacitance machines.
- An averaged model of the proposed architecture with half-wave diode bridge rectifiers was derived, allowing the system to be represented as a network of "cells" consisting

of equivalent current sources feeding into a load. This simplified model provides transparency on the system's behavior from a terminal perspective.

- Using the averaged model, the load and excitation conditions to maximize the power delivered to a load were derived. Conditions were derived in two different situations: one where there is no constraint imposed on the maximum voltage that the machines can insulate, and one where the machines' maximum voltage is constrained.

- The averaged model was verified at the bench scale using machine prototypes. The experiments included short-circuit testing, load sweeping, power vs. excitation testing, and power vs. number of cells testing. Each experiment was conducted for the cells being configured in series and in parallel.

- The geometry of the rotor and stator plates was optimized using FEA, and prototype machines with these optimized designs were constructed and tested. The power density of the optimized design was 3x larger than the original design, matching the predicted improvement and demonstrating the opportunities with electrostatic machine design optimization.

- A detailed FEA simulation was used to create a varying capacitance machine design for utility-scale power generation. The results also highlighted the impact of using passive vs. active electronics in the optimal machine design.

6.1.2 Linear direct-drive machines utilizing liquid for wave energy

- The effect of charge leakage on the performance of varying capacitance machines was studied using an instantaneous model. Criteria regarding the material properties of the dielectric were derived.

- Five different linear direct-drive varying capacitance machines were prototyped and evaluated experimentally. Each design utilized a liquid in the design of the capacitor to simplify the mechanics of the electromechanical energy conversion process.

- The materials criteria were empirically supported with experiments using dielectric liquid-filled varying capacitance machine prototypes. Two different dielectric liquids with differing material properties were tested. Ultimately, it was determined that the $\frac{\epsilon}{\sigma}$ of commercially-available dielectric liquids is too large to make direct-drive WECs viable.

- A review of electrostatic wave energy converters was conducted and published in [21].

6.2 Recommended Future Work

While this work presents a foundation for realizing HVDC grids with electrostatic machinery, there are several other aspects that should be investigated for its continued development:

- The scaling of the proposed system to utility power levels rests upon its operation in vacuum. As a next step in that direction, it would be necessary to design and operate a 10 to 100-kW machine with medium voltage electronics in a vacuum chamber.

- The architecture presented in this work is compatible with any type of synchronous electrostatic machine, including the separately-excited synchronous electrostatic machine (SEM). Using SEMs instead of varying capacitance machines may offer several benefits, including a greater power density and more controllability.

- To facilitate active rectification, a DC-to-DC converter (e.g., boost, buck, or buck-boost converter) could be connected to the output of the rectifier. Using the DC-to-DC converter could help with regulating the bus voltage and improving the output power of varying capacitance machines.

- Designing a control strategy for the architecture was beyond the scope of this work but would be necessary for grid interconnection. For example, droop control could be implemented, where the generator speed and excitation are adjusted based on the bus voltage.

Chapter 7

Chapter for the Public

> *Truth is ever to be found in the simplicity, and not in the multiplicity and confusion of things.*
>
> — Isaac Newton

I am including this chapter in my dissertation to communicate my research to the general public. In my opinion, making research comprehensible for people of all backgrounds is just as important as mastering the technical intricacies of any field. I would like to thank the Wisconsin Initiative for Science Literacy (WISL), including Bassam Shakhashiri, Cayce Osborne, and Elizabeth Reynolds, for providing this opportunity to communicate my work to a broader audience.

7.1 Harnessing energy from the oceans

If you've ever been on a road trip through rural areas (especially in the Midwest), you've probably seen wind turbines dotting the landscape with their white towers and sleek blades. For the past 20 years, not only have we been harnessing the power of the wind on land, but we have also been tapping into wind energy from the oceans, known as "offshore wind". In addition to being out of sight from the public eye, offshore wind turbines can generate more power than land-based turbines, since the winds are typically stronger and more consistent over the open ocean. Scientists are also working to harness other sources

of energy from the oceans, including from tides, waves, and currents. While all of these sources of ocean energy are plentiful and promising for the clean energy transition, sending the electricity from the ocean to where it will be used onshore is a huge barrier to utilizing ocean energy. As such, my research is focused on developing new technologies that make it simpler and cheaper to transmit electricity for ocean energy systems.

7.2 Basics of ocean energy systems

The raw energy of the oceans is astounding. While it is difficult to pinpoint an exact number on just how much energy there is, scientists agree that ocean-derived energy could satisfy the global demand for electricity.

One of the most attractive aspects of ocean energy is its proximity to population centers. Nearly 75% of the world's population lives within 50 km of the ocean, meaning that electricity could be generated right where it is needed. Utilizing ocean energy could avoid costly upgrades to the power grid that are often necessary for integrating other sources of energy, such as solar and wind. These upgrades are not trivial, as solar and wind farms tend to be located in remote areas, necessitating extensive networks of new power lines and other grid infrastructure to be built.

Another key advantage of ocean energy is its predictability and 24-hr. availability. Because solar and wind energy are not constant, batteries and other energy storage technologies are necessary for integrating higher levels of these resources into the electric grid. In contrast, energy sources within the oceans (such as waves, tides, and currents) are not random processes and can be relied upon for consistent energy delivery.

Despite these advantages, however, harnessing ocean energy is significantly more challenging than solar or onshore wind energy. To understand why, I will provide a little background on how electricity is generated and transmitted and how it is different for ocean energy systems.

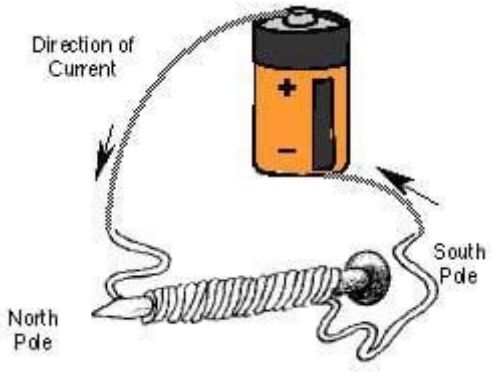

Figure 7.1: Example of an electromagnet, formed by wrapping a wire around a nail and connecting a battery to the ends of the wire. The current from the battery creates a magnetic field that allows the nail to pick up paperclips and other ferrous (iron-containing) objects.

7.2.1 Generation

Generating electricity always begins with the resource(s) supplying the raw energy, which in the case of ocean energy originates from the tides, waves, winds, or currents. From here, this raw energy must somehow be captured by a device before it can be converted into electricity. For the case of wind energy, turbine blades are the most effective way to capture the raw wind energy. For the other forms of ocean energy, scientists are still trying to figure out the best way to capture the raw energy. Many unique (and sometimes quirky) systems have been proposed, including buoys, flexible membranes, and even sea snakes! Designing these systems is typically the work of mechanical engineers, civil engineers, and naval engineers, and was not the focus of my PhD.

Regardless of how the raw energy is captured, it eventually has to find its way to an electric generator. Nearly all electricity around the world is generated in the same fundamental way (solar energy is the key exception): Kinetic energy (or energy of motion) from some raw energy source is used to spin a magnet within a coil of wire. These magnets can either be permanent magnets (think of the ones on your fridge or a bar magnet) or electromagnets (caused by running current through a coil of wire, see Fig. 7.1 for a common example).

In offshore wind, permanent magnets are the preferred choice because they offer a

higher power density than electromagnets, allowing more energy to be converted into electricity. However, these gains in power density come at a price. The permanent magnets used in wind turbines (and other high-performance applications) require several rare-earth materials (such as Neodymium and Dysprosium) and advanced refining techniques. Mining these raw minerals incurs serious ecological damage to the surrounding area and is often done with forced labor and other unethical labor practices. Furthermore, only a small percentage of these magnets are mined and refined in the US, with the vast majority being sold by Chinese companies, adding to geopolitical tensions between the two countries.

In any case, the electricity generated by the interaction of these magnetic fields is not ready to be transmitted to the electric grid because a fundamental law of physics says the electricity will be at a low voltage. This fundamental law – Faraday's Law – basically says that spinning the magnet within the coil of wire produces a voltage that is proportional to two things: how fast the magnet is spun and the strength of the magnet. You can imagine that the rotational speed has a physical limit—even if we could make turbines spin faster, doing so increases the risk of damaging components from vibrations and mechanical failures. Magnet strength is also limited because magnetic materials saturate, just like how there is a limit to how much water a sponge can hold. Taken together, the physical limitations on rotational speed and magnet strength ensure that the voltage produced by electric generators is low. But why does this matter for electricity transmission?

7.2.2 Transmission

Back in the 1800s, people figured out that the most economically viable way to transmit electricity was to use high voltages. The reason for this is that raising the voltage lowered the current of the electricity that you needed to send to have the same amount of power (since Power = Voltage x Current), and lowering the current meant reducing power losses (since Losses = Current^2 x Resistance of Wire). Think of current as the flow rate of water in a pipe, voltage as the water pressure, and the wires through which the current is conducted as the pipe. Inside of the pipe, there is some amount of roughness (corresponding to resistance) causing friction with water that ultimately creates heat and wastes energy.

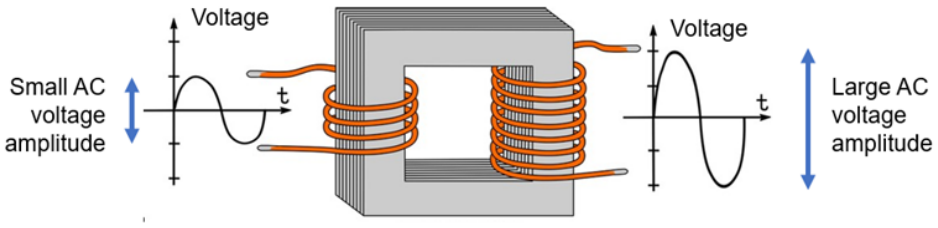

Figure 7.2: Cartoon of what transformers look like

If there is more water flowing through the pipe, there will be more energy wasted.

So, if the generators produce low-voltage electricity and high voltages are needed for transmission, how do we make the electricity high voltage? This question plagued scientists for years until the invention of the transformer in the late 1800s (yes, the same transformer on a utility pole in your neighborhood). Scientists figured out that low voltages could be stepped up to higher voltages if the electricity from the generator was run through a coil of wire with a low number of "turns" that was adjacent to another coil of wire with a high number of "turns" (see Fig. 7.2). The new voltage would be scaled by the ratio of the turns of each coil and worked best if the coils shared a common ferrous material (such as iron), since the coupling between the two coils relies on the magnetic field produced by the electricity in each coil. In fact, it is the advent of transformers that was the nail in the coffin for Thomas Edison's vision to use direct current (DC) in the power grid. When the electrons all move in one direction (DC), transformers cannot be used because the only way to create the magnetic fields that couple the two coils in the transformer is to force the electrons to wiggle (hence, alternating currents or AC). Thus, George Westinghouse (and Nikola Tesla) emerged as the clear victors in the so-called "War of the Currents" with the AC grid, since they could unlock high voltages with transformers. There's a pretty good movie with Benedict Cumberbatch portraying Thomas Edison in "The Current War" if you want a more dramatized and less technical version of this history.

The same efficiency advantages with high voltages hold true for transmitting electricity from ocean energy systems to land but with an important caveat: DC is actually better than AC! While this may seem counterintuitive since AC is used for transmitting power on

Figure 7.3: Analogy of water flowing through a pipe with "pockets" to explain charging currents in cable-based transmission, from [46]

land, a crucial difference between onshore and offshore power transmission is the medium through which the electricity is transmitted. On land, we primarily use bare overhead wires. In the ocean (and underground), we use cables. This difference may seem subtle and negligible but is actually quite significant. Because cables are essentially wires wrapped in layers of plastic and other insulating materials, some of the electric charges that would otherwise travel straight through a bare wire are trapped by the insulating layers of the cable. This phenomenon is known as "charging current" and is due to capacitive coupling within the cable. A simple way to understand this is to think of a hose with little pockets (see Fig. 7.3). In order for water to travel from one end to the other, these little pockets must first be filled with water. If these pockets must only be filled once (aka DC), it is not a big deal, but if they must be filled and emptied over and over again (aka AC), this becomes problematic. This effect is especially acute as the length of the hose increases. As a result, high voltage DC is the preferred technology choice in offshore energy systems, and AC is only feasible if the underwater transmission distance is short (usually 50 km or less).

So how do we go from AC to DC? In Thomas Edison's time, converting the generator's AC to DC for transmission was not technically feasible because semiconductors were not yet invented. Once semiconductor devices like diodes and transistors (like what you have in computers) became available in the 1950s, a new industry known as power electronics emerged. In addition to making AC to DC converters for renewable energy systems, the power electronics industry makes converters for laptop chargers, electric vehicles, and many other everyday systems. While laptop chargers fit in the palm of your hand and can be purchased for $20 on Amazon, the AC to DC converters (known as "rectifiers") used in offshore wind are around the size of an aircraft carrier and cost more than a billion

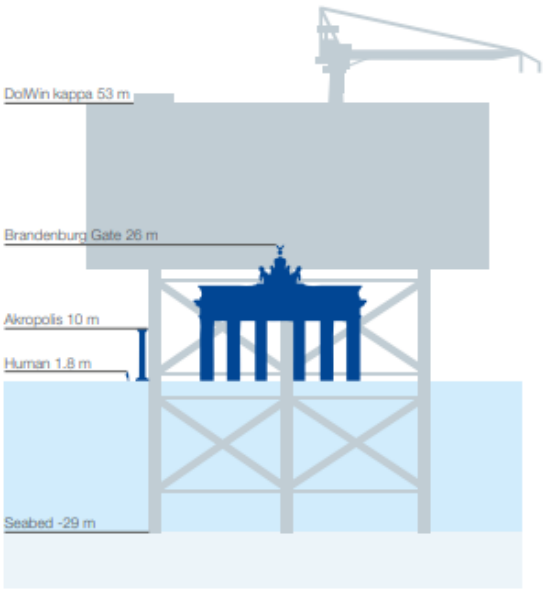

Figure 7.4: Illustration of just how large offshore converter stations are in offshore wind farms, from [43]. For those of you from Madison, the height of this structure from the sea floor to the top is almost as tall as the State Capitol from the ground to the top of Lady Wisconsin (86 m)!

dollars (see Fig. 7.4). These astronomical figures stem not only from the sheer amount of hardware needed to facilitate the AC to DC conversion but having to install everything in the open ocean makes the task significantly more challenging.

7.2.3 Layout of offshore wind systems

Now that you know how electricity is generated and transmitted, you can understand why offshore wind farms look the way they do. Fig. 7.5 shows an example of an offshore wind farm using high voltage DC transmission (HVDC), but I should mention that this layout would also apply to any other ocean energy system. Going from left to right, once electricity is generated by the turbines, it is stepped up to a higher voltage at the transformer station. While these transformer stations are not quite as large as the converter station platforms, they are still large, costly, and a pain point for offshore wind developers. From here, the electricity is converted to DC with the gargantuan converter station and sent onshore with DC cables. Finally, the converter station on land converts the electricity

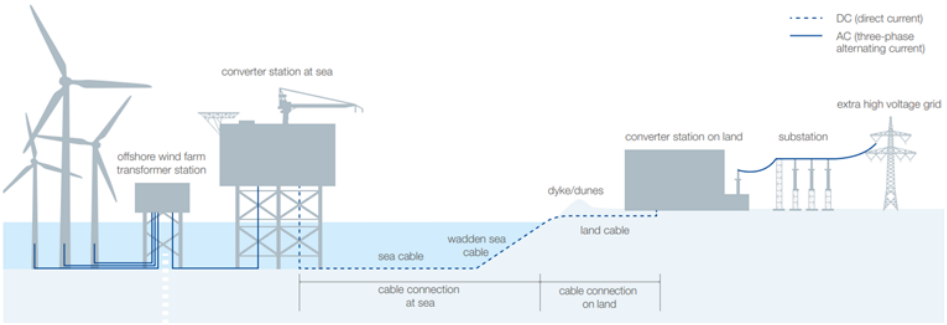

Figure 7.5: Layout of the DolWin offshore wind farm in the North Sea using HVDC transmission, from [43].

back to AC and sends it to the main grid (which uses AC).

Finding ways to simplify and reduce the infrastructure needed to connect offshore wind farms and future sources of ocean energy to the grid will allow more of these carbon-free resources to provide our electricity needs and serves as the basis of my research.

7.3 My research

Before I get into the details of my research, I'd like to start this section by mentioning that the path to my dissertation topic took many twists and turns. Research is often portrayed as a neat and tidy process where someone starts with an idea, works on it for a while, and eventually makes it work with some sweat and ingenuity, but this has not been my experience. Instead, my PhD research journey has been a reflection of my ups and downs in the lab, my own curiosity getting the better of me, and my advisor's seemingly inexhaustible supply of new (and sometimes crazy) ideas.

7.3.1 My research journey

I began my PhD with experience in power transmission engineering and an interest in all things related to the power grid and renewable energy but had very little background on the core areas of my advisor's research. My advisor is primarily interested in improving electric motors and renewable energy systems by applying electrostatics to these areas, rather

than being confined to the conventional magnetic systems I described earlier. Although electrostatics is just the technical term for "static electricity" – just like when you shock yourself from touching a doorknob after rubbing your feet on the carpet – I came to learn that there is a lot more to it than that.

It turns out that there are two ways to convert kinetic energy into electricity: with magnetics and electrostatics. In the previous section, I described how spinning a magnet inside of a coil of wire produces voltages, which we call "magnetic systems" in our discipline. Another way to create electricity is to simply use kinetic energy to move electrically charged objects (such as capacitors) relative to one another. As these charged objects move, the charge distribution within the objects feels pushing and pulling from the other object's charges, creating currents. Historically, these "electrostatic systems" have not played a major role in generating electricity because magnetic systems have satisfied our electricity needs for the past 150 years. However, as we look to expand into new domains, such as ocean energy, we may need to break from tradition and embrace electrostatic systems.

Why should we look at electrostatic systems? I came to learn that they have three key benefits over magnet systems:

1. Electrostatic systems have much lower materials requirements than magnetic systems. They do not require any rare earth materials and are primarily constructed from lightweight and abundant materials, such as plastics and aluminum. An easy way to internalize this is to think about what it takes to make magnetic forces vs. electric forces with household items: For magnetic forces, you either need a permanent magnet (could be fridge or bar magnet) or an electromagnet, like the one I showed previously in Fig. 7.1. For electric forces, you can just rub a balloon on the carpet and start attracting things like hair and pieces of paper.

2. Electrostatic systems are naturally high voltage and low current, while magnetic systems are naturally low voltage and high current. In Section 7.2.1, I discussed how the limitations in rotational speed and magnet strength ensure that the voltage

produced by magnetic systems is low. So, in order to attain higher power levels, high currents are desired, since power equals the product of current and voltage. Similarly, the rotational speed and electric field strength in electrostatic systems are limited, so the current they create will be limited, and thus high voltages are desired to boost power. One important ramification of electrostatic systems' tendency to be high voltage is that they could produce electricity that is ready for transmission without all of the infrastructure that is normally needed in magnetic systems (such as transformers).

3. Electrostatic systems tend to be more efficient at low-speed operation than magnetic systems. The reason for this is a bit nuanced but simple in principle. I mentioned in Section 7.2.2 that power losses depend on the amount of current flow, just like how more water flowing through a rough pipe will waste more energy. In magnetic systems, a large amount of current must flow and as the rotational speed decreases, a greater share of this current flow is generating heat and losses, rather than being used to generate electricity. Conversely, electrostatic systems do not rely on a large current flow to generate electricity, so even as the speed decreases, they will have negligible power losses—or so we thought (more on that later).

Bearing these advantages in mind, we thought that wave energy would be the perfect application of electrostatics because waves move incredibly slowly and previous efforts using conventional magnetic systems were largely unsuccessful due to these systems being so inefficient. On top of that, most wave energy systems reported in the literature required copious amounts of rare earth materials and were very heavy (one such system weighed 6,700 tons and only had the power capacity of a single wind turbine, which weighs less than 200 tons!!). In what turned into the first two years of my PhD, I learned that even electrostatic systems were no match for the waves, as the systems I prototyped and tested in the lab either did not work at all, led to unexpected and useless outcomes, or were less efficient and less power dense than other scientists' magnetic systems. I won't go into detail here since I want to focus on my later work, but you can read more and see pictures

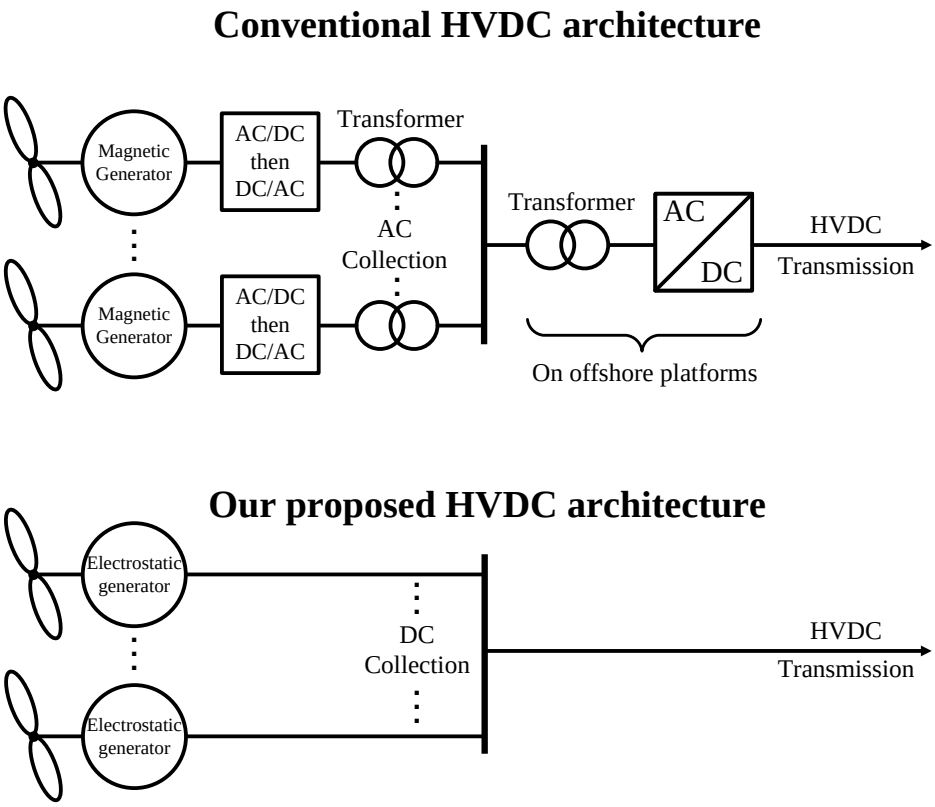

Figure 7.6: Comparison of conventional HVDC system architectures that use magnetic generators vs. our proposed HVDC architecture using electrostatic generators

of my contraptions in the Appendix.

7.3.2 My dissertation experiments

Since we did not have much luck with exploiting the efficiency of electrostatic systems at low speeds, we decided to instead explore the idea of generating electricity that was "ready" for transmission (advantage #2 that I listed above). More specifically, we wanted to develop an electrostatics-based architecture for renewable energy systems that requires HVDC transmission, which encompasses anything offshore. As I mentioned in the first few Sections, current HVDC transmission technologies are complex and costly, posing a significant hurdle to utilizing offshore energy resources. Our aim was to simplify the hardware requirements for HVDC transmission by using electrostatic generators to produce the electricity, see Fig. 7.6.

There was some existing research that helped guide us towards solutions with a greater chance of success, but we were otherwise proposing things that had never been tested before. The basic idea behind our approach was as follows:

- Use wind turbines, tidal turbines, wave buoys, or any other source of raw ocean energy to drive several electrostatic generators connected to each other with a common shaft. Each generator would operate at a high voltage and would be constructed exclusively out of aluminum and plastic.

- Use the simplest of semiconductor devices (diodes) to convert each individual generator's AC output to DC.

- Combine all of the generator's outputs so that the output voltage of the whole system equals the sum of each individual generator's output voltage. The goal is to have the output voltage of the whole system be large enough for HVDC transmission (100,000 volts or more).

To see if our proposal would work, we had to first describe it mathematically (which resulted in many hours spent deriving equations, see Chapter 3) and then run experiments on a small-scale system to see if our results matched our mathematical model. If the experimental results matched what the math predicted, we could then extrapolate our results to larger systems with confidence.

Although Chapter 4 already describes all of the experiments in detail, I want to include an abbreviated version to highlight some important things. We first contacted a local prototyping company to build us custom prototypes of our generators. Once we received the prototypes, we connected a servo motor to one of the generator's shafts and connected the shafts of each generator to each other. The servo motor simulated the raw energy that would drive our generators. I also had to construct a subsystem for providing high voltages to the generators. I won't go into the details on this (you can see pictures of it in Chapter 4), but it was able to take the 120 volts AC from the wall outlet and bring it up to 5000 volts DC for each generator! Because the generators would be spinning quickly

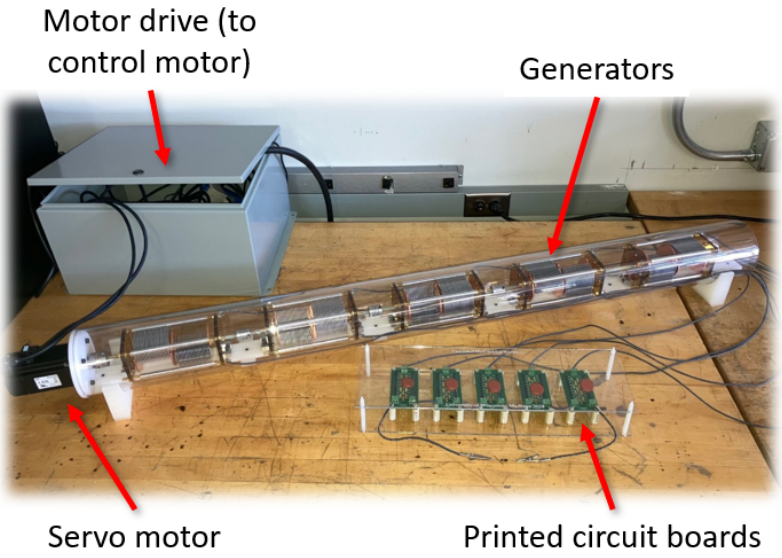

Figure 7.7: Picture of my experimental setup. On the far left is the servo motor that drives each generator contained within the plastic tube. The green printed circuit boards are the AC to DC converters, and there are five in total, since we had five generators.

and would be at a high voltage, we put them inside of a protective plastic tube. Because it was also see-through, it had the added benefit of looking cool (see Fig. 7.7). Finally, I had to build printed circuit boards (the green things in Fig. 7.7 — these are like computer chips and are found in almost every household electronic device) to house all of the diodes and other electronics that would facilitate the AC to DC transmission for each generator's output.

After running several experiments where I changed different input parameters and recorded their effect on the outputs, we concluded that our mathematical model was representative of the true physical system we tested. In light of the unsuccessful experience we had with our wave energy systems, this was a huge relief.

The next logical step was to see how we could improve our system, which meant finding ways to increase the power density. The low-hanging fruit solution was to optimize the geometry of the generator, since we knew that the original prototype was not optimal. I used a computer simulation tool to determine what the output power for different designs would look like. In order to facilitate as fair of a comparison as possible, I kept all of

the physical dimensions (height, width, thickness, etc.) of the new design equal to the previous prototype's. You can see a comparison of the two designs in Fig. 4.5 and Fig. 4.18.

Over the course of six months, which spanned the initial design process of the new generators to repeating the same experiments I did with the previous generators, we were able to triple the power density with our new design! The previous power density was 26 Watts per cubic meter, and the new power density was 79 Watts per cubic meter. To put these numbers in perspective, the magnetic-based generators used in offshore wind turbines typically have a power density greater than 100,000 Watts per cubic meter. However, if you include all of the infrastructure needed to make high voltage DC electricity offshore (e.g., the transformers, the aircraft-carrier-sized platform), the power density of the magnetic generators is drastically reduced, putting it close to the power density we achieved. Nonetheless, there is still room for improvement with our electrostatic system.

7.3.3 Outcomes of my research

The main contribution of my research was identifying and characterizing a system based on electrostatics that could make it easier to integrate ocean energy with our power grid—ultimately allowing another source of carbon-free energy to be part of our electricity mix. This electrostatics-based system would require substantially less infrastructure than current ocean energy systems and is constructed from sustainable and cost-effective materials.

While the system I proposed and tested in the lab is far from being commercially viable, I plan to continue working on it as a postdoctoral researcher at UW-Madison. My team entered a marine energy competition sponsored by the Department of Energy in the summer of 2023 and have progressed through Round I and Round II. As a post-doc, I will lead our involvement in Round III, hoping to secure more funding to bring our research to the next level! Regardless of the outcome of this competition, I hope that my research can serve as a foundation for future work in this vein and can inspire others.

Appendix A

Linear Direct-drive Machines

> *Many a deluded inventor has spent years of his life in endeavoring to 'harness the tides', and some have even proposed to compress air by tide- or wave-power for supplying energy... The fact is that a wave- or tide-motor would have, as a rule, but a small chance of competing commercially...*
>
> — Nikola Tesla, "The Problem of Increasing Human Energy" (1900)

An earlier aim of this work was to evaluate linear direct-drive varying capacitance machines for wave energy conversion. Five different designs were experimentally investigated, where each design incorporated a liquid in design of the capacitor.

A.1 Background on electrostatic wave energy conversion

Despite numerous efforts over the past several decades to unlock the potential of ocean wave energy, it continues to be an underutilized resource. As of 2022, the installed capacity of new wave energy systems was a mere 165.5 kW [1]. Historically, wave energy converter (WEC) research has focused on hydrodynamical and power take-off (PTO) design, with the electromechanical design being less of a priority. In fact, the vast majority of WECs continue to make use of the same technology for the electromechanical energy conversion process: electric machines based on the interaction of magnetic fields, be they

rotary vs. linear, synchronous vs. asynchronous, or wound-field vs. permanent magnet. While these conventional machines are suitable for electricity generation in high-speed applications (e.g., thermal power stations), their performance is fundamentally limited in low-speed applications, such as in wave energy conversion (see Section 1.3 in the Introduction for more information). The fundamental frequency of relevant ocean waves (wind-driven waves) is typically on the order of 10^{-2} to 10^{-1} Hz, which is many orders of magnitude lower than the typical speeds used in conventional power stations [47]. Given this discrepancy, alternative approaches in electromechanical energy conversion should be investigated for wave energy. One promising option utilizes electrostatic machinery.

In Section 2.2 of Chapter 2, electrostatic machines utilizing the triboelectric effect and piezoelectric effect are briefly mentioned but never discussed in detail, given their absence in macroscale power conversion applications. However, because these types of electrostatic devices have been investigated in wave energy conversion, albeit at low power levels, they will be briefly described. Triboelectric devices make use of the fact that when certain materials rub against each other, charges are induced on the surface of those material(s), creating an electric potential. This potential can then drive a current through a load. In piezoelectric systems, mechanical stress, e.g., compression, of certain materials causes net polarization of the dipole moments which results in a macroscopic electric potential across the material capable of driving current through an external load. For more information and examples of these devices, please see the review of electrostatic WECs in [21].

Nevertheless, researchers have had more success with varying capacitance machines than they have with triboelectric or piezoelectric devices in utility-scale WECs (>10 kW). In varying capacitance machines, the operating voltage is determined by an external supply and can be set to much higher voltages than are achievable with triboelectric and piezoelectric systems, yielding better power performance. Furthermore, variable-capacitor systems are readily characterized and described by elementary physics, whereas triboelectricity and piezoelectricity are subject to stochastic processes that can be difficult to model and predict.

Several researchers have developed WEC prototypes that utilize variable capacitors

[48]–[51]. A commonality among each of these variable-capacitor WECs is that they all use dielectric elastomer (DE) transducers in the construction of the variable capacitor. These DE transducers typically consist of a flexible polymer dielectric sandwiched between two conductors. These conductors serve as the capacitor electrodes and at least one of these electrodes has to be flexible, although most designs have both electrodes being flexible. Mechanical work (from the wave) deforms the capacitor, modulating its capacitance and thus converts mechanical energy into electrical energy.

While the results of the DE variable capacitor WEC research are promising, there are several issues that could limit their development. Because DEs are relatively new, there is little empirical data regarding their long-term durability, especially when subjected to high voltages, biofouling, and the harsh, corrosive sea environment [52], [53]. In addition, it is unclear if DE variable capacitor WECs can scale to utility power levels. [52] approximated that over 10^4 kg of DE material would be needed in systems rated for 100 kW. Given that the market for DEs is still emerging, it would need to rapidly grow to manufacture DEs in a cost-competitive manner. Finally, more work needs to be done to find appropriate electrode materials for DE systems. In prototypes, carbon powder, carbon grease, and hydrogels have been successfully employed but would not be reliable enough for an at-scale device [52].

One design option to circumvent the issues with DEs is to incorporate liquid(s) with the construction of the variable capacitor. Not only are liquids more durable than solids, but the nature of the mechanical excitation (the wave) is a slow-moving liquid, and so utilizing that liquid motion to directly vary some aspect of a variable capacitor (its gap distance, electrode area, or permittivity) could simplify the overall electromechanical energy conversion process.

A.2 Experimental Setup

Five direct-drive varying capacitance machines were constructed and tested at the bench scale. While the variable capacitor was different for each design, each design was equivalent

from a circuit-level perspective, matching the circuit in Fig. 3.1. Because the machines were direct-drive, the fundamental frequency was equal to the speed of ocean waves, resulting in load resistances needing to be in the range of several gigaohms for impedance matching. Because the highest impedance probe available had a resistance R_{pr} of only 100 MΩ, the probe was placed in series with the load resistor R_L to avoid the loading effect. In doing so, the probe voltage V_{pr} registered by the oscilloscope was just a fraction of the true output voltage V_o, related by the simple voltage divider expression $V_{pr} = V_o \frac{R_{pr}}{R_L + R_{pr}}$.

A programmable stepper motor with linear ball screw was used to emulate wave motion in each experiment, operating at speeds within the range of typical ocean wave frequencies (<1 Hz). Capacitance measurements were taken with the Keysight E4990A Impedance Analyzer, and large impedances were measured with the Keysight B2980B Series Femtoammeter/Electrometer.

A.3 Machine with solid electrode, liquid dielectric

A simple way to integrate liquid motion into the design of a varying capacitance machine is to use wave motion to pump a dielectric fluid between the plates of a capacitor. As the dielectric fluid moves between the plates, the effective permittivity varies between that of air and the fluid, which manifests as a change in capacitance proportional to the frequency of fluid motion.

Two machine prototypes utilizing different dielectric fluids were constructed and experimentally evaluated. FR3 soybean oil was used in the first prototype, and the second prototype utilized Galden perfluoropolyether (PFPE) EV110. These particular fluids were chosen because of their differing properties (see Table A.1): commonly used as an alternative to mineral oil in transformers, FR3 is a relatively inexpensive dielectric fluid but has a relaxation time $\tau_c = 8.5$ s, which is on the same order of magnitude as ocean wave periods (see Section 3.5 in Chapter 3 for more on τ_c). In contrast, PFPE has a $\tau_c = 250$ s but is far costlier.

Two parallel plate capacitors were constructed, and each was used with only one

Table A.1: Material properties of dielectric fluids, taken from [54] and [55]

Property	FR3	PFPE
ϵ	$3.2\epsilon_0$	$1.9\epsilon_0$
σ	3.3 pS/m	66.7 fS/m
τ_c	8.5 s	250 s
μ	33 cSt	0.77 cSt
E_{br}	30 kV/mm	15.7 kV/mm

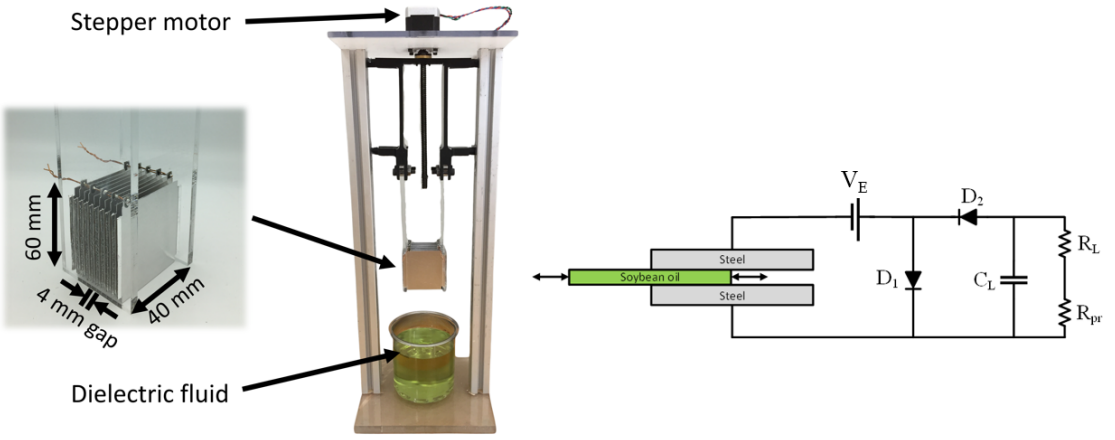

Figure A.1: Experimental setup used during experimentation with zoomed-in view of parallel plate capacitor prototype

dielectric fluid in order to not contaminate the other fluid. Each capacitor was constructed by laser cutting grooves into two acrylic slabs and placing ten 0.5 mm-thick aluminum plates into the grooves, such that the air gap between each plate was 4 mm. Copper wire was soldered to every other plate to create an alternating polarity. Fig. A.1 shows the experimental setup with a machine prototype, and Fig. A.2 shows the measured capacitance vs. position as well as R_{leak} vs. position for each prototype.

For each prototype, a series of experiments were carried out in which the bias voltage was varied between 1 and 5 kV with a step size of 1 kV, ten different values of R_L between 1 and 20 GΩ were used, and the stepper motor oscillated the capacitor at a rate of 12 mm/s, such that $T = 10$ s. In order to evaluate the effect of charge leakage, R_L was placed in series with the load, matching the circuit in Fig. 3.8.

P_L as a function of V_E and R_L is plotted in Fig. A.3a and Fig. A.3c for the FR3 soybean oil and PFPE, respectively. The values for P_L reflected in these figures are taken

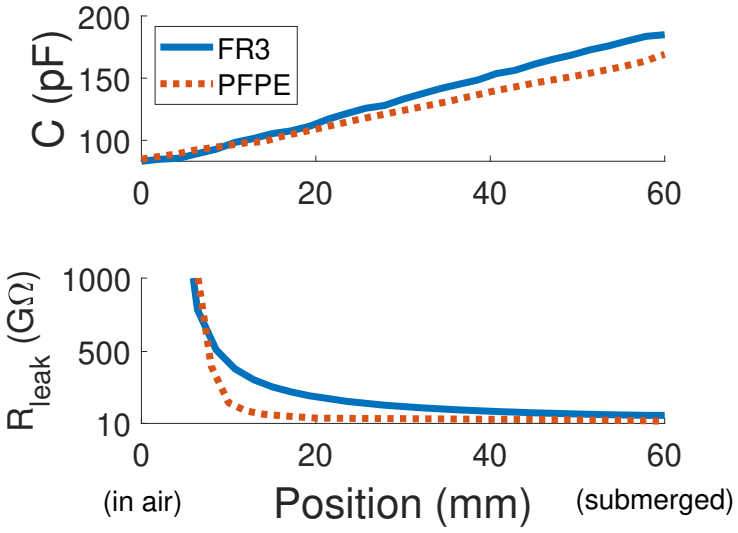

Figure A.2: Measured capacitance vs. position (top) and R_{leak} vs. position (bottom) for each prototype

as the average of five cycles of $C(t)$ at each operating point. The instantaneous values of P_L were estimated by 1) measuring V_{pr} with the oscilloscope, 2) finding the current through R_L by taking $I_L(t) = \frac{V_{pr}(t)}{R_{pr}}$, 3) subtracting off the DC bias to isolate $\widetilde{i}_L(t)$, and 4) using Eq. 3.25 to obtain the instantaneous value. Once P_L was determined for each operating point, Eq. 3.27 could be used to estimate η (see Fig. A.3b and Fig. A.3d).

Despite the PFPE having a 50x lower conductivity than the FR3 soybean oil, the minimum R_{leak} recorded for the capacitor with the PFPE was less than half the minimum value of R_{leak} for the capacitor with FR3 (25 GΩ vs. 64 GΩ). This lower R_{leak} is partially responsible for the poorer efficiency of the PFPE-based transducer than the FR3-based transducer. Another contributing factor is the fact that PFPE has nearly half the ϵ_r of FR3. Nevertheless, both variable capacitors exhibited very poor efficiencies, not exceeding 15% and 10% for the FR3 soybean oil and PFPE, respectively. Such poor efficiencies are not surprising, given the fact that the product $\tau\frac{R_{leak}}{R_L}$ should be far greater than 10 s (see criteria in Eq. 3.28-3.29) but equals 13 s and 4.3 s for the FR3 and PFPE capacitors, respectively. Ideally, their time constants should be at least two orders of magnitude slower in order to increase $\tau\frac{R_{leak}}{R_L}$ well beyond T.

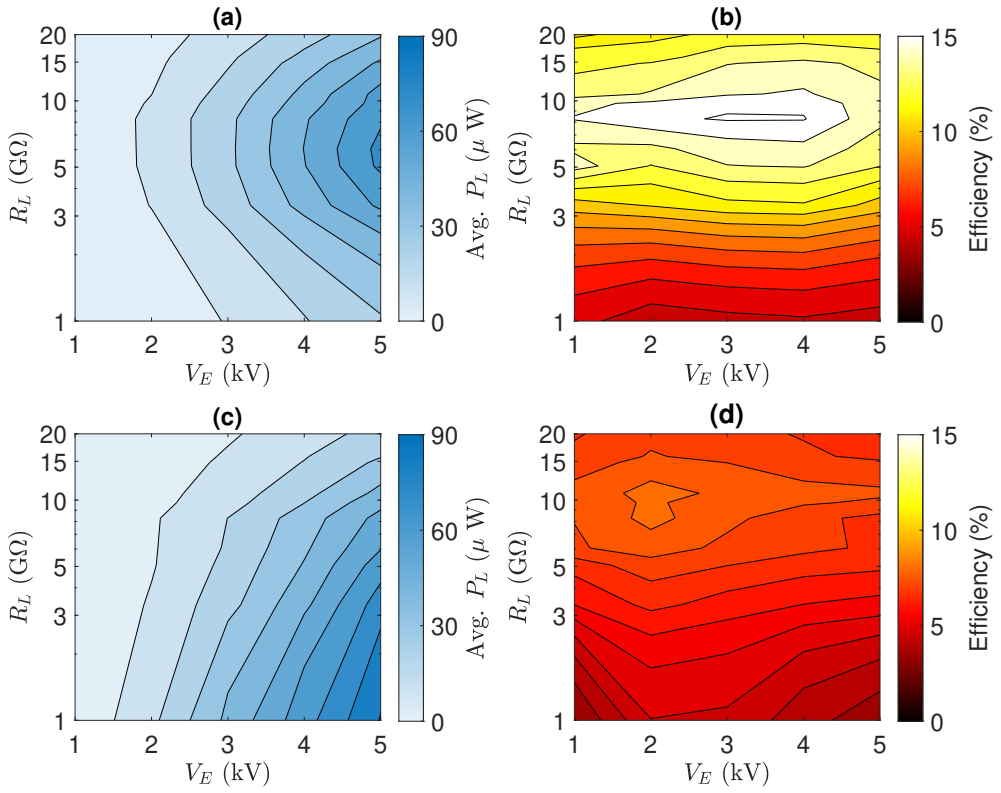

Figure A.3: (a) P_L using FR3 soybean oil, (b) Efficiency using FR3 soybean oil, (c) P_L using PFPE, and (d) Efficiency using PFPE

It is difficult to pinpoint the exact reason for the discrepancy between the measured R_{leak} and the rated conductivities of each fluid, but it could be related to a difference in the two liquids' moisture absorptivities or other abilities to become contaminated. In any case, it is worthwhile to emphasize that, despite the effort that was taken to ensure the purity of the fluids (e.g., using gloves during all stages of prototyping and experimenting, cleaning all components before assembly with an ultrasonic cleaner), the liquids must have become appreciably contaminated. If such a degree of contamination was possible in a relatively forgiving laboratory environment, maintaining high levels of purity for several years in the harsh ocean environment could be prohibitively difficult.

Looking at the criteria in Eq. 3.28-3.29, there are several strategies for mitigating the effects of leakage current in a variable capacitor:

1. Most obviously, R_{leak} should be as high as possible. However, as was demonstrated with this research, maintaining the purity of a liquid dielectric is not easy and the degree of contamination experienced was enough to dramatically reduce its efficacy. Solids tend to have lower conductivities than liquids but exhibit surface charge exchange when rubbed against other liquids, negating any charge buildup within the variable capacitor transducer [56].

2. Using a fluid with a greater permittivity would increase the saliency in capacitance. However, fluids with higher permittivities tend to either have high conductivities or pose a health or environmental hazard [19], [55].

3. Decreasing T would lower the material requirements on the dielectric medium. Because the periods of ocean waves are fixed, this would require using PTO(s) to increase the system speed.

Regarding the third point, it should be mentioned that rotating electrostatic machinery using dielectric fluids is able to circumvent the issue of charge leakage by increasing the machine pole count. Because the machine's effective electrical period is inversely proportional to the pole count, using a suitably high pole count can drastically shorten the

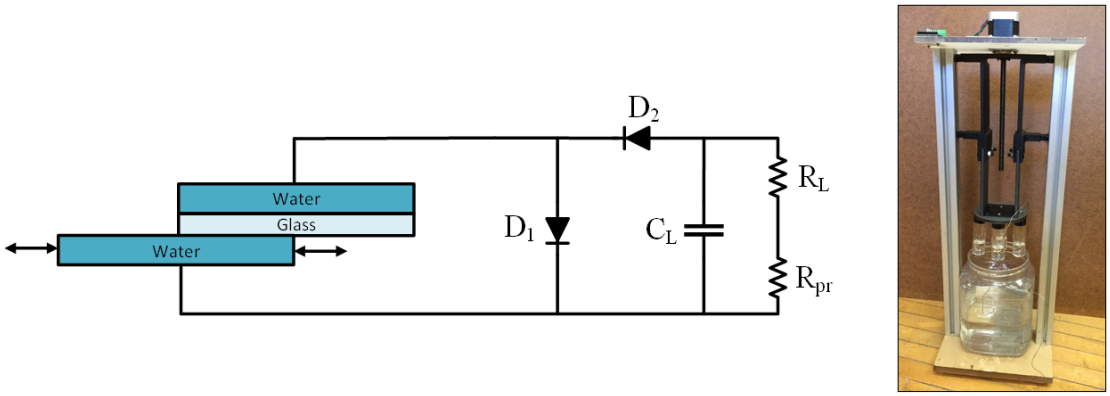

Figure A.4: Schematic of liquid electrode, solid dielectric design (left) and experimental setup (right)

electrical period. For example, in [57], 40 poles are used for a switched elastance electrostatic machine, and in [58], [59], 96 poles are used for a synchronous electrostatic machine with a rated fundamental frequency of 900 Hz.

A.4 Machine with liquid electrode, solid dielectric

Motivated by the shortcomings of the solid electrode, liquid dielectric design, a new variable capacitor design utilizing salt water electrodes separated by glass was investigated (see Fig. A.4). The underlying idea behind this new design was the fact that solid dielectrics have conductivities that are generally several orders of magnitude lower than liquid dielectrics, making them better insulators. In addition, by utilizing salt water as an electrode, the ocean waves themselves could be a part of the variable capacitor, as the capacitance would vary as the seawater washes over the glass.

To realize this design, glass vials were filled with a solution of 1% Na_2SO_4 and were mounted to a fixture attached to the motor (see Fig. A.5). Small wires making contact with the solution of Na_2SO_4 were bolted to the screws that held the vials in place, and the fixture was sandwiched by two plates, such that all of the screws (and thus solutions of Na_2SO_4) could be at the same electrical potential. A container filled with a solution of 1% Na_2SO_4 was placed beneath the vials to act as the other electrode.

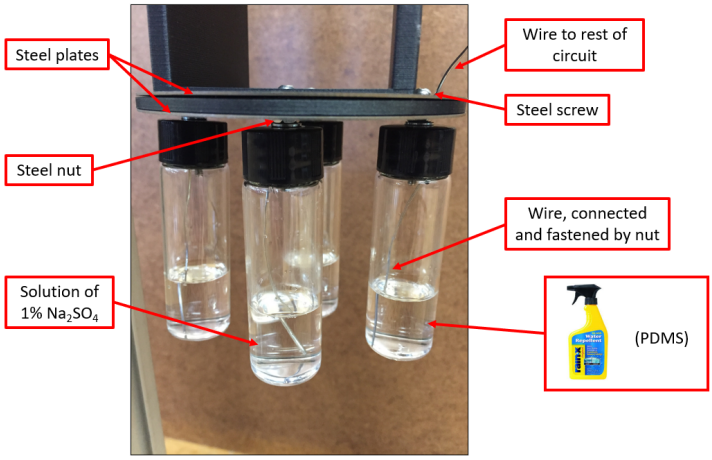

Figure A.5: Construction of capacitor in liquid electrode, solid dielectric design

During the first experiment with a 1 kV bias, 100 mHz motor oscillation, and a parallel RC load of 31 GΩ and 630 pF, no voltage rise was measured on the load. Initially, leakage resistance through residual water on the glass seemed to be a likely culprit. To combat this, RainX, which contains polydimethylsiloxane (PDMS), was applied to the outside of the glass vials to act as a hydrophobic layer and hopefully prevent residual water from adhering to the glass. However, this did not alleviate the issue, as there was still no voltage rise measured on the load, even with increasing the bias voltage and motor oscillatory speed.

The suspected real reason behind the inoperability of the liquid electrode, solid dielectric design is related to triboelectricity. While the mechanics of triboelectricity are not well-understood and are beyond the scope of this work, the triboelectric series reliably predicts which materials will induce charges when rubbed against each other [60]. PDMS and water are on opposite ends of the triboelectric series, meaning they will transfer charges. One possible explanation as to why this effect would render the variable-capacitor generator inoperable is that these induced charges acted to negate the bias applied from the external power supply, preventing the variable capacitor from acquiring a nonzero voltage. Interestingly, when the bias was removed from the capacitor and the motor set to oscillate the capacitor, the load voltage rose to an average of 24 V, corresponding to an output power of 18 nW as a "triboelectric generator."

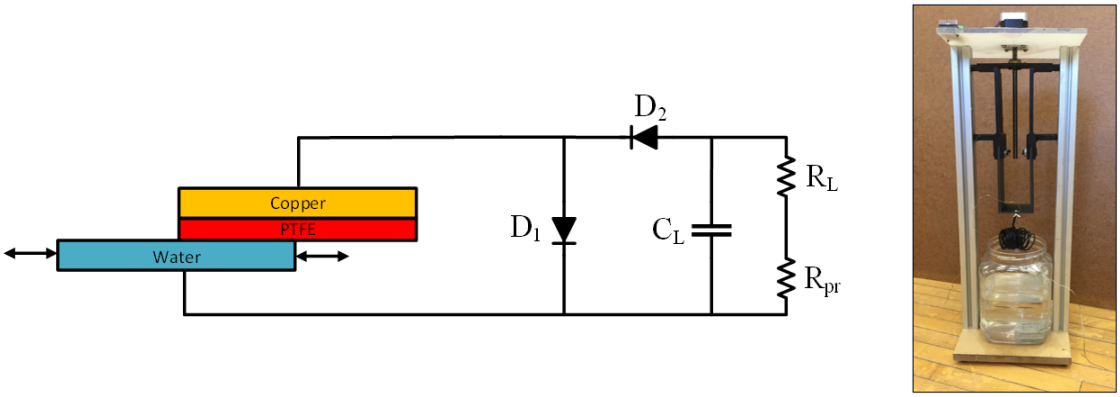

Figure A.6: Schematic of liquid-solid electrode, solid dielectric design (left) and experimental setup (right)

A.5 Machine with liquid-solid electrode, solid dielectric

To further test the hypothesis concerning triboelectricity, another design was proposed that utilized both a solid and liquid for each electrode, along with a solid dielectric. A spool of wire insulated with polytetrafluoroethylene (PTFE, commercially known as Teflon) was twisted in a coil shape and attached to the motor fixture that was situated above a container containing 1% Na_2SO_4 (see Fig. A.6). Not only is PTFE present on the triboelectric series, which allowed for the triboelectric hypothesis to be tested, but PTFE also has one of the lowest conductivities of all known materials, making it a good choice in a variable-capacitor generator if that configuration were to work.

The liquid-solid electrode, solid dielectric design was first tested as a variable-capacitor generator connected to a parallel RC load of 31 GΩ and 630 pF with a 1 kV bias voltage and mechanical oscillatory frequency of 100 mHz. No voltage was measured on the load. When the bias voltage was removed, the device now acting as a triboelectric generator charged the load to 152 V, corresponding to an output power of 740 nW. The presence of triboelectricity was confirmed by measuring the open-circuit voltage across the capacitor when no bias was applied and the capacitor was oscillating (see Fig. A.7).

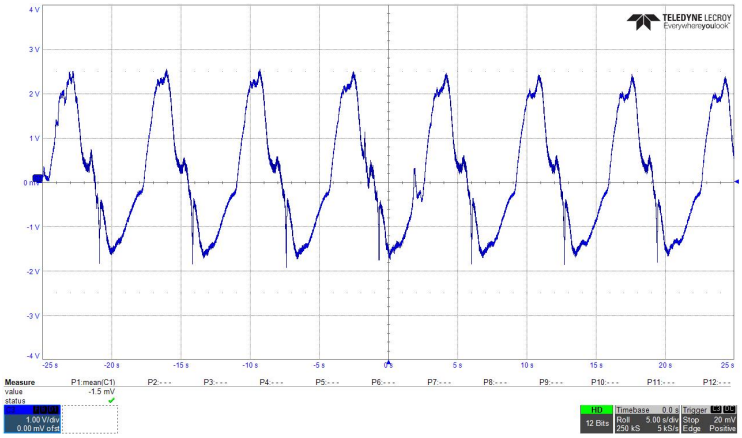

Figure A.7: Open-circuit voltage of liquid-solid electrode, solid dielectric design when no excitation is applied

A.6 Machine with liquid electrode, flexible dielectric

Before abandoning the idea of using liquid electrodes and solid dielectrics in a variable-capacitor generator, another design utilizing silicone rubber as the dielectric was investigated. It was theorized that a flexible material (as opposed to a rigid one) might not induce surface charges via triboelectricity. Additionally, this variant is similar to DE devices, lending operational promise.

The balloon of a silicone Foley catheter was filled with salt water (1% Na_2SO_4) and the port nozzle was retrofitted with a brass barbed hose connector, such that a bias voltage could travel from its application to the brass connector through the moisture trapped inside the walls of the catheter tube, down to the water in the balloon (see Fig. A.8). The balloon was placed in a container of salt water (also 1% Na_2SO_4), completing the capacitor. The plunger of a syringe was affixed to the stepper motor, allowing it to push air via the port nozzle into the catheter balloon to inflate it.

In both configurations as a variable-capacitor generator and as a triboelectric generator, the liquid electrode, flexible dielectric design did not produce any output power during experimentation, regardless of the load component values or speed of mechanical actuation. The circuit did not operate well as a variable-capacitor generator, likely because triboelectric charge transfer was observed during the open-circuit voltage measurement,

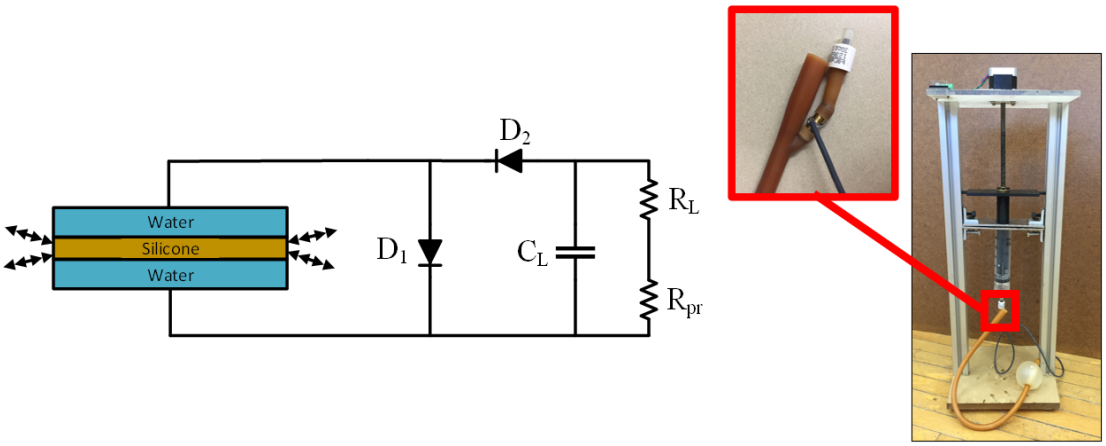

Figure A.8: Schematic of liquid electrode, flexible dielectric design (left) and experimental setup (right)

correlating with prior experience. It likely failed as a triboelectric generator due to the modest open-circuit voltage (400 mV peak-to-peak).

A.7 Machine with liquid-solid electrode, gaseous dielectric

Because salt water electrodes are only problematic when they rub against solid dielectrics, a new design was investigated that utilizes air (or theoretically, any gas) as the dielectric. If charges are deposited on a metal disc that is suspended above a body of water, those charges will electrically couple with the water, forming a capacitor whose capacitance changes as the water level varies.

Fig. A.6 shows the experimental setup to test this idea. To emulate a variable water level, a 48x48 cm metal sheet was attached to the stepper motor, such that it could move vertically. A plastic dish filled with tap water was placed directly beneath the metal sheet, such that the distance between the water and sheet was about 4 mm (i.e., capacitor air-gap is 4 mm). Although this setup is visually inverted from what was described earlier, it is physically the same since the relative motion between the water and metal sheet is all that matters.

Experimental results demonstrated that the liquid-solid, gaseous dielectric variable

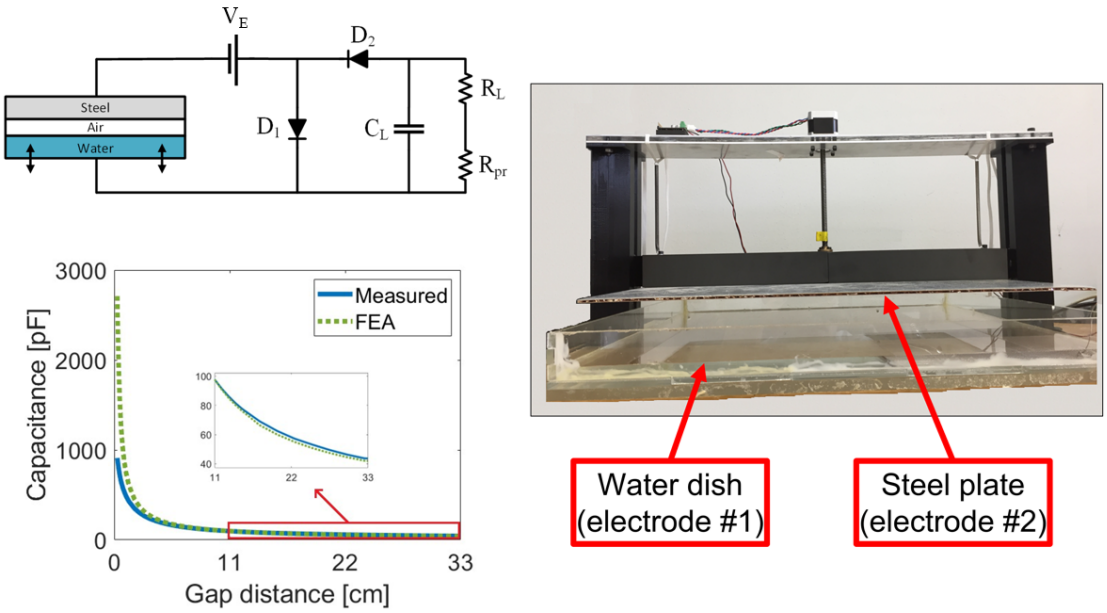

Figure A.9: Schematic of liquid-solid electrode, gaseous dielectric design (upper left), capacitance vs. position (lower left) and experimental setup (right)

capacitor behaved according to electrostatic power conversion theory and also did not exhibit any triboelectric charge transfer. It is clear from Fig. A.10 that the output power has a quadratic dependence on the bias voltage and a linear dependence on the oscillatory frequency, as expected. It is important to keep in mind, however, that increasing the bias voltage will not invariably yield a quadratic increase in power since the minimum gap distance d_{min} depends on V_E, where $d_{min} = \frac{V_E}{E_{br}}$, with E_{br} denoting the electric field strength. If the vertical displacement of the capacitor electrodes is denoted by Δh, then the change in capacitance ΔC from $C_{max} = \frac{\epsilon A}{V_E/E_{br}}$ to $C_{min} = \frac{\epsilon A}{V_E/E_{br}+\Delta h}$ is

$$\Delta C = C_{max} - C_{min} = \frac{\epsilon A \Delta h}{\frac{V_E}{E_{br}}\left(\frac{V_E}{E_{br}} + \Delta h\right)}, \tag{A.1}$$

which is $\mathcal{O}\left(\frac{1}{{V_E}^2}\right)$. Since $P \propto {V_E}^2 \frac{\Delta C}{\Delta t}$, the power of a variable air-gap capacitor is bounded as the operating voltage approaches infinity.

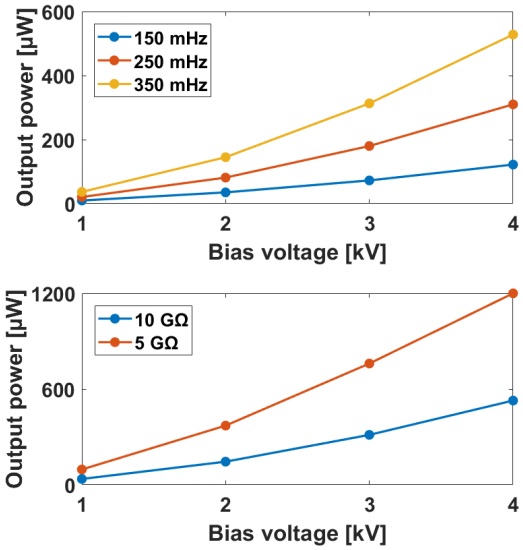

Figure A.10: Dependence of output power on bias voltage at various mechanical frequencies at a fixed load of 10 GΩ (top) and dependence of output power on bias voltage at various load resistances at fixed mechanical frequency of 350 mHz (bottom) for liquid-solid electrode, gaseous dielectric design

A.8 Discussion

Of the variable capacitor designs investigated, only two of them worked as intended: the solid electrode, liquid dielectric and the liquid-solid electrode, gaseous dielectric, see Table A.2. The other designs did not operate as varying capacitance machines, likely due to the presence of triboelectricity. In liquid-polymer triboelectricity, it has been hypothesized that protons and/or hydroxyl groups are transferred from water to the surface of the polymer it is rubbing against [61]. Thus, it is possible that these free charges combined with the charges that the external power supply had deposited on the capacitor electrodes, leaving it with no net charge and hence, zero voltage. While it is possible to exploit the triboelectric effect for power generation, the scalability of triboelectricity to higher power levels is unknown, as the highest reported powers are at the sub-watt level [62]. Varying capacitance machinery, on the other hand, has achieved power levels in the sub-kW range [19]. In addition, triboelectricity is highly sensitive to environmental parameters such as humidity, pH, and salt concentration, which could lead to unexpected and undesirable

Table A.2: Summary of linear direct-drive machine testing

Design	**Mode of generation**	**Max. output power**
Solid electrode, liquid dielectric	Variable-capacitor	490 nW
Liquid electrode, solid dielectric	Triboelectric	18 nW
Liquid-solid electrode, solid dielectric	Triboelectric	740 nW
Liquid electrode, flexible dielectric	-	0
Liquid-solid electrode, gaseous dielectric	Variable-capacitor	1.2 mW

behavior [61].

Bibliography

[1] IRENA, *Innovation outlook: Ocean energy technologies*. 2020.

[2] Enerdata, "Electricity domestic consumption," 2022.

[3] A. Mccoy, W. Musial, R. Hammond, D. M. Hernando, P. Duffy, P. Pérez, R. Baranowski, and P. Spitsen, "Offshore Wind Market Report : 2024," tech. rep., NREL, 2024.

[4] The White House, "Fact sheet: Biden-harris administration continues to advance american offshore wind opportunities," Mar. 2023. Accessed: 2024-10-17.

[5] IEA, "Offshore Wind Outlook 2019," tech. rep., IEA, 2019.

[6] IEA, "Electricity Information: Overview," 2021.

[7] R. Williams and F. Zhao, "Global Offshore Wind Report 2023," tech. rep., GWEC, 2023.

[8] PwC Consultancy, "Unit Investment Cost Indicators-Project Support to ACER," tech. rep., ACER, 2023.

[9] J. Engström, *Underground cables in transmission networks*. PhD thesis, Lund University, 2007.

[10] D. V. A. N. Hertem, O. Gomis-bellmunt, and J. U. N. Liang, *HVDC Grids in the Energy Vision of the Future*. Wiley, 2016.

[11] C. Gorgs, "Deutschlands schwimmende Steckdose," 2017.

[12] N. A/S, "High voltage offshore ac cables." `https://www.nkt.com/products-solutions/high-voltage-cable-solutions/high-voltage-offshore-solutions/high-voltage-offshore-ac-cables`, 2024. Accessed: 2024-10-16.

[13] N. Schmitz and D. Novotny, *Introductory electromechanics*. Ronald Press, 1 ed., 1965.

[14] A. Abdalrahman and E. Isabegovic, "DolWin1 - Challenges of connecting offshore wind farms," in *2016 IEEE International Energy Conference (ENERGYCON)*, pp. 1–10, IEEE, apr 2016.

[15] S. F. Philp, "The vacuum-insulated, varying capacitance machine," *IEEE Transactions on Electrical Insulation*, vol. EI-12, no. 2, 1977.

[16] F. Paschen, "Ueber die zum Funkenübertragung in Luft, Wasserstoff und Kohlensäure bei verschiedenen Drucken erforderliche Potentialdifferenz," *Annalen der Physik*, vol. 273, no. 5, pp. 69–96, 1889.

[17] N. J. Felici, "Rotating-cylinder electrostatic generator with hydrogen insulation," *Atomnaya Energiya*, vol. 11, no. 2, pp. 140–152, 1961.

[18] B. Gokhberg, A. Ioffe, and N. Reynov, "Models of Multi-Disc High-voltage Electrostatic Generators," *Zhurnal Teknicheskoy Fiziki*, vol. 9, no. 23, pp. 2094–2103, 1939.

[19] D. C. Ludois, K. Frankforter, B. Ge, A. N. Ghule, P. Killeen, and R. Knippel, "Macroscale Electrostatic Rotating Machines and Drives: A Review and Multiplicative Gain Performance Strategy," *IEEE Journal of Emerging and Selected Topics in Power Electronics*, vol. 10, no. 1, 2022.

[20] J. G. Trump, *Vacuum Electrostatic Engineering*. PhD thesis, Massachusetts Institute of Technology, 1933.

[21] D. Skrovanek and D. C. Ludois, "Electrostatic Wave Energy Conversion: A Review of Devices, Theory, and Hurdles," *IEEE Transactions on Energy Conversion*, vol. 39, no. 2, pp. 941–952, 2024.

[22] B. Ge, *The Modeling, Design and Demonstration of Electrostatic Synchronous Machines*. PhD thesis, University of Wisconsin-Madison, 2018.

[23] A. Ioffe, "The Electrostatic Generator," *Zhurnal Teknicheskoy Fiziki*, vol. 9, no. 23, pp. 2017–2080, 1939.

[24] N. J. Felici, "Ten years of research on electrostatics at the University of Grenoble 1942-1952," *British Journal of Applied Physics*, vol. 4, pp. S62–S67, jan 1953.

[25] R. O'Donnell, N. Schofield, A. Smith, and J. Cullen, "Design Concepts for High-Voltage Variable-Capacitance DC Generators," *IEEE Transactions on Industry Applications*, vol. 45, no. 5, pp. 1778–1784, 2009.

[26] L. Müller and J. W. Kimball, "High gain dc–dc converter based on the cockcroft–walton multiplier," *IEEE Transactions on Power Electronics*, vol. 31, no. 9, pp. 6405–6415, 2016.

[27] R. O'Donnell, N. Schofield, A. Smith, and J. Cullen, "The variable-capacitance machine for off-shore wind generation," in *Proc. 6th Int. Workshop Large-Scale Integr. Wind Power Transmiss. Netw. Offshore Wind Farms*, pp. 131–135, IEE, 2006.

[28] H. R. Florentino, D. Galayko, R. C. S. Freire, B. A. Luciano, and C. Florentino, "Energy Harvesting Circuit Using Variable Capacitor with Higher Performance," *Journal of Integrated Circuits and Systems*, vol. 6, pp. 68–74, dec 2020.

[29] D. Galayko and P. Basset, "A General Analytical Tool for the Design of Vibration Energy Harvesters (VEHs) Based on the Mechanical Impedance Concept," *IEEE Transactions on Circuits and Systems I: Regular Papers*, vol. 58, pp. 299–311, feb 2011.

[30] D. Galayko, A. Dudka, A. Karami, E. O'Riordan, E. Blokhina, O. Feely, and P. Basset, "Capacitive Energy Conversion With Circuits Implementing a Rectangular Charge-Voltage Cycle—Part 1: Analysis of the Electrical Domain," *IEEE Transactions on Circuits and Systems I: Regular Papers*, vol. 62, pp. 2652–2663, nov 2015.

[31] A. Karami, *Study of electrical interfaces for electrostatic vibration energy harvesting*. PhD thesis, Sorbonne Université, 2019.

[32] A. Kempitiya, D.-A. Borca-Tasciuc, and M. M. Hella, "Low-Power Interface IC for Triplate Electrostatic Energy Converters," *IEEE Transactions on Power Electronics*, vol. 28, pp. 609–614, feb 2013.

[33] E. O'Riordan, E. Blokhina, O. Feely, and D. Galayko, "Modelling and analysis of vibration energy harvesters with charge pump conditioning circuits," in *2014 IEEE International Symposium on Circuits and Systems (ISCAS)*, no. 1, pp. 1247–1250, IEEE, jun 2014.

[34] E. O'Riordan, A. Dudka, D. Galayko, P. Basset, O. Feely, and E. Blokhina, "Capacitive Energy Conversion With Circuits Implementing a Rectangular Charge-Voltage Cycle Part 2: Electromechanical and Nonlinear Analysis," *IEEE Transactions on Circuits and Systems I: Regular Papers*, vol. 62, pp. 2664–2673, nov 2015.

[35] S. Debnath, J. Qin, B. Bahrani, M. Saeedifard, and P. Barbosa, "Operation, control, and applications of the modular multilevel converter: A review," *IEEE Transactions on Power Electronics*, vol. 30, no. 1, pp. 37–53, 2015.

[36] H. Polinder, J. A. Ferreira, B. B. Jensen, A. B. Abrahamsen, K. Atallah, and R. A. McMahon, "Trends in wind turbine generator systems," *IEEE Journal of Emerging and Selected Topics in Power Electronics*, vol. 1, no. 3, pp. 174–185, 2013.

[37] D. Novotny, T. Lipo, and T. Jahns, *Introduction to Electric Machines and Drives*. University of Wisconsin-Madison, 1 ed., 2009.

[38] J. Macdonald and D. Edmondson, "Exact Solution of a Time-Varying Capacitance Problem," *Proceedings of the IRE*, vol. 49, pp. 453–466, feb 1961.

[39] J. Melcher, *Continuum Electromechanics*. MIT Press, 1 ed., 1981.

[40] H. Polinder, F. van der Pijl, G.-J. de Vilder, and P. Tavner, "Comparison of direct-drive and geared generator concepts for wind turbines," *IEEE Transactions on Energy Conversion*, vol. 21, no. 3, pp. 725–733, 2006.

[41] L. Electronics, "5 mva pad-mount transformer - 600v delta primary - 33000y/19050 grounded wye secondary - knan - bell green," 2024. Accessed: 2024-12-02.

[42] Windtech International, "The topside for the offshore substation for the merkur offshore wind farm is installed," 2018. Accessed: 2024-12-02.

[43] TenneT TSO GmbH, "DolWin kappa," Tech. Rep. April, TenneT TSO, Bayreuth, 2022.

[44] E. Bochum, "Wind drive technology - gearboxes for wind turbines," 2024. Accessed: 2024-12-02.

[45] I. Provac Sales, "Edwards xds35i scroll pump - surplus new," 2024. Accessed: 2024-12-02.

[46] Amprion GmbH, "Underground AC cables," 2024. Accessed: 2024-11-09.

[47] A. Pecher and J. P. Kofoed, *Handbook of Ocean Wave Energy*. Springer-Verlag, 2017.

[48] P. Jean, A. Wattez, G. Ardoise, C. Melis, R. Van Kessel, A. Fourmon, E. Barrabino, J. Heemskerk, and J. P. Queau, "Standing wave tube electro active polymer wave energy converter," in *Electroactive Polymer Actuators and Devices (EAPAD) 2012* (Y. Bar-Cohen, ed.), vol. 8340, apr 2012.

[49] S. Chiba, M. Waki, C. Jiang, M. Takeshita, M. Uejima, K. Arakawa, and K. Ohyama, "The possibility of a high-efficiency wave power generation system using dielectric elastomers," *Energies*, vol. 14, no. 12, pp. 1–17, 2020.

[50] G. Neidlein, C. Hentschel, N. Scharmann, C. Langenstein, M. Voss, and B. Hagemann, "Wellenenergietransformer mit elektroaktiver Polymerfolie," 2011.

[51] G. Moretti, S. Rosset, R. Vertechy, I. Anderson, and M. Fontana, "A Review of Dielectric Elastomer Generator Systems," *Advanced Intelligent Systems*, vol. 2, no. 10, 2020.

[52] G. Moretti, M. Santos Herran, D. Forehand, M. Alves, H. Jeffrey, R. Vertechy, and M. Fontana, "Advances in the development of dielectric elastomer generators for wave energy conversion," *Renewable and Sustainable Energy Reviews*, vol. 117, 2020.

[53] I. Denes, "EPoSil - Elektroaktive Polymere auf Silikonbasis zur Energiegewinning: Schlussbericht," tech. rep., Robert Bosch GmbH, Renningen, 2016.

[54] S. . S. Inc., "Solvay Specialty Polymers Galden EV Performance Fluids," tech. rep.

[55] B. Ge and D. C. Ludois, "Dielectric liquids for enhanced field force in macro scale direct drive electrostatic actuators and rotating machinery," *IEEE Transactions on Dielectrics and Electrical Insulation*, vol. 23, no. 4, pp. 1924–1934, 2016.

[56] D. Skrovanek and D. C. Ludois, "Variable capacitors utilizing liquids for low-frequency wave energy harvesting," in *IEEE Industrial Applications Society Annual Meeting (IAS)*, (Nashville), 2023.

[57] G. Reitz, B. Butrymowicz, J. Reed, B. Ge, and D. C. Ludois, "A switched elastance electrostatic machine constructed from sustainable elements for rotational actuators," in *2017 IEEE Energy Conversion Congress and Exposition (ECCE)*, pp. 2389–2395, IEEE, oct 2017.

[58] P. Killeen, A. N. Ghule, and D. C. Ludois, "A Medium-Voltage Current Source Inverter for Synchronous Electrostatic Drives," *IEEE Journal of Emerging and Selected Topics in Power Electronics*, vol. 10, no. 2, pp. 1597–1608, 2022.

[59] B. Ge, A. N. Ghule, and D. C. Ludois, "High torque density macro-scale electrostatic rotating machines: Electrical design, generalized d-q framework, and demonstration," *IEEE Transactions on Industry Applications*, vol. 55, no. 2, pp. 1225–1238, 2019.

[60] Y. Liu, J. Mo, Q. Fu, Y. Lu, N. Zhang, S. Wang, and S. Nie, "Enhancement of Triboelectric Charge Density by Chemical Functionalization," *Advanced Functional Materials*, vol. 30, no. 50, pp. 1–33, 2020.

[61] M. D. Sosa, M. L. Martínez Ricci, L. L. Missoni, D. H. Murgida, A. Cánneva, N. B. D'Accorso, and R. M. Negri, "Liquid-polymer triboelectricity: Chemical mechanisms in the contact electrification process," *Soft Matter*, vol. 16, no. 30, pp. 7040–7051, 2020.

[62] C. Rodrigues, D. Nunes, D. Clemente, N. Mathias, J. M. Correia, P. Rosa-Santos, F. Taveira-Pinto, T. Morais, A. Pereira, and J. Ventura, "Emerging triboelectric nanogenerators for ocean wave energy harvesting: State of the art and future perspectives," *Energy and Environmental Science*, vol. 13, no. 9, pp. 2657–2683, 2020.